Real-time simulation of soft tissue deformation for surgical simulation

A thesis submitted in fulfilment of the requirements for the degree of Doctor of Philosophy

Jinao Zhang

BEng (MechEng) (Hons), RMIT University

School of Engineering

College of Science, Engineering and Health

RMIT University

August 2017

Declaration

I certify that except where due acknowledgement has been made, the work is that of the author alone; the work has not been submitted previously, in whole or in part, to qualify for any other academic award; the content of the thesis is the result of work which has been carried out since the official commencement date of the approved research program; any editorial work, paid or unpaid, carried out by a third party is acknowledged; and, ethics procedures and guidelines have been followed.

I acknowledge the support I have received for my research through the provision of an Australian Government Research Training Program Scholarship.

Jinao Zhang

25.08.2017

Acknowledgements

I would like to express my sincere gratitude to my supervisors, A/Prof. Yongmin Zhong and Prof. Gholamreza Nakhaie Jazar for their invaluable suggestions, support and encouragement throughout my Ph.D. research program at RMIT University. I also would like to thank my other committee members in the candidature milestone reviews for their immense knowledge, insightful comments, and interest in my work.

My deepest gratitude goes to my family, for their unwavering love, unyielding support, and encouragement throughout my life.

To my family.

Contents

List of Figures

List of Tables

Abstract

Surgical simulation plays an important role in the training, planning and evaluation of many surgical procedures. It requires realistic and real-time simulation of soft tissue deformation under interaction with surgical tools. However, it is challenging to satisfy both of these conflicting requirements. On one hand, biological soft tissues are complex in terms of material compositions, structural formations, and mechanical behaviours, resulting in nonlinear deformation characteristics under an external load. Due to the involvement of both material and geometric nonlinearities, the use of nonlinear elasticity causes a highly expensive computational load, leading to the difficulty to achieve the real-time computational performance required by surgical simulation. On the other hand, in order to satisfy the real-time computational requirement, most of the existing methods are mainly based on linear elasticity under the assumptions of small deformation and homogeneity to describe deformation of soft tissues. Such simplifications allow reduced runtime computation; however, they are inadequate for modelling nonlinear material properties such as anisotropy, heterogeneity and large deformation of soft tissues. In general, the two conflicting requirements of surgical simulation raise immense complexity in modelling of soft tissue deformation.

This thesis focuses on establishment of new methodologies for modelling of soft tissue deformation for surgical simulation. Due to geometric and material nonlinearities in soft tissue deformation, the existing methods have only limited capabilities in achieving nonlinear soft tissue deformation in real-time. In this thesis, the main focus is devoted to the real-time and realistic modelling of nonlinear soft tissue deformation for surgical simulation. New methodologies, namely new ChainMail algorithms, energy propagation method, and energy balance method, are proposed to address soft tissue deformation. Results demonstrate that the proposed methods can simulate the typical soft tissue mechanical properties, accommodate isotropic and homogeneous, anisotropic and heterogeneous materials, handle incompressibility and viscoelastic behaviours, conserve system energy, and achieve realistic, real-time and stable deformation. In the future, it is projected to extend the proposed methodologies to handle surgical operations, such as cutting, joining and suturing, for topology changes occurred in surgical simulation.

1. Introduction

Modelling and simulation of soft tissue deformation is a fundamental research topic in surgical simulation. In general, surgical simulation requires realistic and real-time simulation of soft tissue response to tool-tissue interactions [1, 2]; however, it is challenging to satisfy both of these conflicting requirements.

1.1 Challenge of Modelling of Soft Tissue Deformation

- **Challenge of realistic simulation.** The challenge of realistic simulation manifests itself in the context of surgical simulation as the accurate results of material characterisation of *in vivo* biological tissues, mesh generation of organ models, and numerical solutions to soft tissue behaviours [3]. In order to simulate realistic soft tissue mechanical behaviours, the material properties of living tissues need to be characterised. Such properties are patient-specific, and it can be difficult to predict the mechanical behaviours of *in vivo* tissues. Further, the geometry of anatomical models must be acquired from patient-specific medical images, and the problem domain must be discretised. This process is still not fully automated, requiring significant manual work in image segmentation and mesh generation. Finally, numerical issues for soft tissue simulation must be overcome. Most biological soft tissues exhibit anisotropic and heterogeneous stiffness and are nearly incompressible, which can lead to ill-conditioned problems during simulation. The ill-conditioned problems have a high condition number which measures the sensitivity of the output of a function to changes in the input. Such problems can be numerically expensive to solve and may lead to inaccuracy or even failure of simulation. Boundary conditions, which provide additional constraints of state variables at the boundary of the problem domain, are also difficult to define due to complex tissue compositions and interactions between organs.

- **Challenge of real-time simulation.** A simulation that is mechanically realistic, but not interactive would not fit for surgical simulation. The challenge of real-time simulation manifests itself as the high solution speed to tool-tissue interactions. Soft tissue response must be computed in a short time to achieve the required update rate of visual displays and haptic devices for real-time user interactions with virtual organs. The update rate required for visual feedback is at least 30 Hz for the rendered graphics to appear as continuous motion to the human sensory system, while a much higher update rate is required for haptic feedback, requiring a solution to be obtained at least 1,000Hz for stable and smooth tactile rendering from the haptic device with which the user moves the virtual surgery tools [4]. Due to nonlinear characteristics of soft tissues, the solutions are often computationally expensive to obtain. The need for real-time computation, however, often requires simplifications of the problem that adversely affect the simulation accuracy [5].

In all, the realistic and real-time characteristics of surgical simulation not only pose challenges to each aspect but also affect each other mutually since performance improvement on one aspect is mainly achieved to the detriment of the other.

1.2 Contributions and Outline

In this thesis, new methodologies are proposed to address soft tissue deformation for surgical simulation. Mainly, the new proposed methodologies focus on addressing (1) nonlinear soft tissue deformation, (2) anisotropic, heterogeneous and viscoelastic soft tissue material properties, and (3) real-time computational performance. The detailed contribution of each proposed methodology is presented at the beginning of each chapter.

The rest of the thesis is organised as follows:

- Chapter 2 reviews the state-of-the art deformable models for soft tissue modelling for surgical simulation.
- Chapter 3 presents new ChainMail algorithms for soft tissue deformation, namely the time-saving volume-energy-conserved ChainMail algorithm, ellipsoid bounding region-based ChainMail algorithm, and neural dynamics-based ChainMail algorithm.
- Chapter 4 presents energy propagation method for soft tissue deformation, namely the energy propagation method, neural dynamics-based energy propagation method, and neural dynamics-based stable simulation of soft tissue deformation.
- Chapter 5 presents energy balance method for soft tissue deformation.
- Chapter 6 discusses the deformable models for soft tissue deformation and outlines the remaining challenges for soft tissue modelling in surgical simulation.
- Chapter 7 concludes the thesis with summaries of proposed methodologies and presents possible avenues of future work.

2. Literature Review

In this chapter, a review on the deformable models developed for interactive surgical simulation is presented. The deformable models are divided into three basic categories: (i) the heuristic modelling approach; (ii) continuum-mechanical approach; and (iii) others. The first category includes heuristic deformable models that are derived from rather straight forward modelling schemes for the geoemtry of soft tissues, allowing for the inclusion of elastic properties. The second category includes deformable models that consider the deformation of soft tissues from the viewpoint of continuum mechanics and decribe the mathematical terms by equations of solid mechanics. Based on the ultisation of mesh, this category is further divided into mesh-based methods and meshless methods. Lastly, the third category includes deformable models that are based on other concepts for soft tissue deformation, such as neural network technique, machine learning, data-driven approach, and fibre and fluid technique.

2.1 Heuristic Modelling Approach

Deformable models presented in this category are derived from rather straight forward modelling schemes. Namely, the geometrically-based models, mass-spring models, and ChainMail algorithm are presented. The main advantage of these deformable models is their computational efficiency, which can meet the real-time computational requirement of surgical simulation. However, these models generally suffer from ambiguity in detemination of model parameters to reproduce the mechanical behaviours of soft tissues.

2.1.1 Geometrically-based Models

In the early efforts of modelling of soft tissue deformation for surgical simulation, various geometrically-based approaches, such as free-form deformation (FFD) [6] and deformable splines [7], were studied owing to their computational advantages. In 1986, Sederberg and Parry proposed a lattice-based FFD technique [6] which deforms a soft tissue surface model by deforming the parametric parallelepiped lattice in which the model is imbedded, based on the manipulation of control points in a free-form manner (see Fig. 2.1(a)). As the position of control points changes, the surface of the free-form lattice is deformed using a tensor product trivariate Bernstein polynomial to determine the displacement at each point on the lattice surface. Global and local deformations can be obtained through the manipulation of control points. Cover *et al.* [7] studied a deformable spline technique for soft tissue deformation and applied the technique in the simulation of laparoscopic gall-bladder surgery. It induces deformation on a soft tissue surface model by defining a potential energy function, which is proportional to the degree of elastic deformation, and minimising the potential energy with respect to

the displacement of control points, obtaining the corresponding deformation state (see Fig. 2.1(b)). Although the geometrically-based models are often fast for interactive soft tissue deformation, they do not provide a realistic simulation of soft tissue mechanical behaviours to meet the physical accuracy requirement of surgical simulation, since the deformation process is carried out indirectly via the manipulation of control points and may bear little or no resemblance to the physically-based deformation. As such, the geometrically-based models have been mainly superseded by physically-based deformable models, which consider physical properties of materials and physical dynamics to improve simulation accuracy and obtain a satisfactory degree of physical realism.

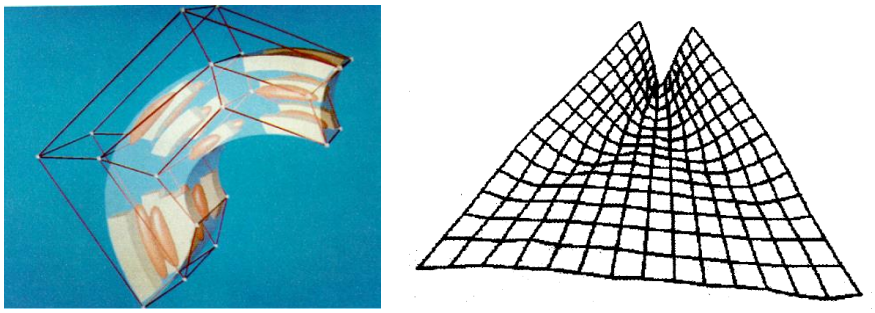

(a) (b)

Figure 2.1 (a) Deformed state of an FFD lattice with control points [6]; and (b) deformed surface using deformable splines [7].

2.1.2 Mass-Spring Models

Mass-spring model (MSM) [8, 9] is a popular deformable model based on the principle of dynamics for soft tissue deformation. It is widely used for modelling of soft tissue deformation, such as in the simulation of surgical repair of heart valves [9], and surveyed well in the literature [10-13]. As illustrated in Fig. 2.2, the basic idea of MSM is it considers a soft tissue model as a network of lumped masses connected via elastic springs. The dynamics of soft tissue deformation are governed by the non-rigid mechanics of motion, in which the internal force at a mass point is due to the sum of spring forces exerted on the point by the connected elastic springs. The positions of mass points are obtained by considering balance of force through time integration schemes in the temporal domain. MSM is simple in implementation and efficient in computation, making it an effective means for modelling of soft tissue deformation for interactive surgical simulation. Soft tissue mechanical properties, such as heterogeneity, nearly incompressibility, and time-dependent viscoelasticity, can be realised by techniques such as the modification of spring stiffness constants [14], utilisation of penalty forces [15], and incorporation of mechanical dampers [16], respectively. The literature on soft tissue deformation using

MSM is abundant, and various improvements were proposed to facilitate the capabilities of MSM. Compared to the conventional MSM where elastic springs are governed by the linear Hooke's law, Basafa and Farahmand [17] employed a piecewise nonlinear spring model with a two-step expression of force-displacement relationship for modelling of nonlinear soft tissue deformation in laparoscopic surgery. They considered the typical force-displacement relationship of a soft biological tissue made by a nonlinear "toe" region at small deformation and a linear region at large deformation and formulated the spring force accordingly. Qin *et al.* [18] facilitated MSM by constructing a multilayered MSM based on the layered structure of biological soft tissues and applied the technique in the virtual orthopedic surgery. Choi *et al.* [16, 19, 20] devised a force propagation MSM for virtual-reality (VR) based medical learning. The basic idea of the force propagation MSM is it considers the process of soft tissue deformation as a process of force propagation among the mass points on a per-node basis [19]. A penetration depth is employed to limit the range of force propagation for the benefit of computational efficiency; the optimum value of the penetration depth is determined based on the criteria that no noticeable changes in shape is detected as the penetration depth is further increased beyond a certain value. Duan *et al.* [8] applied deformable constraints to MSM to directly manipulate the position of mass points to satisfy a set of predefined geometric and volume constraints for the nonlinear force-displacement characteristics and nearly incompressibility of soft tissues.

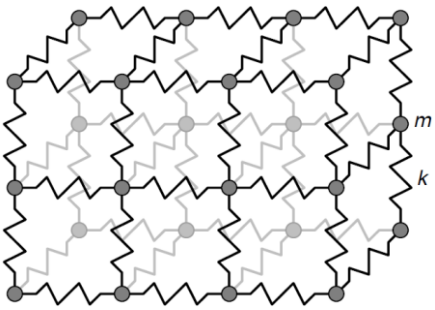

Figure 2.2 A portion of a MSM: points of lumped masses m is connected via a network of elastic springs of stiffness k [13].

Despite the improved physical realism offered by the principle of dynamics, MSM suffers from a number of deficiencies that limit its model accuracy for soft tissue deformation. In general, mass-spring systems are not convergent as the mesh is refined, meaning the solution of deformation does not converge on the true solution [10]. Instead, the geometrical structure and topological arrangement of elastic springs heavily influence the deformation behaviours of the model and may introduce artificial anisotropy and heterogeneity [21], giving rise to stability and accuracy issues [3]. Further, the nonlinear stress-strain relationship of soft biological tissues is difficult to be reproduced accurately by MSM, since the mechanical behaviour of individual springs and

dampers cannot be simply related to the constitutive laws governing the mechanical behaviours of the model, regardless of linear Hookean or nonlinear springs, since the internal nodal force is determined by the sum of the spring forces, which are dependent only on the position of neighbouring points, spring rest lengths and spring stiffness constants. Owing to this, optimisation algorithms such as the Simulated Annealing (SA) [22] and Genetic algorithms (GA) [23] are often employed for optimisation of spring stiffness constants by fitting the deformation of MSM to some reference data to achieve certain global mechanical behaviours. However, parameter optimisation is a tedious task, and the results of a particular optimisation may no longer be valid if model topology arrangement and boundary conditions are changed. In all, the popularity of MSM in surgical simulation is mainly attributed to its simple mesh structure, easy programmability, and low computational complexity; as the evolution of MSM already reached its peak [11], the application of MSM in surgical simulation may be superseded by other deformable models that have higher physical realism with real-time computational efficiency.

2.1.3 ChainMail Algorithm

Compared to MSM, ChainMail algorithm [24, 25] is a more simplified approach for soft tissue deformation. In the early years of computer graphics, objects were commonly represented by surface-based polygonal models; despite their computational efficiency, these surface models are less accurate than modelling of objects' volume for soft tissue deformation [5]. ChainMail algorithm was proposed under this background, which considers the volumetric nature of human organs with a deformation law derived from MSM, forming a linked volume to describe the volumetric behaviours of soft tissues [25]. The basic unit in ChainMail algorithm is called the chain element, which occupies the position of a voxel in a linked volume model. Each chain element enforces a geometric bounding region formed by geometric limits to each of its neighbouring chain elements. The position of a chain element will be adjusted to satisfy the geometric constraints only if the position is outside of the bounding region enforced by its neighbours (see Fig. 2.3). This position adjustment mechanism is further followed by a relaxation scheme that minimises the global potential energy of the system. ChainMail algorithm is unconditionally stable and can simulate various soft tissue mechanical behaviours, such as the nonlinear force-displacement relationship, hysteresis, and stress relaxation [26]. One significant advantage of ChainMail algorithm is its computational efficiency afforded by the position adjustment mechanism, and hence it has been used extensively in the modelling of large medical volume deformation consisting of millions of voxels, each of which stores important information related to patient-specific tissues and organs [27-29]. Such large volumetric datasets cannot be interactively deformed by conventional deformable models; even with significant model processing, the computational complexity of these conventional approaches limit the resolution of the captured medical datasets to only a small fraction that is usually several orders of magnitude lower, resulting in an inevitable loss of details of the source data [27].

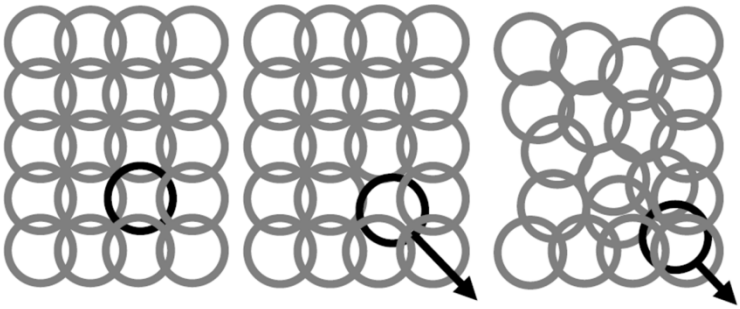

(a) (b) (c)

Figure 2.3 Deformation of ChainMail algorithm: (a) a chain element (black) at undeformed state; (b) the chain element is moved along the path of the arrow; and (c) its neighbouring chain elements are moved to satisfy geometric constraints between elements, leading to the deformed state.

Since its inception, ChainMail algorithm has seen numerous variants that improve its physical accuracy and computational performance. Schill *et al.* [30] presented an enhanced ChainMail to simulate the vitreous humor in the eye, a substance that is heterogeneous and highly deformable. The enhanced ChainMail extends the traditional ChainMail to the modelling of heterogeneous materials. Park *et al.* [31] proposed a shape-retaining 3D ChainMail, or S-Chain in short, for real-time haptic rendering. Haptic forces are calculated based on the idea that the reflection force is proportional to the sum of distances of all moved chain elements. To address the issue of geometric degradation due to shear distance limit in the traditional ChainMail, Wang and Fenster [32] studied a restricted 3D ChainMail, which replaces the shear distance limit by an angular shear limit expressed in degree, confining the movement of a chain element within a ChainMail bounding trapezium or frustum in 2D and 3D, respectively. Li *et al.* [33] proposed a surface ChainMail for web-based surgical simulation, which enhances the traditional ChainMail by defining the stretching, compressing and shear limits using a strain limit expressed relative to the rest length between two chain elements. Further, Li and Brodlie [34] also devised a generalised ChainMail that can be applied to any type of grid. The chain elements can be arbitrarily positioned and linked to any number of neighbouring chain elements, extending the range of applications of ChainMail algorithm. To achieve more accurate deformation with physical meanings, Wang and Lu [35] presented an adaptive S-Chain, utilising an energy-based wave propagation on the surface of the object, whereas the inner volume is deformed by the S-Chain. Based on the generalised ChainMail, Levin *et al.* [36] proposed a ChainMail-mass-spring hybrid model. The ChainMail constraints are employed for checking constraint violations, and spring forces are calculated once the ChainMail constraints are satisfied. Duysak and Zhang [37] presented a mass-spring chain model, combining the strengths of both MSM and ChainMail algorithm. They applied the ChainMail constraints to a surface triangular mesh, confining the movement of a spring within a ChainMail bounding region made by

super elastic limit, rigid limit, minimum spring length and maximum spring length. Neubauer studied a Direct Volume Deformation ChainMail algorithm, or Divod ChainMail in short, for direct volume deformation [38]. Rodriguez *et al.* [29] proposed an SP-ChainMail which implements ChainMail algorithm on the Graphics Processing Unit (GPU). This method can achieve a speed gain of higher than 20x when using a modern GPU compared to that of the traditional ChainMail. The SP-ChainMail was further extended by the heterogeneous SP-ChainMail [27] to simulate heterogeneous materials and handle multiple concurrent deformations.

Thanks to various improvements made to the ChainMail algorithm, it has been applied to many medical applications such as the arthroscopic knee surgery [39], intra-ocular surgery [40], web-based surgical simulations [33, 34], prostate brachytherapy simulation [41], virtual endoscopy applications [38], training simulators with respiratory components [42], angioplasty simulation [43], percutaneous transhepatic cholangio-drainage (PTCD) simulation [28] and image-based palpation simulation [44]. Despite various applications in the field of surgical simulation, the main limitation of ChainMail algorithm stems from the arbitrary selection of parameters for geometric constraints [45, 46]. Further, since the ChainMail relies solely on elements' position rather than the equations of motion to determine elements' displacement, the dynamic behaviours of soft tissues are difficult to realise.

2.1.4 Other Heuristic Approaches

Other deformable modelling methods such as the shape matching technique coupled with position-based solver [47] were also studied for soft tissue deformation. Shape matching is a geometrically motivated approach based on finding the least squares optimal rigid transformations between two sets of points with a prior knowledge of correspondence [48]. Similar to ChainMail algorithm, the shape matching technique also directly manipulates the position of points to satisfy a set of geometric constraints, and it is numerically stable. However, this method relies on determination of an optimal cluster stiffness coefficient for accurate soft tissue deformation, rather than considering material properties of soft tissues.

2.2 Continuum-Mechanical Approach

Different from the heuristic models that assume a discrete representation of soft tissue models for deformable modelling, continuum-mechanical methods consider a soft tissue model as a continuum medium based on the continuum mechanics of solid and employ constitutive laws to account for the complex mechanical behaviours of soft tissues. The solution procedure of these methods typically involves the consideration of minimisation of overall potential system energy and/or other fundamental physical balance laws to determine unknown field

variables over the problem domain. The typical solution methods in this category can be divided into two sub-categories based on the utilisation of object mesh, such as the finite element methods (FEM) and boundary element methods (BEM) in the mesh-based methods, and meshfree total Lagrangian explicit dynamics (MTLED) algorithm and smoothed particle hydrodynamics (SPH) in the meshless methods.

2.2.1 Mesh-based Methods

FEM is a typical method for simulation and analysis of soft tissue deformation in surgical simulation, which requires explicit construction of object mesh to approximate the constitutive laws governing the mechanical behaviours of soft tissues. In FEM, an approximated discrete representation of the soft tissue under study can be obtained by dividing the soft tissue model into a number of elementary building components called finite elements, forming a finite element mesh of tetrahedrons or hexahedrons that conforms to the problem domain (see Fig. 2.4). The constitutive laws are approximated with respect to each finite element and satisfied at an element level. The individual equations of finite elements under external loads are assembled into a large system of equations that represents the mechanical behaviours of the soft tissue model, from which nodal displacements are determined [49]. Soft tissue material properties, such as the Young's modulus and Poisson's ratio, can be obtained by experimental measurements and directly integrated into the parametric constitutive laws for finite element calculation. Thanks to its physical accuracy, FEM is popular in the computational biomechanics [50] and has been applied successfully to a wide range of biomechanical modelling of soft tissues, such as the modelling of soft tissue deformation in image-guided hepatic surgery [51], computer-integrated neurosurgery [52], whole-body medical image registration [53], and interventional electrocardiology procedures [54]. Although FEM can achieve high model accuracy, such accuracy is generally obtained at the expense of high computational cost of problem solutions, leading to great challenges for interactive soft tissue deformation.

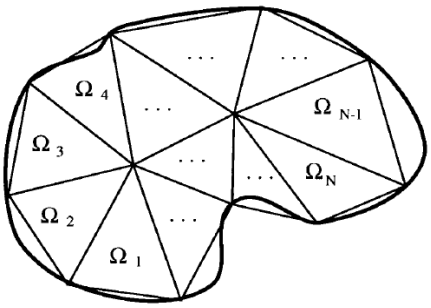

Figure 2.4 The problem domain is divided into a number of finite elements Ω_N [55].

2.2.1.1 Simplification of FEM

To meet the real-time computational performance for surgical simulation, various techniques were proposed to simplify the computational complexity of FEM. Explicit FEM [10] is often employed for soft tissue deformation, in which the masses and the internal and external forces are lumped to the nodes, leading to block diagonal mass and damping matrices through which the computation can be performed at an element level, allowing simple implementation and easy parallel computation [56]. Bro-Nielsen and Cotin studied a fast finite element (FFE) model [57] which simplifies the computational complexity of FEM using matrix condensation [55]. By condensing the full system matrix describing the behaviours of object volume to a new matrix that involves only the variables of surface nodes while preserving the original physical characteristics of the volumetric model, the computational time for the volumetric deformation can be reduced to the computational time of a model only involving the surface nodes of the mesh, leaving only the displacement of the boundary nodes as unknowns [58]. Despite the improved computational efficiency, this simplification significantly degrades the simulation accuracy. Cotin *et al.* [59] applied a pre-computation technique to the linear FEM to achieve real-time computational performance for hepatic surgery simulation; they pre-computed the equilibrium solutions of a linear FEM model and applied the principle of superposition to determine nodal positions at interactive rates. However, the pre-computed elementary deformations are only valid for a given configuration of the stiffness matrix. Cotin *et al.* [60] also proposed a tensor-mass model (TMM) which incorporates the concept of shape functions of FEM into the formulation of internal forces and obtains nodal positions in a mass-spring fashion. The TMM simplifies the computational complexity of FEM to the complexity of MSM while retaining the calculation of internal forces to be independent of mesh topology. BEM [61, 62] simplifies FEM complexity by formulating the weak form of the principle of virtual work into a surface integral form based on the assumption of an isotropic and homogeneous material interior. Owing to this assumption, the deformation solution is reduced to the solution of boundary integration equation on the surface mesh only, which significantly facilitates the computational performance. However, BEM only works for objects whose interior is composed of an isotropic and homogeneous material [11], and hence it cannot accommodate the anisotropic and heterogeneous characteristics of soft tissues. Wang *et al.* [63] applied BEM into a surgical simulation for haptic deformation of soft tissues and surgical cutting. Zhu and Gu [62] applied BEM into a mass-spring constraint model, which uses BEM to determine the global deformation and MSM to interactively simulate the dynamic behaviours of soft tissues. Inspired by the geometric constraints used in the heuristic approach, Tang and Wan [64] studied a strain-limiting FEM for virtual surgical training. They reduced FEM complexity of solving a system of equations to solving a set of geometric constraints by using a series of strain-limit constraints on the principle strains of the strain tensor. They also employed a multi-resolution hierarchy mesh structure to facilitate the global convergence of the constrained system. Despite the computational advantage of this method, the utilisation of strain limits adversely confines the deformation range of finite elements. Liu *et al.* [65] coupled FEM computation of strain energy density function with MSM internal force calculation for modelling of soft

tissue deformation. The spring force calculation in this model is derived from the strain energy density at neighbouring points, which is determined from the strain energy of a tetrahedron in the finite element mesh; soft tissue mechanical behaviours can be reflected by various forms of strain energy density function. Goulette and Chen [66] presented a hyperelastic mass links (HEML) algorithm for fast computation of soft tissue deformation. HEML is derived from the framework of FEM but calculates nodal positions via a mass-spring fashion based on local displacements. They obtained a speed gain more than 40x by HEML compared to standard TMM.

2.2.1.2 Total Lagrangian Formulation

Considering the frame of reference, FEM employs two formulations which are the updated Lagrangian formulation and the total Lagrangian formulation for determination of unknown value of state variables [67]. In the updated Lagrangian formulation, all variables are referred to the current configuration of the system, i.e. from the end of the previous time step. The advantage of this formulation is the simplicity of incremental strain description and low internal memory requirements [52]; however, it requires a re-calculation of spatial derivatives in each time step, since the reference configuration is changing with time. This re-calculation process can be computationally expensive and not suitable for real-time computational performance of surgical simulation. Compared to the updated Lagrangian formulation, the total Lagrangian formulation considers all variables referred to the initial configuration of the system. Contrary to the incremental strain description, the strain formation in the total Lagrangian formulation leads to correct results after a load cycle and no error accumulation occurs [68]. Most important, it permits that all derivatives with respect to spatial coordinates to be pre-calculated and stored [69], since the initial configuration is explicitly defined and does not change with time. Based on this, Miller *et al.* [56] presented a total Lagrangian explicit dynamics (TLED) finite element algorithm for soft tissue deformation, achieving fast solution calculation through the pre-computation of spatial derivatives, element-level computation, and explicit time integration. Given these three important attributes of TLED, it can be easily parallelised on GPU to take advantage of hardware parallel computation. Taylor *et al.* [69] achieved a high-speed TLED solution method with a GPU parallel computing and obtained a speed gain up to 16.8x compared to the equivalent Central Processing Unit (CPU) implementations. Later, Taylor *et al.* [70] achieved a speed gain of 56.3x using NVDIA Compute Unified Device Architecture (CUDA) implementation, which was subsequently integrated into the GPU-based finite element package NiftySim [71]. The GPU-accelerated TLED has been applied successfully to the simulation of neurosurgical procedures [67, 72], whole-body computed tomography (CT) image registration [53], and its computational potential utilising a wide range of GPUs has also been analysed in [73]. Szekely *et al.* [68] applied the total Lagrangian formulation-based FEM into the simulation of uterus deformation. Also based on the total Lagrangian formulation, Marchesseau *et al.* [74] presented a multiplicative Jacobian energy decomposition (MJED) approach for discretising hyperelastic

materials on linear tetrahedral meshes. The key idea of this approach is to decouple in the strain energy, the invariants of the right Cauchy-Green deformation tensor from the Jacobian, so as to avoid matrix inversions and complex derivate expressions, leading to a faster matrix assembly than the standard FEM. MJED is fully general and requires the user to provide a decomposition of the strain energy into simple terms. With this formulation, pre-computation can be performed to speed-up the assembly of stiffness matrices. Mafi and Sirouspour [75] also studied a total Lagrangian formulation-based FEM algorithm coupled with GPU-based implicit dynamics for soft tissue deformation. The GPU-based solution addresses the real-time computational challenges in both areas of FEM matrices construction and solving the system matrix resulting from implicit integration.

2.2.1.3 Model Reduction

In addition, model reduction techniques [76] have also been applied to FEM for achieving improved computational efficiency. The essential idea of model reduction technique is to employ a set of global basis that is, in a statistical sense, the best suited to reproduce the complete models, by which the full system response is projected onto a smaller dimensional subspace, leading to a reduction in the number of degrees of freedom for solution calculation. This is in sharp contrast with standard FEM, which employs general purpose, piecewise polynomial shape functions to approximate the solutions in the Galerkin framework [77]. The solution procedure is made up by two steps: an offline step, in which the response of the organ to prescribed loads is extracted to construct a meta-model and stored in the memory, and an online step, in which the model is interpolated for any other load state to perform a reduced-model simulation with less degrees of freedom. Niroomandi *et al.* [78] studied a model reduction technique based on the proper orthogonal decompositions (POD) for simulation of palpation of human cornea with surgical tools. Despite the improved computational efficiency, the reduced model is actually linear since no updating of the tangent stiffness matrix is performed, resulting in higher strains in comparison with a standard FEM model. Owing to this deficiency, Niroomandi *et al.* [79] coupled POD with a nonlinear solver, the asymptotic numerical method (ANM), constructing a geometrically nonlinear reduced-order model for soft tissue deformation. Later, Niroomandi *et al.* [80] generalised their POD approach by considering a parametric problem using proper generalised decomposition (PGD) to simulate live deformation due to interactions with surgical scalpels. As a generalisation of PODs, the resulting PGD solution is expressed as a finite sum of separable functions that provides a meta-model for the problem, and this meta-model can then be applied in real time to obtain the response of the system at kilohertz rates. Radermacher and Reese [81] also facilitated the computational performance of POD by using discrete empirical interpolation methods (DEIM). The conventional model reduction techniques show a limited reduction in computational time for nonlinear problems, since the reduced equation system still requires evaluations of all finite element quantities at each Gauss point. As an additional treatment, their method further reduces the nonlinear terms by an empirical interpolation based on a small number of interpolation indices. They

obtained a speed gain of 10x compared to the classical POD methods without empirical interpolation. A review of the model reduction techniques can be found in [82].

2.2.1.4 Element-related Issues

When applying the mesh-based methods to the computation of soft tissue deformation, it is important to consider element-related issues to avoid numerical deficiencies. In order to satisfy the computational requirement of surgical simulation, the finite element models must use numerically efficient low-order elements, such as the eight-node linear under-integrated hexahedrons or four-node linear tetrahedrons [72]. However, it is known that the standard formulation of these elements exhibits numerical deficiencies that need to be handled in order to maintain numerical accuracy. The eight-node linear under-integrated hexahedrons exhibit the zero energy mode, where individual elements are deformed while the overall mesh is undeformed, resulting in hourglass-like element shapes referred to in the literature as hourglassing. Joldes *et al.* [83] proposed an efficient hourglass control algorithm based on the total Lagrangian formulation to eliminate the zero energy mode (see Fig. 2.5). The standard formulation of the four-node linear tetrahedrons exhibits artificial stiffening when simulating nearly incompressible materials such as biological soft tissues, referred to in the literature as volumetric locking [71]. Joldes *et al.* [84] addressed this issue by using an improved average nodal pressure (IANP) linear tetrahedron formulation (see Fig. 2.6).

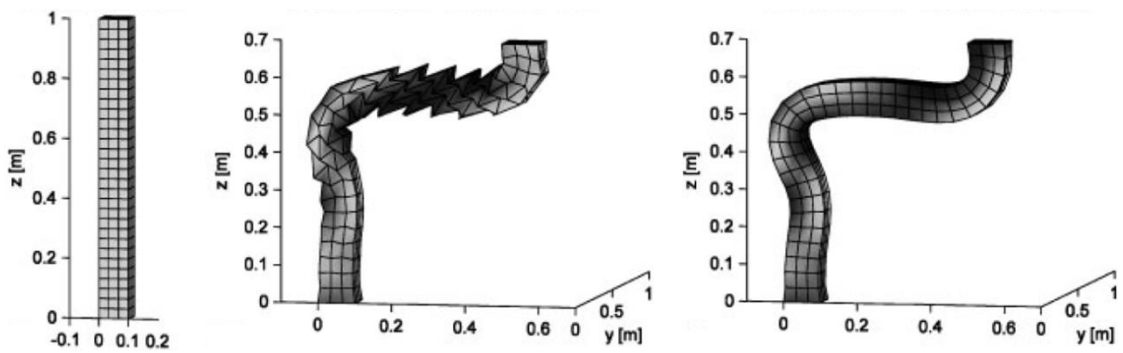

(a) (b) (c)

Figure 2.5 Hourglass control in a deformed column: (a) undeformed shape; (b) deformed shape without hourglass control; and (c) deformed shape with hourglass control [83].

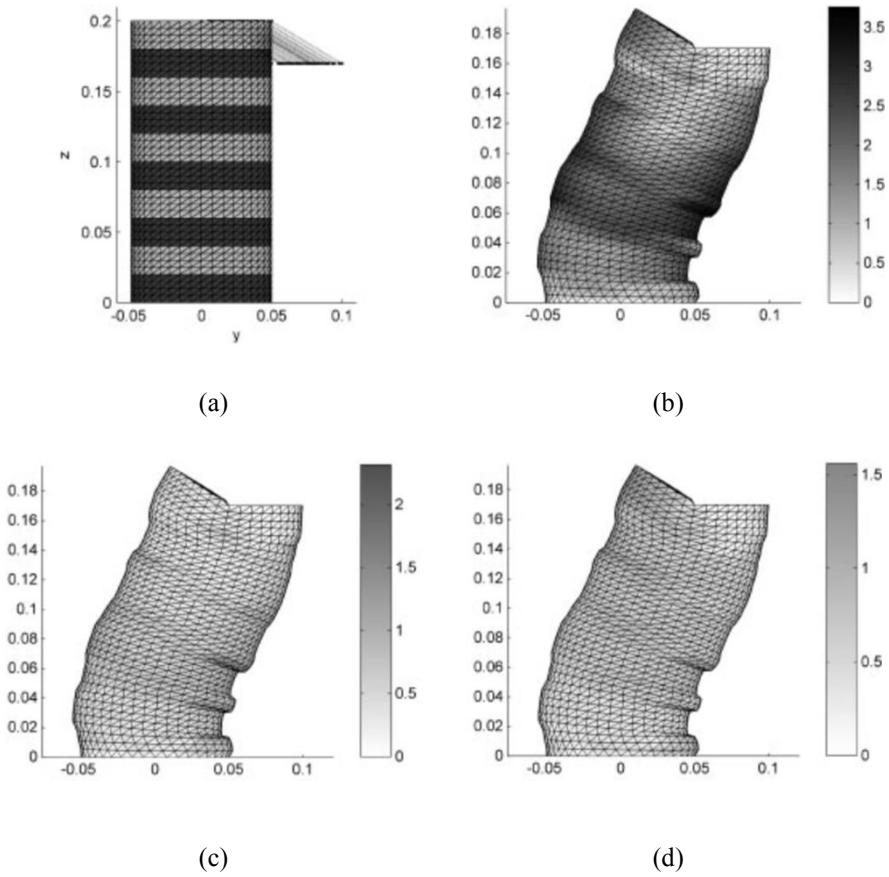

Figure 2.6 Volumetric locking control in a deformed cylinder: (a) undeformed shape with prescribed nodal displacements; (b) locking tetrahedral elements; (c) average nodal pressure (ANP) elements; and (d) IANP elements; color bars show the position difference of surface nodes to the reference solution using hexahedral elements [84].

2.2.2 Meshless Methods

Despite the popularity and high level of accuracy of finite element-based methods in the computation of soft tissue deformation for surgical simulation, the results of these simulations rely heavily on the quality of the object mesh that discretises the model geometry. Given the considerations of physical accuracy and numerical convergence, a good quality mesh is always required. However, owing to the complex geometry of a human organ, it is very hard to build a good quality mesh automatically. An experienced analyst is often required to manually create a quality mesh, consuming valuable human time. It is evident in [85] that a good hexahedral mesh took more than two months to be generated by an experienced analyst, which is a major bottleneck in the efficient generation of patient-specific models to be used in real-time simulation of surgical procedures [85].

Even if a good quality mesh is generated, the solution method may still fail in the case of large deformation where elements become highly distorted during the loading process, leading to element inversions [86] with zero or negative Jacobians [4].

2.2.2.1 Meshless Total Lagrangian Explicit Dynamics

Compared with mesh-based methods, meshless methods [85, 87-89] conduct object deformation without involving mesh topology of the discretised soft tissue model, overcoming the degradation of mesh quality of mesh-based methods at large deformation. It uses a set of particles (mass points) dispersed arbitrarily in the problem domain and interpolates state variables of each particle through consideration of state variables at neighbouring particles. Based on the total Lagrangian formulation where pre-computation can be performed, Horton *et al.* [85] proposed a meshless total Lagrangian explicit dynamics (MTLED) algorithm in the element-free Galerkin (EFG) framework. Numerical integration is conducted through the theory of moving least-squares (MLS) with the aid of hexahedral background integration cells that are not conformed to the simulation geometry (see Fig. 2.7). As in the TLED finite element algorithm, MTLED applies pre-computation of all derivatives with respect to spatial coordinates of each integration cell and uses the deformation gradient to determine the full system matrix at each time step. With equal number of nodes, the presented MTLED runs at half the speed of a hexahedral-based TLED simulation but three times faster than a similar tetrahedral-based simulation [85]. However, the standard meshless shape functions are generally not polynomials and are constructed using support nodes located beyond the boundary of integration cells, making numerical integrations in the meshless method more challenging. Further, the use of hexahedral background integration cells in MTLED may induce volume inaccuracies when the hexahedral cells are intersected by a domain boundary due to the complex geometry of a human organ. Zhang *et al.* [90] addressed these issues in the framework of MTLED by coupling the finite element shape functions with MLS to impose essential boundary conditions and employing tetrahedral background integration cells to improve the accuracy of volumetric integration. Zou *et al.* [91] employed a radial point interpolation method (RPIM) for easy enforcement of essential boundary conditions, since its shape functions have the Kronecker delta function peoperty. They applied the technique into a neurosurgical simulation. To further improve the numerical accuracy of MTLED, Chowdhury *et al.* [92] studied a modified MLS (MMLS) algorithm which uses the second-order polynomial basis to generate more accurate approximations of deformation fields for randomly distributed nodes. For the same size of supporting domain, the MMLS can generate more accurate results than the classical MLS of linear basis, and it is computationally more efficient since the radius of influence need not to be as large as that of in the classical MLS with quadratic basis. Despite the advantage of MTLED in handling large deformation of soft tissues, it should not be used when reaction forces and displacement of individual nodes are needed, since the method is accurate in terms of overall reaction forces but not quite as good with individual displacements or

forces [85].

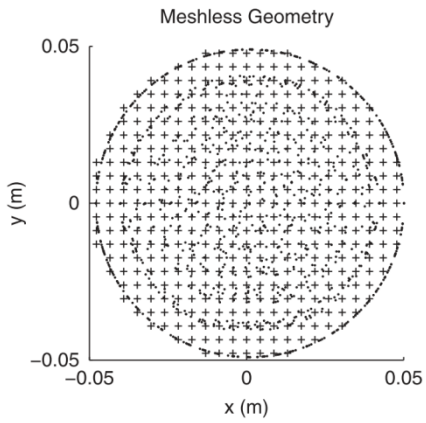

Figure 2.7 A meshless geometry: nodes (·) are dispersed arbitrarily in the problem domain with background integration points (+) [85].

2.2.2.2 Smoothed Particle Hydrodynamics and Point-Collocation-based Method of Finite Spheres

Different from MTLED which uses a grid of background cells for numerical integration, smoothed particle hydrodynamics (SPH) and point-collocation-based method of finite spheres (PCMFS) were also studied for soft tissue deformation. In these methods, the particles in the problem domain have an associated smoothing distance over which the state variables are interpolated by a kernel function (see Fig. 2.8) by considering state variables at neighbouring particles. Palyanov *et al.* [93] presented a predictive-corrective incompressible SPH (PCISPH) algorithm package named Sibernetic for biological soft tissue simulation, while Raucsh *et al.* [94] employed a normalized total Lagrangian SPH, taking its natural ability of creating material discontinuities for modelling of soft tissue damage and failure. De *et al.* [21] applied a localised linear PCMFS model for real-time soft tissue deformation based on the assumption that the surgical tool-tissue interaction is local and the deformation field dies off rapidly with increase in distance from the surgical tool tip. Later Lim and De [4] extended the localised linear PCMFS by considering geometric nonlinearity which enhances the response of linear model with nonlinear deformation in the local neighbourhood of surgical tool-tip. To further extend PCMFS to accommodate nonlinear characteristics of soft tissues, Banihani *et al.* [95] applied the POD technique to PCMFS with consideration of hyperelastic materials. Despite the advantage of meshless methods in handling large deformation and discontinuities, the meshless methods generally have difficulty in handling sparely sampled regions [96], and their accuracy heavily relies on the proper placement of sampled nodes [21, 85].

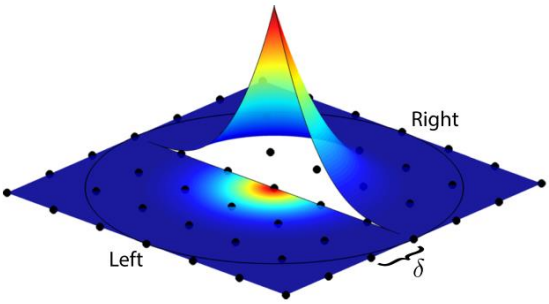

Figure 2.8 A kernel function: (right) the kernel's weight distribution; and (left) projection of the kernel function onto the 2D plane to illustrate the radius of influence (in this case three times the particle distance δ [94]).

2.3 Other Modelling Approaches

Apart from the above-mentioned modelling methods for soft tissue deformation for surgical simulation, a few other methods based on different concepts were also studied for soft tissue deformation. Zhong *et al.* [97] proposed a cellular neural network (CNN) approach, taking its real-time computational performance for interactive soft tissue deformation. Soft tissue deformation is carried out from the viewpoint of potential energy propagation, in which the mechanical load of an external force applied to soft tissues is considered as the equivalent potential energy, according to the law of conservation of energy, and it is propagated in the soft tissues through CNN-based neural propagation. De *et al.* [98] also studied a neural network technique of machine learning for soft tissue deformation. The computational process is divided into an offline and online phase, in which the offline phase pre-computes the response of a FEM model subject to prescribed displacements and optimises the coefficient of neurons through training of a radial basis function network (RBFN); the online phase reconstructs the deformation field using the trained RBFN. The concept of machine learning for computation of soft tissue deformation was further explored by Lorente *et al.* [99] for modelling of liver deformation during breathing. In this approach, deformation data are used to feed a supervised machine learning model to find a mapping function of the input variables that can approximate the known outputs. This mapping function is constructed and capable of generating an output, in this case the deformation, for future unseen inputs, in this case the prescribed displacements. Therefore, the performance of machine learning model is highly dependent on the collected data and the chosen learning algorithm. Similarly, Bickel *et al.* [100] studied a data-driven approach based on a linear co-rotational FEM for soft tissue deformation. They captured the deformations of a real object and presented each of them as a spatially varying stress-strain relationship in the FEM model. Material properties are then interpolated from these stress-strain relationships in the strain-space. Different from the aforementioned approaches, Costa [101] presented a fast deformation model based on the principle of Pascal and conservation of volume to simulate deformation of soft tissues formed by fibres and

fluid. By using the conservation of volume to represent the nearly incompressibility of soft tissues, the volume displacement in one direction directly causes the displacement of any surface in the opposite direction. This approach is particular fast since the variation of liquid pressure within a confined object is constant for the liquid inside the object, according to the principle of Pascal, and it has the same value for all vertices. However, this method is only valid for objects filled with fluids and does not exhibit any dynamic behaviours.

2.4 Numerical Time Integrations

Modelling of soft tissue deformation for surgical simulation often requires the modelling of dynamic behaviours of soft tissues, leading to the need of integrating dynamic equations in the temporal domain. The integration scheme chosen affects the numerical stability, which is also an important factor that needs to be considered in surgical simulation. Currently, the dynamics of soft tissue deformation is commonly obtained by numerical time integration schemes such as the explicit [60, 66] or implicit [3, 102] integrations. In both schemes, the second-order ordinary differential equation governing the dynamics of soft tissue deformation is transformed into a coupled set of two first-order systems by introducing a proxy velocity vector $\dot{\boldsymbol{u}}$, i.e.

$$\begin{cases} \ddot{\boldsymbol{u}} = \dfrac{\dot{\boldsymbol{u}}}{t} \\ \dot{\boldsymbol{u}} = \dfrac{\boldsymbol{u}}{t} \end{cases} \tag{2.1}$$

where $\ddot{\boldsymbol{u}}$, $\dot{\boldsymbol{u}}$ and $\boldsymbol{u}$ are the acceleration, velocity and displacement vectors of a point.

To determine a solution of time-continuous Eq. (2.1), the time-dependent variables $\dot{\boldsymbol{u}}$ and $\ddot{\boldsymbol{u}}$ need to be discretised using a finite difference technique via time increments to determine estimates of the continuous variables [103]. By choosing different finite difference techniques, such as the forward or backward finite difference estimates, an explicit or implicit integration scheme can be obtained [104].

2.4.1 Explicit Integration

In the explicit integration, variables in the future state are explicitly determined from their current state of known values via a numerical time-stepping algorithm. An explicit scheme using forward finite difference estimation can be written as

$$\begin{cases} \ddot{\boldsymbol{u}}^t = \dfrac{\dot{\boldsymbol{u}}^{t+\Delta t} - \dot{\boldsymbol{u}}^t}{\Delta t} \\ \dot{\boldsymbol{u}}^t = \dfrac{\boldsymbol{u}^{t+\Delta t} - \boldsymbol{u}^t}{\Delta t} \end{cases} \rightarrow \begin{cases} \dot{\boldsymbol{u}}^{t+\Delta t} = \dot{\boldsymbol{u}}^t + \Delta t \ddot{\boldsymbol{u}}^t \\ \boldsymbol{u}^{t+\Delta t} = \boldsymbol{u}^t + \Delta t \dot{\boldsymbol{u}}^t \end{cases} \tag{2.2}$$

where the right superscript denotes the current and future time points at t and $t + \Delta t$, respectively, and Δt is the time step size.

The explicit integration is easy to implement and computationally efficient, since variables in the future state are obtained explicitly based on the current state of known values only, which does not require inversion of stiffness matrix at each time step [55]. It is also well suited for distributed parallel computing, since most of the deformation methods for soft tissue deformation employ the mass lumping technique, by which the global system of equations can be split into independent equations for the nodes, allowing each node to be assigned to one processor in the parallel computer and calculation to be performed independently. Despite the improved computational efficiency and simple implementation, the explicit integration exhibits a number of shortcomings. Most important, the solution of explicit integration is only conditionally stable, meaning a careful selection of time step size is needed for the simulation, otherwise explodes numerically, to be stable [11]. The mathematical evaluation of stability of integration schemes can be conducted using the Dahlquist's test equation [105]

$$\dot{y} = \lambda y(t), \quad y(t_0) = y_0 \tag{2.3}$$

where the analytic solution of this equation is the exponential $y(t) = y_0 e^{\lambda t}$.

An integration scheme that yields a bounded solution to Eq. (2.3) is said to be stable. Eq. (2.3) is only bounded when $\Re\mathrm{e}(\lambda) \leq 0$. Using the explicit integration, Eq. (2.3) can be approximated as

$$\dot{y}^n = \frac{y^{n+1} - y^n}{\Delta t} = \lambda y^n \tag{2.4}$$

which can be further rearranged into

$$y^{n+1} = \lambda \Delta t y^n + y^n = (1 + \lambda \Delta t)^{n+1} y_0 \tag{2.5}$$

where the condition for y^{n+1} to be not increased indefinitely is

$$|1 + \lambda \Delta t| \leq 1 \tag{2.6}$$

It can be seen from Eq. (2.6) that the explicit integration is only conditionally stable, and the critical time step Δt is obtained by $\Delta t \leq \frac{2}{|\lambda|}$. In soft tissue deformation, the maximum time step size that can be used for stable simulation is associated with the largest eigenvalue of the stiffness matrix and to the mass and damping values [60, 106]. Various estimations of the critical time step size for stable simulation of soft tissues in explicit

integration were studied, such as the critical time step for linear FEM [107], TLED [56] and meshless method [86]. Due to the stiff equations raised from the nearly incompressibility of biological soft tissues, the maximum time step is often restricted to a small value. Further, considering the soft tissues' viscoelastic effects further decreases the maximum value of the time step size. Owing to these, the solutions of explicit integration to soft tissue deformation usually require more iterations per simulation frame, resulting in inefficient computation.

To address the inefficient computation resulted from using small time steps in explicit integration, various techniques were studied. Cotin *et al.* [60] applied a fourth-order Runge-Kutta explicit integration method for discretising the temporal domain and achieved a larger time step, about 10x larger than the forward Euler method, leading to a speed gain of 2x for surgical simulation. Fierz *et al.* [103] studied a shape matching technique to improve the time step size in the explicit integration. In this approach, under a given desired simulation time step, the ill-shaped elements that cannot be simulated stably are handled specially via a non-physics-based geometric shape matching technique, whereas the remaining well-shaped ones are simulated with a standard deformation model. The elements that require special treatment are identified by computing the eigenmodes of the elements while considering the mutual interactions with neighbouring elements. This hybrid approach enables taking a larger time step than using an explicit integration alone, and the total computational costs per frame are significantly lowered. Taylor *et al.* [108] presented a reduced order explicit dynamics scheme to improve the time step limit. In this approach, the full model configuration is projected onto a low dimensional generalised basis prior to integration of the equilibrium equations, and hence the time integration is performed on a reduced basis, leading to a much larger time step than that of the full system for stable simulation. Despite all the efforts mentioned above, the conditional stability of explicit integration cannot be completely eliminated by these approaches.

2.4.2 Implicit Integration

Compared to explicit integration, the implicit integration is unconditionally stable. In the implicit integration, variables in the future state are determined by considering variables both in the current and future states, leading to a system of equations in which unknown state variable values are implicitly given as solutions. An implicit scheme using the backward finite difference estimation can be written as

$$\begin{cases} \ddot{\boldsymbol{u}}^t = \dfrac{\dot{\boldsymbol{u}}^t - \dot{\boldsymbol{u}}^{t-\Delta t}}{\Delta t} \\ \dot{\boldsymbol{u}}^t = \dfrac{\boldsymbol{u}^t - \boldsymbol{u}^{t-\Delta t}}{\Delta t} \end{cases} \tag{2.7}$$

By writing the index of $\boldsymbol{u}$ by $t \to t + \Delta t$ and $t - \Delta t \to t$, the time-continuous variables $\ddot{\boldsymbol{u}}$, $\dot{\boldsymbol{u}}$ and $\boldsymbol{u}$ can be estimated as

$$\begin{cases} \dot{\boldsymbol{u}}^{t+\Delta t} = \dot{\boldsymbol{u}}^{t} + \Delta t \ddot{\boldsymbol{u}}^{t+\Delta t} \\ \boldsymbol{u}^{t+\Delta t} = \boldsymbol{u}^{t} + \Delta t \dot{\boldsymbol{u}}^{t+\Delta t} \end{cases} \tag{2.8}$$

Similar to the stability verification of the explicit integration using the Dahlquist's test equation, Eq. (2.3) can be approximated using the implicit integration as

$$y^{n+1} = \lambda \Delta t y^{n+1} + y^{n} \rightarrow y^{n+1} = \frac{y^{n}}{(1 - \lambda \Delta t)} = \frac{y_0}{(1 - \lambda \Delta t)^{n+1}} \tag{2.9}$$

where y^{n+1} will not be increased indefinitely if

$$|1 - \lambda \Delta t| \geq 1 \tag{2.10}$$

Equation (2.10) is always true since $\Re\mathrm{e}(\lambda) \leq 0$; therefore, the implicit integration is unconditionally stable for any arbitrarily chosen time step [105]. This attribute provides a unique strength to the implicit integration in handling collisions occurred in tool-tissue interactions and the stiff equations raised from the nearly incompressibility of soft tissues, which enhances the simulation by using a large time step without loss of numerical stability. The time step size is limited only by the considerations of numerical convergence and accuracy. Despite unconditional stability, the downside of implicit integration is that it is computationally more expensive than the explicit counterpart. It requires the solution of a nonlinear system of equations at each load step, which is usually solved by an iterative method based on the Newton-Raphson method through a sequence of solutions of linear equations. The linear system equations can either be solved by directly computing the inverse or a factorisation of the system matrix or iteratively solving a system of algebraic equations based on an initial estimate, both of which lead to an increase in computational time. Mafi and Sirouspour [75] studied and compared the performance of an element-by-element and conventional preconditioned conjugate gradients (PCG) solvers for solving the system equations. It was shown that the element-by-element PCG outperforms the conventional solver at small number of iterations. In implicit integration, iterations also need to be performed for each time step in order to control the numerical errors and prevent divergence [56]. Further, numerical dissipation can become dominant for large time steps, and the computed solution accuracy deteriorates when a large time step is used in low-order schemes [103].

Compared between the two integration schemes, the system response is more global within the implicit approach, whereas the response of the explicit integration to applied forces is only propagated from a node to the whole mesh after multiple iterations [55]. Although the explicit integration can be computationally efficient at finding solutions than the implicit integration thanks to not solving a large system of equations, the time discretisation error will usually accumulate in the explicit scheme [68]. Further, in the case of large deformation of soft tissues, elements can become distorted and ill-conditioned, leading to a reduction in the critical time step size in the explicit integration [52], whereas the implicit integration still remains stable. Explicit integration also tends to converge more slowly than the implicit counterpart, since it is only conditionally stable. Joldes *et al.*

facilitated the convergent rate of explicit integration using a dynamic relaxation (DR) scheme [109], and it was further improved by the adaptive DR [110]. The main idea of DR algorithm is to increase the convergence rate towards the final, deformed state by including a mass proportional numerical damping while sacrificing numerical accuracy in the path along which the deformed state is reached. The proposed DR is computationally efficient in that the main parameters of DR algorithm can be pre-computed. Compared to explicit integration, the implicit integration also helps to obtain robust and realistic behaviours when simulating user tool-tissue interactions, whereas the explicit integration with a much lower time step and large frame rate results in very damped motions [74]. Moreover, the explicit integration does not guarantee that, at each time step, the residual vector is minimised, and hence it cannot ensure that the external and internal forces are balanced [3], whereas the accuracy of the equilibrium equation can be controlled in the implicit integration [111].

3. New ChainMail Algorithms

In this chapter, three new ChainMail algorithms are proposed to improve the modelling realism and computational performance of traditional ChainMail algorithms. Chapter 3.1 first presents an overview of the traditional ChainMail, followed by three new ChainMail algorithms presented in Chapters 3.2, 3.3 and 3.4, respectively. The novelties of the proposed ChainMails are presented as follows:

- **Time-Saving Volume-Energy-Conversed ChainMail Algorithm (Chapter 3.2):** The proposed method can (i) accommodate various material properties; (ii) improve computational performance for isotropic and homogeneous materials; and (iii) conserve volume and strain energy.
- **Ellipsoid Bounding Region-based ChainMail Algorithm (Chapter 3.3):** The proposed method can (i) overcome the conflict of the concept of principle strains in continuum mechanics to control the movement of chain elements; (ii) conserve linear and angular momentums and improve deformation realism; and (iii) enable model dynamics for dynamic soft tissue deformation.
- **Neural Dynamics-based ChainMail Algorithm (Chapter 3.4):** The proposed method can (i) avoid the complex computation of elasticity; (ii) simulate soft tissues' nonlinear deformation and the typical mechanical behaviours; and (iii) simulate the dynamics of soft tissue deformation via neural dynamics of the cellular neural network.

3.1 Traditional ChainMail Algorithm

From the perspective of continuum mechanics of elasticity, the traditional ChainMail algorithm [24, 34] is equivalent to a spring system. As shown in Fig. 3.1, a spring of length l_0 at the rest state can be compressed to a minimum compression length l_{min} or extended to a maximum extension length l_{max}. Therefore, the movement of the spring is bounded by these two limits.

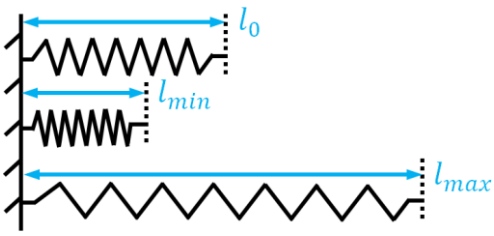

Figure 3.1 A spring of rest length l_0 can be compressed to a minimum length l_{min} or extended to a maximum length l_{max}.

Traditional ChainMail algorithms, such as the 3D ChainMail [24] and the generalised ChainMail [34], employ geometric limits, forming a box-shaped bounding region (BSBR), to control the movement of chain elements in the object. As illustrated in Fig. 3.2, for any two connected chain elements i and j with their respective positions denoted by $\mathbf{P_i}(x_i, y_i, z_i)$ and $\mathbf{P_j}(x_j, y_j, z_j)$, the $\mathrm{BSBR}_{j,i}$ for chain element j with respect to chain element i is defined by geometric limits $x_{j,i\ limit}$, $y_{j,i\ limit}$ and $z_{j,i\ limit}$, which are the maximum allowable moving distances of chain element j in the x, y and z directions, respectively.

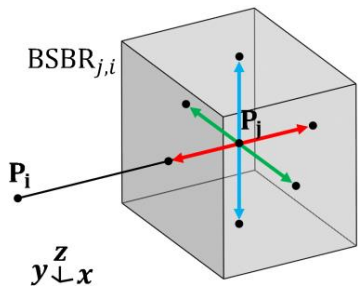

Figure 3.2 The $\mathrm{BSBR}_{j,i}$ is a box-shaped bounding region defined by three geometric limits $x_{j,i\ limit}$ (red), $y_{j,i\ limit}$ (green) and $z_{j,i\ limit}$ (blue) for chain element j with respect to chain element i, with their positions denoted by $\mathbf{P_j}$ and $\mathbf{P_i}$, respectively.

The $\mathrm{BSBR}_{j,i}$ for chain element j with respect to chain element i is given by

$$\mathrm{BSBR}_{j,i} = \{x_{j,i\ min} \leq x_j \leq x_{j,i\ max}; y_{j,i\ min} \leq y_j \leq y_{j,i\ max}; z_{j,i\ min} \leq z_j \leq z_{j,i\ max}\} \tag{3.1}$$

where $x_{j,i\ min}$, $y_{j,i\ min}$ and $z_{j,i\ min}$ are the minimum compressions, and $x_{j,i\ max}$, $y_{j,i\ max}$ and $z_{j,i\ max}$ are the maximum extensions in the x, y and z axis directions, respectively.

With the three geometric limits, the minimum compression $x_{j,i\ min}$ and maximum extension $x_{j,i\ max}$ are expressed as

$$x_{j,i\ min} = x_i + \Delta x_{j,i} - x_{j,i\ limit} \tag{3.2}$$

$$x_{j,i\ max} = x_i + \Delta x_{j,i} + x_{j,i\ limit}$$

which may be further formulated according to the generalised ChainMail [34] as

$$x_{j,i\,min} = x_i + \alpha_{min}\Delta x_{j,i} - \beta\left(\Delta y_{j,i} + \Delta z_{j,i}\right) \tag{3.3}$$

$$x_{j,i\,max} = x_i + \alpha_{max}\Delta x_{j,i} + \beta\left(\Delta y_{j,i} + \Delta z_{j,i}\right)$$

where α_{min}, α_{max} and β are the material parameters; and $\Delta x_{j,i}$, $\Delta y_{j,i}$ and $\Delta z_{j,i}$ are geometric distances between chain elements i and j with respect to the x, y and z axes at the rest state, respectively, i.e. $\Delta x_{j,i} = |x_j - x_i|$, where the symbol "|·|" denotes the modulus of a vector component. The minimum compression and maximum extension in the other two directions, i.e. $y_{j,i\,min}$, $y_{j,i\,max}$, $z_{j,i\,min}$ and $z_{j,i\,max}$, can be expressed in a similar manner.

The minimum compression and maximum extension along an axis direction define the limits of compression and extension of a chain element along this axis direction. If any of these limits is violated, the chain element violating the limit will be moved in the corresponding axis direction to maintain its position within the BSBR, such that the projection of the chain link connecting the two chain elements on that axis direction is always bounded by the two limits. Consider the chain element i is now moved from position $\mathbf{P_i}$ to a new position $\mathbf{P_i^*}(x_{i^*}, y_{i^*}, z_{i^*})$ and enforces a new BSBR_{j,i^*}. The BSBR_{j,i^*} for chain element j with respect to the new position $\mathbf{P_i^*}$ of chain element i can be written in a similar manner as Eq. (3.1), and it is given by

$$\mathrm{BSBR}_{j,i^*} = \{x_{j,i^*\,min} \le x_j \le x_{j,i^*\,max}; y_{j,i^*\,min} \le y_j \le y_{j,i^*\,max}; z_{j,i^*\,min} \le z_j \le z_{j,i^*\,max}\} \tag{3.4}$$

The minimum compression $x_{j,i^*\,min}$ and maximum extension $x_{j,i^*\,max}$ in the x axis direction of the new BSBR_{j,i^*} can be calculated by

$$x_{j,i^*\,min} = x_{i^*} + \alpha_{min}\Delta x_{j,i} - \beta\left(\Delta y_{j,i} + \Delta z_{j,i}\right) \tag{3.5}$$

$$x_{j,i^*\,max} = x_{i^*} + \alpha_{max}\Delta x_{j,i} + \beta\left(\Delta y_{j,i} + \Delta z_{j,i}\right)$$

If x_j is outside of the limits defined by Eq. (3.5), the chain element j will be adjusted in the x axis direction such that

$$\text{if } \left(x_j < x_{j,i^*\,min}\right), x_{j^*,i^*} = x_{j,i^*\,min} \tag{3.6}$$

$$\text{if } \left(x_j > x_{j,i^*\,max}\right), x_{j^*,i^*} = x_{j,i^*\,max}$$

where x_{j^*,i^*} is the x component of the new position $\mathbf{P_j^*}(x_{j^*,i^*}, y_{j^*,i^*}, z_{j^*,i^*})$ of chain element j adjusted from $\mathbf{P_j}$, due to the movement of chain element i from position $\mathbf{P_i}$ to $\mathbf{P_i^*}$, which is illustrated in Fig. 3.3. The position adjustments in the other two axis directions are performed in a similar manner.

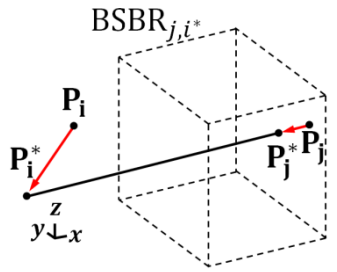

Figure 3.3 The position of chain element j is adjusted from $\mathbf{P_j}$ to $\mathbf{P_j^*}$ to satisfy the BSBR$_{j,i^*}$ enforced by the chain element i at its new position $\mathbf{P_i^*}$ which is moved from $\mathbf{P_i}$.

The position adjustments of the traditional ChainMails result in a deformation that is propagated in the object from the chain element being manipulated to the others via chain links. The deformation propagation between chain elements in 1D is illustrated in Fig. 3.4.

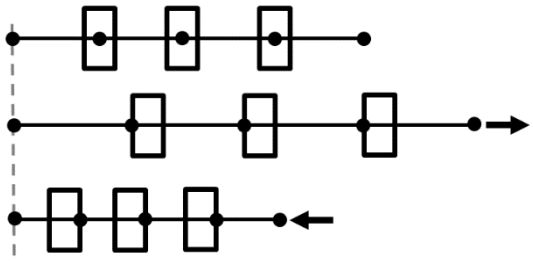

Figure 3.4 Propagation of deformation in a 1D ChainMail model, where the BSBR is indicated by a black box: (top) the rest state; (middle) maximally extended; and (bottom) minimally compressed.

3.2 Time-Saving Volume-Energy-Conserved ChainMail Algorithm

Traditional ChainMails employ constant values for material parameters α_{min}, α_{max} and β throughout the entire volumetric object, leading to the failure in accommodating nonlinear material properties such as anisotropy and heterogeneity. In addition, despite various improvements on the traditional ChainMails [27, 29], the method still lacks the capability in modelling of soft tissues' incompressibility and relaxation behaviours, due to the lack of volume and strain energy conservation. Therefore, a new ChainMail algorithm named time-saving volume-energy-conserved (TSVE) ChainMail is proposed in this chapter to address these issues. The proposed algorithm enables the use of different material properties for chain elements to accommodate various materials. Based on the new BSBR, a time-saving scheme is developed to improve computational performance for isotropic and homogeneous materials. The proposed algorithm can also conserve volume and strain energy.

3.2.1 New Box-Shaped Bounding Region

The minimum compression $x_{j,i\,min}$ and maximum extension $x_{j,i\,max}$ in the x axis direction of the new $\mathrm{BSBR}_{j,i}$ in the proposed TSVE-ChainMail are defined as

$$x_{j,i\,min} = x_i + \Delta x_{j,i} - \frac{\alpha_i + \alpha_j}{2}\left(\Delta x_{j,i} + \Delta y_{j,i} + \Delta z_{j,i}\right) \tag{3.7}$$

$$x_{j,i\,max} = x_i + \Delta x_{j,i} + \frac{\alpha_i + \alpha_j}{2}\left(\Delta x_{j,i} + \Delta y_{j,i} + \Delta z_{j,i}\right)$$

where α_i and α_j are the material parameters of chain elements i and j, respectively, and they are corresponded to the spring stiffness k of the material.

For isotropic and homogeneous materials, where $\alpha_i = \alpha_j = \alpha$, the above equations may be simplified to

$$x_{j,i\,min} = x_i + (1 - \alpha)\Delta x_{j,i} - \alpha(\Delta y_{j,i} + \Delta z_{j,i}) \tag{3.8}$$

$$x_{j,i\,max} = x_i + (1 + \alpha)\Delta x_{j,i} + \alpha(\Delta y_{j,i} + \Delta z_{j,i})$$

Anisotropic and heterogeneous materials can be modelled by setting different parameter values in different directions and different regions, respectively, which were unable to achieve with the traditional ChainMails.

3.2.2 Time Saving Scheme for Isotropic and Homogeneous Materials

A time saving scheme (TSS) is developed for isotropic and homogeneous materials of constant material parameter α, where each chain element can be considered only once in every iteration, leading to improved computational efficiency. Consider three general cases of chain elements' movement illustrated in Fig. 3.5:

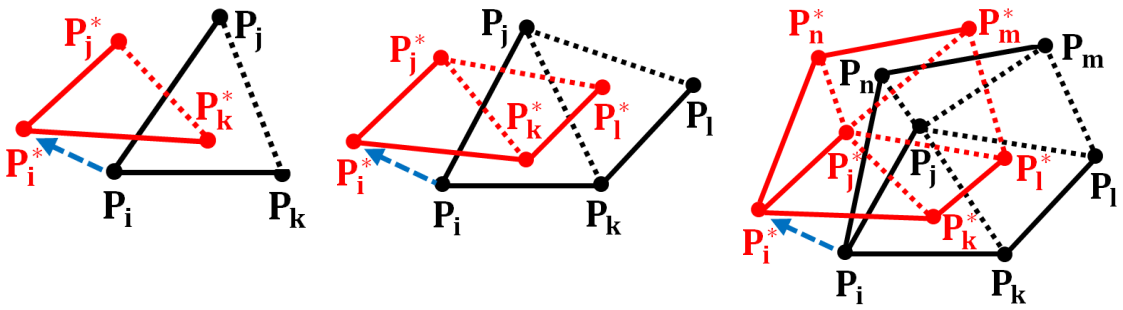

(a) (b) (c)

Figure 3.5 Chain element i is moved from $\mathbf{P_i}$ to a new position $\mathbf{P_i^*}$ (blue arrow) while others follow its movement; the rest state is shown in black, whereas the new positions are shown in red; the solid line indicates that the two chain elements are connected and one is moved directly with respect to the other, whereas the dotted line indicates that the elements are connected but one does not move with respect to the other.

- **Case (1):** Following $\mathbf{P_i}$'s movement to $\mathbf{P_i^*}$, chain elements j and k are moved to $\mathbf{P_j^*}$ and $\mathbf{P_k^*}$, respectively (see Fig. 3.5(a)). Then $\mathbf{P_j^*}$ and $\mathbf{P_k^*}$ stay within their respective BSBRs;
- **Case (2):** Following $\mathbf{P_k}$'s movement to $\mathbf{P_k^*}$ in **Case (1)**, chain element l is moved to $\mathbf{P_l^*}$ (see Fig. 3.5(b)). Then $\mathbf{P_j^*}$ and $\mathbf{P_l^*}$ stay within their respective BSBRs;
- **Case (3):** In addition to $\mathbf{P_i}$, $\mathbf{P_j}$, $\mathbf{P_k}$ and $\mathbf{P_l}$'s movements, chain element n is moved to $\mathbf{P_n^*}$ following $\mathbf{P_i}$'s movement to $\mathbf{P_i^*}$, and chain element m is moved to $\mathbf{P_m^*}$ following $\mathbf{P_n}$'s movement (see Fig. 3.5(c)). Then $\mathbf{P_l^*}$ and $\mathbf{P_m^*}$ stay within their respective BSBRs.

3.2.2.1 Proof of Case (1)

Case (1) will be verified if $\mathbf{P_j^*}(x_{j^*,i^*}, y_{j^*,i^*}, z_{j^*,i^*})$ stays within the BSBR_{j^*,k^*} with respect to $\mathbf{P_k^*}$, and $\mathbf{P_k^*}$ stays within the BSBR_{k^*,j^*} with respect to $\mathbf{P_j^*}$. Since the exact positions of $\mathbf{P_j^*}$ and $\mathbf{P_k^*}$ are unknown, the maximum and minimum limits (two limits), $\mathbf{P_{k,max}^*}(x_{k^*,i^*\,max}, y_{k^*,i^*\,max}, z_{k^*,i^*\,max})$ and $\mathbf{P_{k,min}^*}(x_{k^*,i^*\,min}, y_{k^*,i^*\,min}, z_{k^*,i^*\,min})$ of $\mathbf{P_k^*}$, are used for verification of **Case (1)**. Denote the BSBR_{j^*,k^*} at the two limits of $\mathbf{P_k^*}$ by $\overline{\mathrm{BSBR}_{j^*,k^*}}$. Thus,

$$\overline{\mathrm{BSBR}_{j^*,k^*}} = \{\overline{x_{j^*,k^*\,min}} \le x_{j^*,i^*} \le \overline{x_{j^*,k^*\,max}}; \overline{y_{j^*,k^*\,min}} \le y_{j^*,i^*} \le \overline{y_{j^*,k^*\,max}}; \overline{z_{j^*,k^*\,min}} \le z_{j^*,i^*} \le \overline{z_{j^*,k^*\,max}} \quad (3.9)$$

Substituting $x_{i^*} = x_{k,i^*\,min} - (1-\alpha)\Delta x_{k,i} + \alpha(\Delta y_{k,i} + \Delta z_{k,i})$ into the lower limit $x_{j^*,i^*} \ge x_{j,i^*\,min} = x_{i^*} + (1-\alpha)\Delta x_{j,i} - \alpha(\Delta y_{j,i} + \Delta z_{j,i})$ to replace x_{i^*} yields

$$x_{j^*,i^*} \geq x_{k,i^*\,min} - (1-\alpha)\Delta x_{k,i} + \alpha(\Delta y_{k,i} + \Delta z_{k,i}) + (1-\alpha)\Delta x_{j,i} - \alpha(\Delta y_{j,i} + \Delta z_{j,i}) \tag{3.10}$$

Using geometric distance $\Delta x_{j,i} = |x_j - x_i|$, at lower limit $x_{k,i^*\,min} = x_{k^*,i^*\,min}$, the above equation may be simplified to

$$\begin{aligned} x_{j^*,i^*} \geq x_{k,i^*\,min} + (1-\alpha)\Delta x_{j,k} - \alpha(\Delta y_{j,k} + \Delta z_{j,k}) &= x_{k^*,i^*\,min} + (1-\alpha)\Delta x_{j,k} - \alpha(\Delta y_{j,k} + \Delta z_{j,k}) \\ &= \overline{x_{j^*,k^*\,min}} \end{aligned} \tag{3.11}$$

A similar calculation can be made for $\overline{x_{j^*,k^*\,max}}$, $\overline{y_{j^*,k^*\,min}}$, $\overline{y_{j^*,k^*\,max}}$, $\overline{z_{j^*,k^*\,min}}$, $\overline{z_{j^*,k^*\,max}}$, and for BSBR_{k^*,j^*}. Therefore, it is demonstrated that $\mathbf{P_j^*}$ always stays within the BSBR_{j^*,k^*} with respect to $\mathbf{P_k^*}$, and vice versa.

3.2.2.2 Proof of Case (2)

Case (2) will be verified if $\mathbf{P_l^*}(x_{l^*,k^*}, y_{l^*,k^*}, z_{l^*,k^*})$ stays within the BSBR_{l^*,j^*} with respect to $\mathbf{P_j^*}$, and $\mathbf{P_j^*}$ stays within the BSBR_{j^*,l^*} with respect to $\mathbf{P_l^*}$. Denote the BSBR_{l^*,j^*} at the two limits of $\mathbf{P_j^*}$ by $\overline{\text{BSBR}_{l^*,j^*}}$. Thus,

$$\overline{\text{BSBR}_{l^*,j^*}} = \{\overline{x_{l^*,j^*\,min}} \leq x_{l^*,k^*} \leq \overline{x_{l^*,j^*\,max}}; \overline{y_{l^*,j^*\,min}} \leq y_{l^*,k^*} \leq \overline{y_{l^*,j^*\,max}}; \overline{z_{l^*,j^*\,min}} \leq z_{l^*,k^*} \leq \overline{z_{l^*,j^*\,max}} \tag{3.12}$$

Consider the lower limit $x_{l^*,k^*} \geq x_{l,k^*\,min} = x_{k^*,i^*} + (1-\alpha)\Delta x_{l,k} - \alpha(\Delta y_{l,k} + \Delta z_{l,k})$; substituting x_{k^*,i^*} by $x_{k^*,i^*\,min} = \overline{x_{j^*,k^*\,min}} - (1-\alpha)\Delta x_{j,k} + \alpha(\Delta y_{j,k} + \Delta z_{j,k})$ from Eq. (3.11) yields

$$x_{l^*,k^*} \geq \overline{x_{j^*,k^*\,min}} - (1-\alpha)\Delta x_{j,k} + \alpha(\Delta y_{j,k} + \Delta z_{j,k}) + (1-\alpha)\Delta x_{l,k} - \alpha(\Delta y_{l,k} + \Delta z_{l,k}) \tag{3.13}$$

Using the geometric distance, the above equation may be simplified to

$$x_{l^*,k^*} \geq \overline{x_{j^*,k^*\,min}} + (1-\alpha)\Delta x_{l,j} - \alpha(\Delta y_{l,j} + \Delta z_{l,j}) \tag{3.14}$$

Based on Eqs. (3.6) and (3.11), $x_{j^*,i^*} \geq x_{j,i^*\,min}$ and $x_{j^*,i^*} \geq \overline{x_{j^*,k^*\,min}}$. At the lower limit of x_{j^*,i^*}, $\overline{x_{j^*,k^*\,min}} = x_{j,i^*\,min}$. Further, at lower limit $x_{j,i^*\,min} = x_{j^*,i^*\,min}$. Thus,

$$\begin{aligned} x_{l^*,k^*} \geq x_{j,i^*\,min} + (1-\alpha)\Delta x_{l,j} - \alpha(\Delta y_{l,j} + \Delta z_{l,j}) &= x_{j^*,i^*\,min} + (1-\alpha)\Delta x_{l,j} - \alpha(\Delta y_{l,j} + \Delta z_{l,j}) \\ &= \overline{x_{l^*,j^*\,min}} \end{aligned} \tag{3.15}$$

A similar calculation can be made for the other boundary limits, and for BSBR_{j^*,l^*}. Therefore, it is demonstrated that $\mathbf{P_l^*}$ stays within the BSBR_{l^*,j^*} with respect to $\mathbf{P_j^*}$, and vice versa.

3.2.2.3 Proof of Case (3)

Case (3) will be verified if $\mathbf{P_m^*}(x_{m^*,n^*}, y_{m^*,n^*}, z_{m^*,n^*})$ stays within the BSBR_{m^*,l^*} with respect to $\mathbf{P_l^*}$, and $\mathbf{P_l^*}$ stays within the BSBR_{l^*,m^*} with respect to $\mathbf{P_m^*}$. Denote the BSBR_{l^*,m^*} at the two limits of $\mathbf{P_m^*}$ by $\overline{\text{BSBR}_{l^*,m^*}}$. Thus,

$$\overline{\text{BSBR}_{l^*,m^*}} = \{\overline{x_{l^*,m^*\,min}} \le x_{l^*,k^*} \le \overline{x_{l^*,m^*\,max}}; \overline{y_{l^*,m^*\,min}} \le y_{l^*,k^*} \le \overline{y_{l^*,m^*\,max}}; \overline{z_{l^*,m^*\,min}} \le z_{l^*,k^*} \le \overline{z_{l^*,m^*\,max}} \tag{3.16}$$

Similar to the determination of $\overline{x_{l^*,j^*\,min}}$ in Eq. (3.15), the calculation of $\overline{x_{m^*,j^*\,min}}$ can be represented by

$$\overline{x_{m^*,j^*\,min}} = x_{j^*,i^*\,min} + (1-\alpha)\Delta x_{m,j} - \alpha(\Delta y_{m,j} + \Delta z_{m,j}) \tag{3.17}$$

Substituting $x_{j^*,i^*\,min} = \overline{x_{m^*,j^*\,min}} - (1-\alpha)\Delta x_{m,j} + \alpha(\Delta y_{m,j} + \Delta z_{m,j})$ into Eq. (3.15) yields

$$x_{l^*,k^*} \ge \overline{x_{m^*,j^*\,min}} - (1-\alpha)\Delta x_{m,j} + \alpha(\Delta y_{m,j} + \Delta z_{m,j}) + (1-\alpha)\Delta x_{l,j} - \alpha(\Delta y_{l,j} + \Delta z_{l,j}) \tag{3.18}$$

Similar to $x_{l^*,k^*} \ge \overline{x_{l^*,j^*\,min}}$ in Eq. (3.15), $x_{m^*,n^*} \ge \overline{x_{m^*,j^*\,min}}$. At lower limit of x_{m^*,n^*}, $\overline{x_{m^*,j^*\,min}} = x_{m,n^*\,min}$. Further, at lower limit $x_{m,n^*\,min} = x_{m^*,n^*\,min}$. Thus,

$$\begin{aligned} x_{l^*,k^*} &\ge x_{m,n^*\,min} + (1-\alpha)\Delta x_{l,m} - \alpha(\Delta y_{l,m} + \Delta z_{l,m}) \\ &= x_{m^*,n^*\,min} + (1-\alpha)\Delta x_{l,m} - \alpha(\Delta y_{l,m} + \Delta z_{l,m}) = \overline{x_{l^*,m^*\,min}} \end{aligned} \tag{3.19}$$

A similar calculation can be made for the other boundary limits, and for BSBR_{m^*,l^*}. Therefore, it is demonstrated that $\mathbf{P_l^*}$ stays within the BSBR_{l^*,m^*} with respect to $\mathbf{P_m^*}$, and vice versa.

3.2.2.4 Three Remarks

From the above three proofs, the following three remarks can be drawn. For any three neighbouring chain elements **A**, **B** and **C**:

- [**Remark 1]** if **A** and **B** are moved with respect to **C**, then **A** and **B** stay within their respective BSBRs (the case of $\mathbf{P_i^*}$, $\mathbf{P_j^*}$and $\mathbf{P_k^*}$ in Fig. 3.5(a)).
- **[Remark 2]** if only **A** is moved with respect to **C** while **B** and **C** have been previously moved as per Remark 1, then **A** and **B** stay within their respective BSBRs (the case of $\mathbf{P_j^*}$, $\mathbf{P_k^*}$and $\mathbf{P_l^*}$ in Fig. 3.5(b)).
- **[Remark 3]** if **A** and **C** as well as **B** and **C** have been previously moved as per Remark 2, then **A** and **B** stay within their respective BSBRs (the case of $\mathbf{P_j^*}$, $\mathbf{P_l^*}$and $\mathbf{P_m^*}$ in Fig. 3.5(c)).

The three remarks demonstrate that the chain elements always satisfy the BSBRs with respect to each other in isotropic and homogeneous materials. Therefore, each chain element can be considered only once at each iteration, saving computational time. It should be noted that boundary conditions can be enforced by specifying displacement values to chain elements at the boundary of the problem domain.

3.2.3 Volume and Strain Energy Conservation

Since most biological soft tissues are nearly incompressible [112], and there is a change in strain energy when soft tissues are deformed by an external force, the conservation of volume and strain energy are enforced by using a position adjustment $\Delta\mathbf{P}$ for realistic soft tissue deformation. This position adjustment is derived based on the conditions of conservation of volume and energy [113, 114].

$$\Delta\mathbf{P_i} = \frac{w_i C(\mathbf{P_0}, \dots, \mathbf{P_n})}{\sum_{j=1}^{4} w_j \left\| \nabla_{\mathbf{P_j}} C(\mathbf{P_0}, \dots, \mathbf{P_n}) \right\|^2} \nabla_{\mathbf{P_i}} C(\mathbf{P_0}, \dots, \mathbf{P_n}) \tag{3.20}$$

$$C(\mathbf{P_0}, \dots, \mathbf{P_n}) = C_{volume}(\mathbf{P_0}, \mathbf{P_1}, \mathbf{P_2}, \mathbf{P_3}) = \frac{1}{6} \|(\mathbf{P_1} - \mathbf{P_0}) \cdot ((\mathbf{P_2} - \mathbf{P_0}) \times (\mathbf{P_3} - \mathbf{P_0}))\| - V_0 \tag{3.21}$$

$$C(\mathbf{P_0}, \dots, \mathbf{P_n}) = C_{energy}(\mathbf{P_0}, \mathbf{P_1}, \mathbf{P_2}, \mathbf{P_3}) = \frac{1}{2} \sum_{i=0}^{3} k_i (\|\mathbf{P_C} - \mathbf{P_i}\| - l_{ic}^0)^2 \tag{3.22}$$

where w_i and w_j are the inverse of masses of respective chain elements; $C(\cdot)$ is the condition, the condition of conservation of volume $C_{volume}(\mathbf{P_0}, \mathbf{P_1}, \mathbf{P_2}, \mathbf{P_3})$ and energy $C_{energy}(\mathbf{P_0}, \mathbf{P_1}, \mathbf{P_2}, \mathbf{P_3})$ are employed; $\mathbf{P_0}, \mathbf{P_1}, \mathbf{P_2}, \mathbf{P_3}$ are the four vertices of a tetrahedron; $\nabla_{\mathbf{P_i}} C(\cdot)$ is the gradient vector of $C(\cdot)$ at position $\mathbf{P_i}$; the symbol "$\|\cdot\|$" denotes the modulus of a vector; V_0 is the volume of the tetrahedron at rest state; k_i is the stiffness associated with chain element i; $\mathbf{P_C}$ is the barycentre of the tetrahedron; and l_{ic}^0 is the rest length of $\overrightarrow{\mathbf{P_i}\mathbf{P_C}}$.

3.2.4 Results

A prototype surgical simulation system has been implemented with the proposed TSVE-ChainMail. Experiments are conducted to evaluate the performance of the proposed method in terms of soft tissue material properties, computational time, and volume and strain energy conservation.

3.2.4.1 Isotropic and Homogeneous, Anisotropic and Heterogeneous Deformations

Fig. 3.6 illustrates the deformations of an isotropic and homogeneous, an anisotropic and a heterogeneous material. The cube model is deformed evenly for an isotropic and homogeneous material in Fig. 3.6(a), deformed more significantly in one direction than the others in Fig. 3.6(b), and deformed differently at different regions in Fig. 3.6(c).

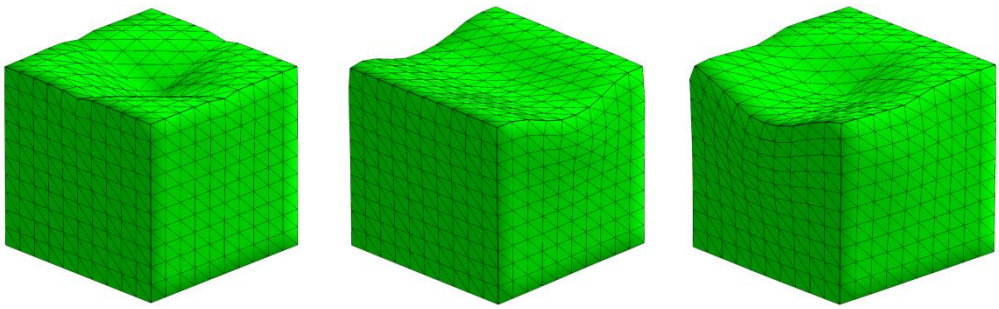

(a) (b) (c)

Figure 3.6 (a) Isotropic and homogeneous, (b) anisotropic and (c) heterogeneous deformations.

3.2.4.2 Computational Performance

The computational performance is evaluated on an Intel(R) Core(TM) i7-4700 CPU@3.40 GHz PC running Visual Studio 2015 in debug mode. Experiments are conducted under same conditions to compare the timing performances with and without the use of TSS for isotropic and homogeneous materials. As illustrated in Fig. 3.7, the computational time with the use of TSS is less than that without TSS for isotropic and homogeneous materials. A computational gain of 29.4% is achieved for real-time visual refresh rate (30 Hz) in terms of the number of moved chain elements.

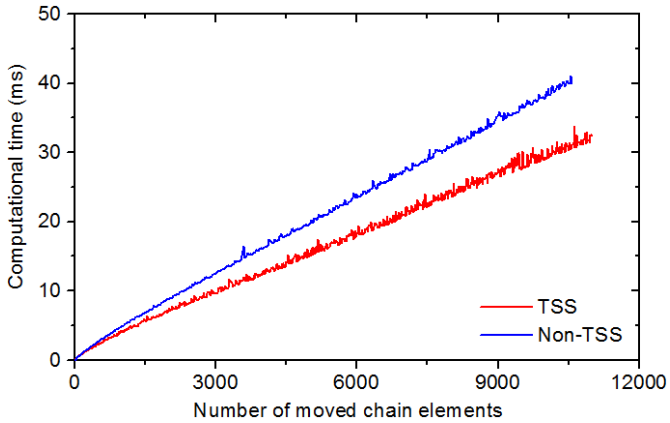

Figure 3.7 Computational time of the proposed ChainMail with and without TSS for isotropic and homogeneous materials.

3.2.4.3 Volume Conservation

Volume conservation has been achieved with the proposed ChainMail. As shown in Fig. 3.8, the proposed ChainMail conserves the object's volume considerably better than the traditional ChainMails which has a significant volume loss after deformation. The volume change after deformation was 0.71% for the TSVE-ChainMail, whereas it was 14.31% for the traditional ChainMails.

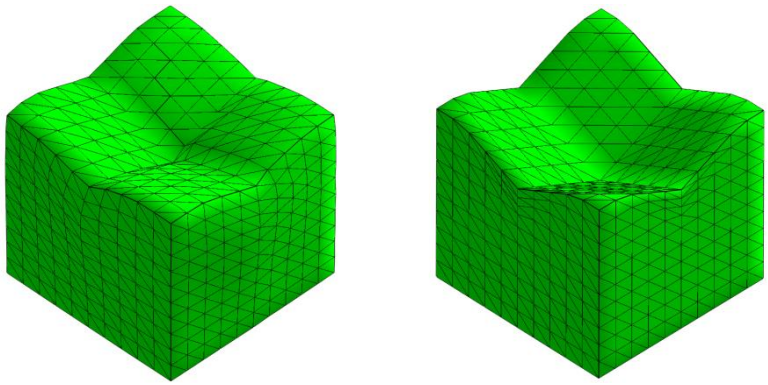

(a) (b)

Figure 3.8 Comparison between the (a) proposed TSVE-ChainMail and (b) traditional ChainMails in terms of volume conservation.

3.2.4.4 Soft Tissue Deformation and Strain Energy Conservation

Interactive deformation of virtual human organs with force feedback has been achieved with the proposed method. Fig. 3.9(a) illustrates the deformation process of a volumetric kidney model by a virtual probe. The strain energy conservation is presented in Figs. 3.9(b)-(d): the kidney model returned to its original state with the proposed ChainMail, whereas the traditional ChainMails failed to do so. It is also noticed that a significant visual improvement has been achieved with the proposed method.

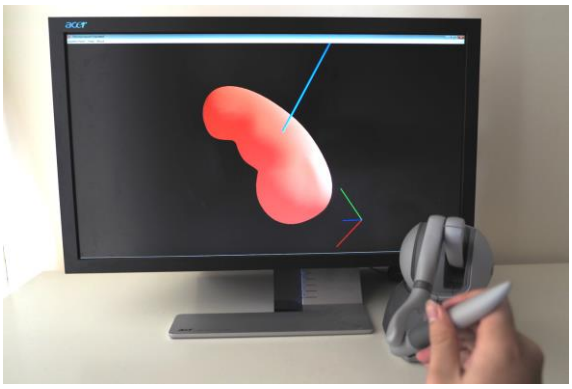

(a) prototype surgical simulation system

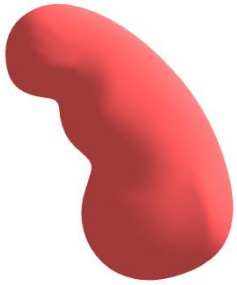

(b) virtual kidney model at the rest state

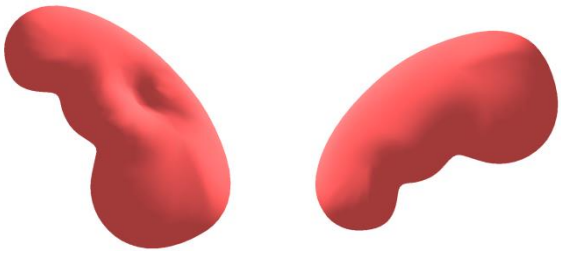

(i) force applied (ii) force released

(c) TSVE-ChainMail

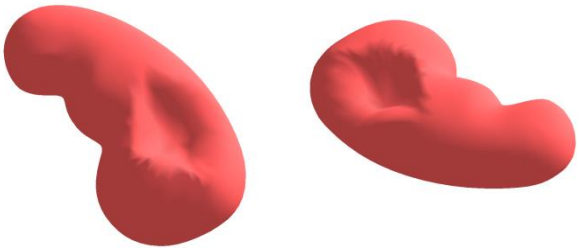

(i) force applied (ii) force released

(d) Traditional ChainMails

Figure 3.9 Comparison between the two ChainMails in terms of strain energy conservation: the kidney model with the TSVE-ChainMail can return to its original state once the external force is released, whereas the traditional ChainMails fails to do so.

3.3 Ellipsoid Bounding Region-based ChainMail Algorithm

In previous chapter, the traditional ChainMail algorithms are improved by considering material properties and

volume and strain energy conservation [45]. Despite improved modelling realism, the ChainMail algorithm still suffers from three major deficiencies such as (i) the conflict of the concept of principle strains in continuum mechanics; (ii) the violation of linear and angular momentum conservation; and (iii) the lack of model dynamics in the temporal domain, leading to limited modelling realism.

In this chapter, the above three deficiencies of the ChainMail algorithm are addressed. Unlike the traditional ChainMails using the box-shaped bounding region, the proposed method defines an ellipsoid-shaped bounding region according to the concept of principle strains in continuum mechanics to control the movement of chain elements. Based on the ellipsoid-shaped bounding region, new position adjustment rules are developed, leading to conservation of linear and angular momentums and improved deformation realism. Further, rather than based on a static update process for deformation in the traditional ChainMails, the proposed method integrates temporal-domain model dynamics to enable ChainMail algorithm to handle dynamic behaviours for soft tissue deformation. Isotropic and homogeneous, anisotropic and heterogeneous materials can be easily accommodated by simple modification of strain limits. Experimental results demonstrate that the proposed ChainMail can simulate the typical mechanical behaviours of soft tissues, accommodate isotropic and homogeneous, anisotropic and heterogeneous materials, and handle large deformation. The proposed ChainMail requires only small computational time, capable of achieving real-time performance.

3.3.1 Three Deficiencies of the Traditional ChainMail Algorithm

Traditional ChainMail algorithm is easy to implement and computationally inexpensive; however, it suffers from three major deficiencies, resulting in limited physical accuracy.

3.3.1.1 First Deficiency

First, the BSBR used in the traditional ChainMails conflicts with the concept of principle strains in continuum mechanics. For a given state of strain at a point **P**, if the relative extension (i.e. strain) ε is of extremum in a direction **n** (n_x, n_y, n_z), then ε is the principle strain at point **P**, and **n** is the principle strain direction associated with ε. The principle strain ε can be obtained by solving

$$\begin{vmatrix} (\varepsilon_{xx}-\varepsilon) & \frac{1}{2}\gamma_{xy} & \frac{1}{2}\gamma_{xz} \\ \frac{1}{2}\gamma_{xy} & (\varepsilon_{yy}-\varepsilon) & \frac{1}{2}\gamma_{yz} \\ \frac{1}{2}\gamma_{xz} & \frac{1}{2}\gamma_{yz} & (\varepsilon_{zz}-\varepsilon) \end{vmatrix} = 0 \tag{3.23}$$

where ε_{xx}, ε_{yy} and ε_{zz} are the normal strains parallel to the x, y and z axes, respectively, and γ_{xy}, γ_{xz} and γ_{yz} are the shear strains in the xy, xz and yz planes, respectively.

The principle strain direction **n** associated with principle strain ε can be obtained by substituting ε into the following equation and solving for n_x, n_y and n_z.

$$(\varepsilon_{xx}-\varepsilon)n_x + \frac{1}{2}\gamma_{xy}n_y + \frac{1}{2}\gamma_{xz}n_z = 0 \tag{3.24}$$

$$\frac{1}{2}\gamma_{xy}n_x + (\varepsilon_{yy}-\varepsilon)n_y + \frac{1}{2}\gamma_{yz}n_z = 0$$

$$\frac{1}{2}\gamma_{xz}n_x + \frac{1}{2}\gamma_{yz}n_y + (\varepsilon_{zz}-\varepsilon)n_z = 0$$

In order to solve the above equations, n_x, n_y and n_z must satisfy the following condition [115]

$$n_x^2 + n_y^2 + n_z^2 = 1 \tag{3.25}$$

However, the BSBR used in the traditional ChainMails violates the above condition. Consider a point in the $\mathrm{BSBR}_{j,i}$, its x component can be expressed by

$$x_{j,i} = x_i + \Delta x_{j,i} - n_x x_{j,i\ limit} \tag{3.26}$$

The maximum extension $x_{j,i\ max}$ and minimum compression $x_{j,i\ min}$ in the x axis direction of the $\mathrm{BSBR}_{j,i}$ are reached when $n_x = 1$ and -1, respectively. Similarly, the limits in the other two directions are reached when $n_y = \pm 1$ and $n_z = \pm 1$. Therefore, the boundary of the BSBR where the maximum extension and minimum compression occur may be written as

$$n_x = \begin{cases} 1 \\ -1 \end{cases} \text{while } n_y, n_z \in [-1, 1] \tag{3.27}$$

$$n_y = \begin{cases} 1 \\ -1 \end{cases} \text{while } n_x, n_z \in [-1, 1]$$

$n_z = \begin{cases} 1 \\ -1 \end{cases}$ while $n_x, n_y \in [-1, 1]$

Eq. (3.25) represents a unit sphere, whereas Eq. (3.27) a cube in 3D. As shown in Fig. 3.10, in 2D with $n_z = 0$, Eq. (3.25) represents a unit circle and Eq. (3.27) a square with unit length and width. Therefore, it can be seen that the BSBR (red square) used in the traditional ChainMails does not comply with the condition of principle strains (blue circle).

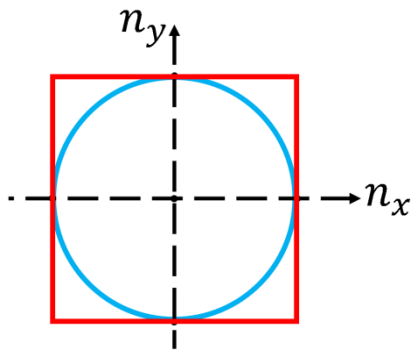

Figure 3.10 The BSBR and the condition of principle strains in 2D in terms of n_x and n_y: the red square indicates the BSBR, whereas the blue circle indicates the condition of principle strains.

3.3.1.2 Second Deficiency

The second deficiency of the traditional ChainMails is that the position adjustments violate the conservation of linear and angular momentums. The conservation of linear momentum, conservation of angular momentum, and conservation of mass are the three fundamental laws of mechanics [116], and they must be satisfied at every point in the problem domain. The conservation of mass is automatically satisfied in the ChainMail since the Lagrangian description is used. The conservation of linear momentum and conservation of angular momentum [117] are satisfied if

$$\sum_i m_i \Delta \mathbf{P_i} = 0 \tag{3.28}$$

$$\sum_i \mathbf{r_i} \times m_i \Delta \mathbf{P_i} = 0 \tag{3.29}$$

where $\Delta \mathbf{P_i}$ denotes the position adjustment vector for chain element i; m_i is the mass of chain element i; and $\mathbf{r_i}$ is the vector from chain element i to an arbitrary common rotation centre.

As illustrated in Fig. 3.11, chain element j is adjusted from position $\mathbf{P_j}$ to $\mathbf{P_j^*}$ to maintain its position within the BSBR_{j,i^*}. However, the adjustment is only applied to the y component of $\mathbf{P_j}$ due to $y_j > y_{j,i^*\,max}$, where $x_{j,i^*\,min} < x_j < x_{j,i^*\,max}$, resulting in the failure of conserving linear and angular momentums, i.e.

$$m_i \Delta \mathbf{P_i} + m_j \Delta \mathbf{P_j} \neq 0 \tag{3.30}$$

$$\mathbf{r_i} \times m_i \Delta \mathbf{P_i} + \mathbf{r_j} \times m_j \Delta \mathbf{P_j} \neq 0$$

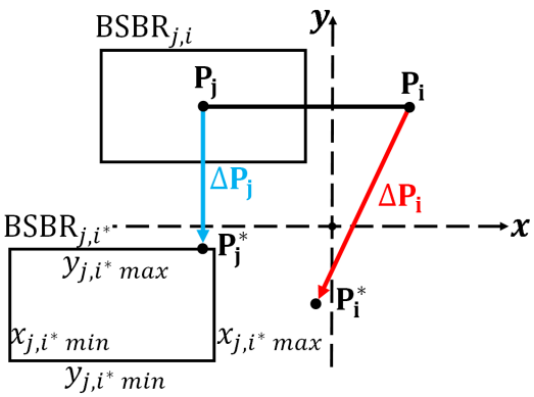

Figure 3.11 The linear and angular momentums are not conserved in the traditional ChainMails.

The failure in conserving linear and angular momentums introduces the so-called *ghost forces* which act like external forces dragging and rotating the object, resulting in unrealistic deformation [117].

3.3.1.3 Third Deficiency

Finally, the traditional ChainMail algorithms cannot achieve model dynamics in the temporal domain. The deformation process in the traditional ChainMails is achieved by a static update process, which is solely calculated from the displacement field without consideration of the effect of model dynamics in the temporal domain. It does not involve physical model dynamics to evolve the position of chain elements through numerical time integration of velocities and accelerations.

3.3.2 Proposed Ellipsoid ChainMail Bounding Region

Similar to the BSBR used in the traditional ChainMail algorithms, the proposed ellipsoid ChainMail bounding

region (ECBR) is a geometric bounding region used to control the movement of chain elements in the object. Consider two chain elements i and j connected by a chain link $\mathbf{L_{ij}}$, the bounding region is established for chain element j with respect to chain element i such that the position $\mathbf{P_j}$ of chain element j is always bounded within this region. Accordingly, the length of chain link $\mathbf{L_{ij}}$ is always bounded by the limits defined by this region.

Let point $\mathbf{C}(x_C, y_C, z_C)$ be the barycentre of the bounding region. Geometric limits $x_{j,i\ limit}$, $y_{j,i\ limit}$ and $z_{j,i\ limit}$ are used to define the dimensions of the bounding region in the axis directions. The boundary of the bounding region can be expressed by

$$x = x_C + n_x x_{j,i\ limit} \tag{3.31}$$

$$y = y_C + n_y y_{j,i\ limit}$$

$$z = z_C + n_z z_{j,i\ limit}$$

Substituting the above equation into Eq. (3.25) yields

$$\left(\frac{x - x_C}{x_{j,i\ limit}}\right)^2 + \left(\frac{y - y_C}{y_{j,i\ limit}}\right)^2 + \left(\frac{z - z_C}{z_{j,i\ limit}}\right)^2 = 1 \tag{3.32}$$

The ellipsoid represented by Eq. (3.32) defines the bounding region $\mathrm{ECBR}_{j,i}$, and it is given by

$$\left(\frac{x - x_C}{x_{j,i\ limit}}\right)^2 + \left(\frac{y - y_C}{y_{j,i\ limit}}\right)^2 + \left(\frac{z - z_C}{z_{j,i\ limit}}\right)^2 \leq 1 \tag{3.33}$$

where $\mathrm{ECBR}_{j,i}$ stands for the ellipsoid ChainMail bounding region for chain element j with respect to chain element i (see Fig. 3.12).

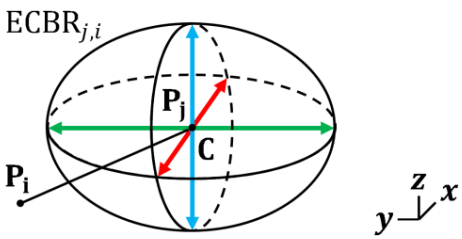

Figure 3.12 The ellipsoid ChainMail bounding region $\mathrm{ECBR}_{j,i}$ for chain element j with respect to chain element i at the rest state: point $\mathbf{C}$ is coincident with $\mathbf{P_j}$, and the three geometric limits $x_{j,i\ limit}$ (red), $y_{j,i\ limit}$ (green) and $z_{j,i\ limit}$ (blue) define the dimensions of the bounding region in the axis directions.

The three geometric limits $x_{j,i\ limit}$, $y_{j,i\ limit}$ and $z_{j,i\ limit}$ are defined by a strain limit with reference to the length of chain link $\mathbf{L_{ij}}$ at the rest state, i.e.

$$\mathbf{s_{j,i}} = l_{ij}^{0}\boldsymbol{\varepsilon}_{\mathbf{j,i}} \tag{3.34}$$

where $\mathbf{s_{j,i}} = (x_{j,i\ limit}, y_{j,i\ limit}, z_{j,i\ limit})$; l_{ij}^{0} is the length of chain link $\mathbf{L_{ij}}$ at the rest state; and $\boldsymbol{\varepsilon}_{\mathbf{j,i}} = (\varepsilon_{j,i\ x}, \varepsilon_{j,i\ y}, \varepsilon_{j,i\ z})$ is the strain limit with all components in positive values, and it defines the limits of chain link that can be extended or compressed in the axis directions.

The position of chain element j must always be bounded within the $\mathrm{ECBR}_{j,i}$. In other words, the length of chain link $\mathbf{L_{ij}}$ must always be bounded by the limits of this region. As illustrated in Fig. 3.13, let $\mathbf{P_{max}}$ and $\mathbf{P_{min}}$ be the limit points that define the maximum extension length and minimum compression length of chain link $\mathbf{L_{ij}}$. The limit points $\mathbf{P_{max}}$ and $\mathbf{P_{min}}$ can be represented by

$$\mathbf{P_{max}} = \mathbf{C} + \lambda\hat{\mathbf{u}}_{\mathbf{ij}} \tag{3.35}$$

$$\mathbf{P_{min}} = \mathbf{C} - \lambda\hat{\mathbf{u}}_{\mathbf{ij}}$$

where $\hat{\mathbf{u}}_{\mathbf{ij}}(x_{ij,u}, y_{ij,u}, z_{ij,u})$ is the unit vector of chain link $\mathbf{L_{ij}}$, and λ is the Lagrange multiplier; and they are given by

$$\hat{\mathbf{u}}_{\mathbf{ij}} = \frac{\overrightarrow{\mathbf{P_iP_j}}}{\|\overrightarrow{\mathbf{P_iP_j}}\|} \tag{3.36}$$

$$\lambda = \frac{1}{\sqrt{\left(\frac{x_{ij,u}}{x_{j,i\ limit}}\right)^2 + \left(\frac{y_{ij,u}}{y_{j,i\ limit}}\right)^2 + \left(\frac{z_{ij,u}}{z_{j,i\ limit}}\right)^2}} \tag{3.37}$$

The detailed derivation of λ is given in Appendix A.

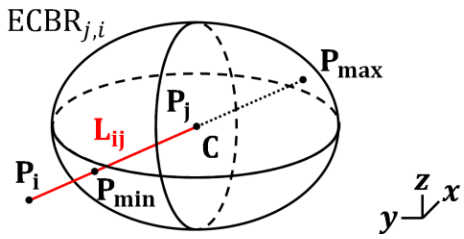

Figure 3.13 The $\mathrm{ECBR}_{j,i}$ intersects with the infinite line in the direction of chain link $\mathbf{L_{ij}}$ at points $\mathbf{P_{max}}$ and $\mathbf{P_{min}}$, which define the maximum extension and minimum compression lengths of chain link $\mathbf{L_{ij}}$.

Once the limit points $\mathbf{P_{max}}$ and $\mathbf{P_{min}}$ are determined, the maximum extension length l_{max} and minimum compression length l_{min} of chain link $\mathbf{L_{ij}}$ can be written as

$$l_{max} = \left\|\overrightarrow{\mathbf{P_i P_{max}}}\right\| \tag{3.38}$$

$$l_{min} = \left\|\overrightarrow{\mathbf{P_i P_{min}}}\right\|$$

Therefore, the length of chain link $\mathbf{L_{ij}}$ must always be bounded by the two lengths, i.e.

$$l_{min} \leq \left\|\overrightarrow{\mathbf{P_i P_j}}\right\| \leq l_{max} \tag{3.39}$$

The ECBR enables controlling the strain of a chain link independently from the chain link direction, as the dimensions of the ECBR are defined in the axis directions. In addition, anisotropic and heterogeneous materials can be modelled by setting different values of strain limit in different directions and different regions, respectively. Further, as the ECBR is established according to the condition of principle strains, it overcomes the conflict of BSBR with the concept of principle strains in continuum mechanics.

3.3.3 New Position Adjustment Rules

With the maximum extension and minimum compression lengths of a chain link, the movement of a chain element does not affect its connected neighbouring elements if the length of the chain link is within these two lengths. However, position adjustments will be applied if the chain link is extended or compressed beyond the two limits.

Consider the chain element i is moved from position $\mathbf{P_i}$ to a new position $\mathbf{P_i^*}$. To construct the new ECBR_{j,i^*}, the centre point $\mathbf{C}$ of bounding region ECBR_{j,i^*} needs to be determined. Since the ECBR_{j,i^*} is constructed for chain element j with respect to the new position of chain element i, the centre point $\mathbf{C}$ can be determined from $\mathbf{P_i^*}$ in the direction of chain link with rest length of the chain link as distance, i.e.

$$\mathbf{C} = \mathbf{P_i^*} + l_{ij}^0 \hat{\mathbf{u}}_{\mathbf{i^*j}} \tag{3.40}$$

where $\hat{\mathbf{u}}_{\mathbf{i^*j}}(x_{i^*j,u}, y_{i^*j,u}, z_{i^*j,u})$ is the unit vector of chain link $\mathbf{L_{i^*j}}$ and is given by

$$\hat{\mathbf{u}}_{\mathbf{i^*j}} = \frac{\overrightarrow{\mathbf{P_i^* P_j}}}{\left\|\overrightarrow{\mathbf{P_i^* P_j}}\right\|} \tag{3.41}$$

Fig. 3.14 illustrates the determination of centre point $\mathbf{C}$ for the extension and compression of chain link $\mathbf{L_{i^*j}}$.

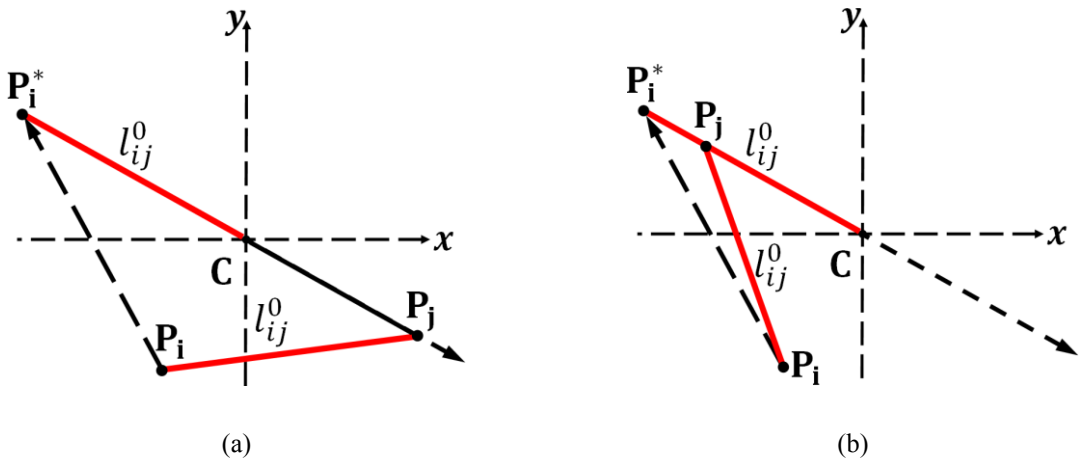

Figure 3.14 Determination of centre point **C** of ECBR_{j,i^*} when chain link $\mathbf{L_{i^*j}}$ is (a) extended or (b) compressed.

Once the centre point **C** is determined, the new ECBR_{j,i^*} can be established according to Eq. (3.33) by specifying the strain limit. Subsequently, limit points $\mathbf{P_{max}}$ and $\mathbf{P_{min}}$ can be calculated from Eq. (3.35) by identifying the intersection points between the boundary of ECBR_{j,i^*} and the infinite line of chain link $\mathbf{L_{i^*j}}$. Fig. 3.15 illustrates the determination of limit points $\mathbf{P_{max}}$ and $\mathbf{P_{min}}$ with reference to Fig. 3.14.

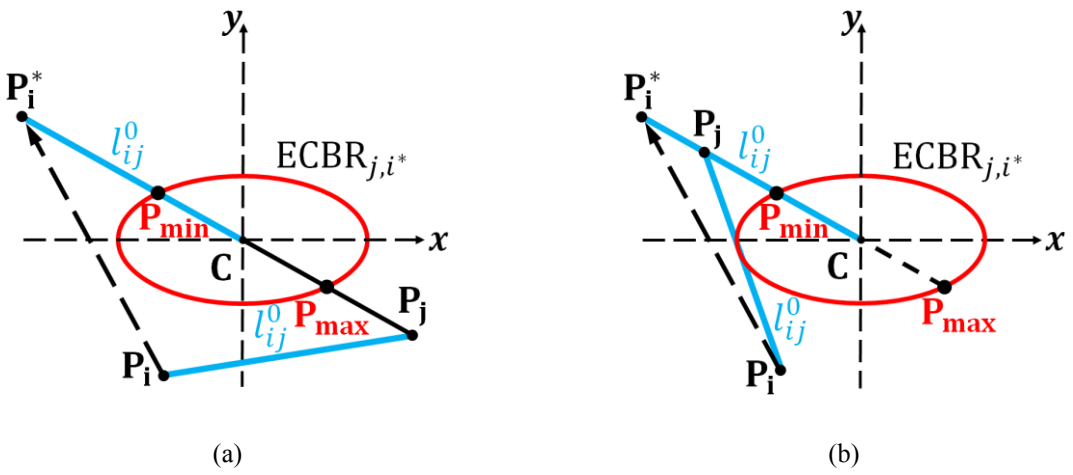

Figure 3.15 Construction of the ECBR_{j,i^*} at centre point **C**: limit points $\mathbf{P_{max}}$ and $\mathbf{P_{min}}$ are determined by identifying the intersection points between the boundary of ECBR_{j,i^*} and the infinite line of chain link $\mathbf{L_{i^*j}}$ when the chain link $\mathbf{L_{i^*j}}$ is (a) extended or (b) compressed.

With limit points $\mathbf{P_{max}}$ and $\mathbf{P_{min}}$ determined, the maximum extension length l_{max} and minimum compression length l_{min} of chain link $\mathbf{L_{i^*j}}$ can be calculated as

$$l_{max} = \left\|\overrightarrow{\mathbf{P_i^*P_{max}}}\right\| \tag{3.42}$$

$$l_{min} = \left\|\overrightarrow{\mathbf{P_i^*P_{min}}}\right\|$$

As mentioned previously, the movement of chain element i, from $\mathbf{P_i}$ to $\mathbf{P_i^*}$, does not affect chain element j if the length of chain link $\mathbf{L_{i^*j}}$ is within the two lengths. However, position adjustments will be applied if the chain link $\mathbf{L_{i^*j}}$ is extended or compressed beyond the two lengths. Unlike the traditional ChainMails where position adjustment is applied to chain element j only, the proposed ChainMail applies position adjustments to both chain elements i and j to adjust the length of chain link $\mathbf{L_{i^*j}}$ back to the maximum extension l_{max} and minimum compression l_{min}, i.e.

$$\text{(i) if } \left(\left\|\overrightarrow{\mathbf{P_i^*P_j}}\right\| > l_{max}\right), \left\|\overrightarrow{\mathbf{P_i^{**}P_j^*}}\right\| = l_{max} \tag{3.43}$$

$$\text{(ii) if } \left(\left\|\overrightarrow{\mathbf{P_i^*P_j}}\right\| < l_{min}\right), \left\|\overrightarrow{\mathbf{P_i^{**}P_j^*}}\right\| = l_{min}$$

where $\mathbf{P_i^{**}}$ and $\mathbf{P_j^*}$ are the adjusted positions of $\mathbf{P_i^*}$ and $\mathbf{P_j}$, respectively, and they are expressed by

$$\mathbf{P_i^{**}} = \mathbf{P_i^*} + \Delta\mathbf{P_{ij}} \tag{3.44}$$

$$\mathbf{P_j^*} = \mathbf{P_j} + \Delta\mathbf{P_{ji}}$$

where $\Delta\mathbf{P_{ij}}$ and $\Delta\mathbf{P_{ji}}$ are the position adjustment vectors applied to chain elements i and j, respectively. The $\Delta\mathbf{P_{ij}}$ and $\Delta\mathbf{P_{ji}}$ for case (i) in Eq. (3.43) are defined as

$$\Delta\mathbf{P_{ij}} = \lambda_{ij}\hat{\mathbf{u}}_{\mathbf{i^*j}} \tag{3.45}$$

$$\Delta\mathbf{P_{ji}} = \lambda_{ji}\hat{\mathbf{u}}_{\mathbf{i^*j}}$$

where λ_{ij} and λ_{ji} are the Lagrange multipliers calculated by

$$\lambda_{ij} = -\frac{w_i}{w_i + w_j}\left(l_{max} - \left\|\overrightarrow{\mathbf{P_i^*P_j}}\right\|\right) \tag{3.46}$$

$$\lambda_{ji} = \frac{w_j}{w_i + w_j}\left(l_{max} - \left\|\overrightarrow{\mathbf{P_i^*P_j}}\right\|\right)$$

where w_i and w_j are the inverses of their respective masses, i.e. $w_i = 1/m_i$ and $w_j = 1/m_j$, for weighting the adjustments for chain elements i and j.

The $\Delta\mathbf{P_{ij}}$ and $\Delta\mathbf{P_{ji}}$ for case (ii) in Eq. (3.43) can be calculated in a similar manner by replacing l_{max} with l_{min} in Eq. (3.46). It can be concluded from Eqs. (3.45) and (3.46) that by weighting position adjustments $\Delta\mathbf{P_{ij}}$ and $\Delta\mathbf{P_{ji}}$ with the masses of chain elements i and j and further projecting them on the infinite line of chain link $\mathbf{L_{i^*j}}$, both linear and angular momentums are conserved during the position adjustment process (see Appendix B for detailed proof).

As illustrated in Figs. 3.16(a) and (b), which correspond to Figs. 3.15(a) and (b), the length of the chain link $\mathbf{L_{i^*j}}$ exceeds the maximum extension length l_{max} in Fig. 3.16(a) and is under minimum compression length l_{min} in Fig. 3.16(b). Position adjustments $\Delta\mathbf{P_{ij}}$ and $\Delta\mathbf{P_{ji}}$ are applied to move $\mathbf{P_i^*}$ to $\mathbf{P_i^{**}}$ and $\mathbf{P_j}$ to $\mathbf{P_j^*}$, respectively. It can be seen that the new position $\mathbf{P_j^*}$ of chain element j automatically falls onto the boundary of the new $\mathrm{ECBR}_{j^*,i^{**}}$ enforced by chain element i at the new position $\mathbf{P_i^{**}}$. The length of the chain link, otherwise exceeds or under the calculated lengths, is adjusted back to the maximum extension l_{max} and minimum compression l_{min}. It should be noted that boundary conditions can be enforced by specifying displacement values to the related chain elements at the boundary of the problem domain.

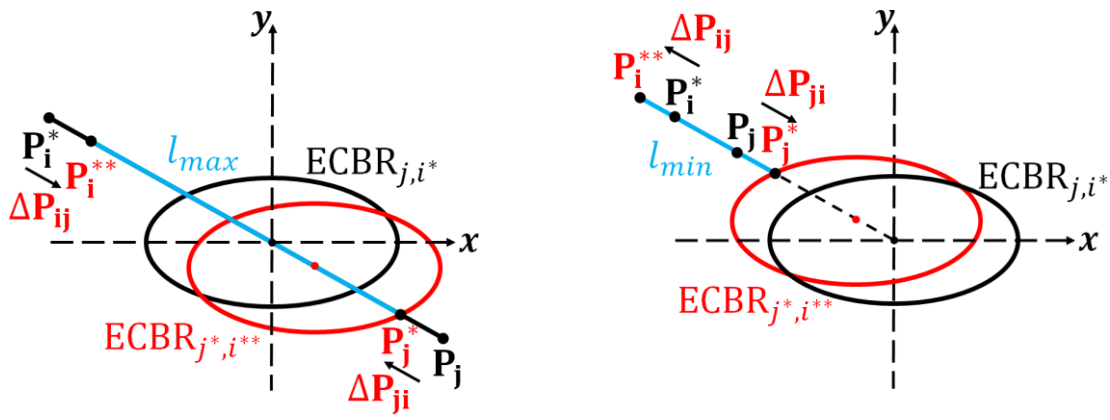

(a) (b)

Figure 3.16 Position adjustments $\Delta\mathbf{P_{ij}}$ and $\Delta\mathbf{P_{ji}}$ are applied to move chain element i from $\mathbf{P_i^*}$ to $\mathbf{P_i^{**}}$ and chain element j from $\mathbf{P_j}$ to $\mathbf{P_j^*}$, respectively, to adjusted the length of the chain link back to the (a) maximum extension l_{max} or (b) minimum compression l_{min}.

3.3.4 Model Dynamics

As mentioned previously, traditional ChainMails only use the displacement field for deformation calculation, leading to a static update process without consideration of model dynamics in the temporal domain. In the proposed method, a displacement-based formulation is established by calculating velocities and accelerations from the resultant position adjustments to enable the proposed ChainMail to handle model dynamics.

Let $\mathbf{P_i}$ and $\mathbf{P_i^*}$ be the positions of chain element i before and after position adjustment. The velocity vector $\mathbf{v_i}$ and the acceleration vector $\mathbf{a_i}$ are calculated as

$$\mathbf{v_i} = \frac{\mathbf{P_i^*} - \mathbf{P_i}}{\Delta t} \tag{3.47}$$

$$\mathbf{a_i} = \frac{\mathbf{v_i}}{\Delta t}$$

where Δt is the time step.

Further, nodal force $\mathbf{f_i}$ at chain element i of mass m_i can be calculated according to the Newton's second law of motion, i.e.

$$\mathbf{f_i} = m_i \mathbf{a_i} \tag{3.48}$$

3.3.5 Results and Discussion

Experiments are conducted to investigate the performance of the proposed method in terms of soft tissue mechanical behaviours, and isotropic and homogeneous, anisotropic, heterogeneous and large deformations. Comparison and analysis with the traditional ChainMails and deformation results from commercial FEM software package are conducted. Further, haptic feedback has been achieved with the proposed method for surgical simulation, and its performance is also evaluated and discussed.

3.3.5.1 Mechanical Behaviours

Experiments are conducted to verify the typical mechanical behaviours of soft tissues, such as the nonlinear force-displacement relationship, hysteresis and stress relaxation [112]. The nonlinear force-displacement relationship is examined using a compression test with a displacement occurred at the contact point. Three materials modelled with strain limit values of $\varepsilon = 0.1$, 0.3 and 0.5 were tested, and the feedback force was calculated when the displacement was increased at a constant rate. Fig. 3.17 illustrates the variation of force

with respect to displacement for the three materials. It can be seen that the proposed ChainMail is capable of modelling the nonlinear force-displacement relationship of soft tissues due to the use of nonlinear bounding region of ellipsoid shape and associated position adjustments.

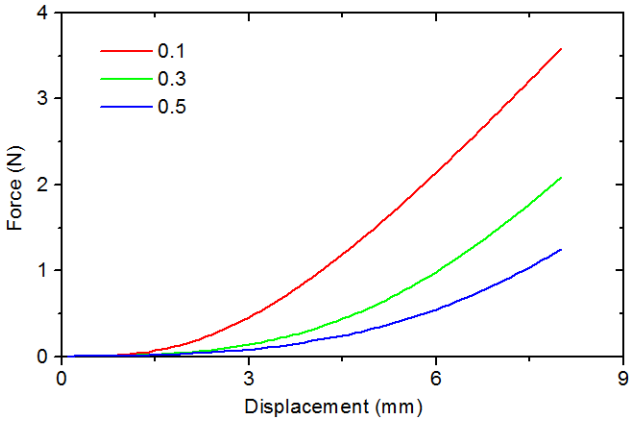

Figure 3.17 Nonlinear force-displacement relationship exhibited by the proposed ChainMail.

The hysteresis effect, in which the variation of force with respect to displacement follows two distinct paths during loading and unloading, is examined using the proposed method. A material modelled with strain limit value of $\varepsilon = 0.3$ was tested. The feedback force was calculated when the displacement was increased at a constant rate from zero to a maximum value and down to zero again. The loading process was the same as the compression process in Fig. 3.17, whereas the unloading process was calculated by restoring the displacement occurred at the contact point to the initial value at the rest state (i.e. zero). As shown in Fig. 3.18, the variation of force with respect to displacement during loading and unloading followed two distinct paths, demonstrating that the observed behaviour is in good agreement with the hysteresis effect measured in living tissues [112].

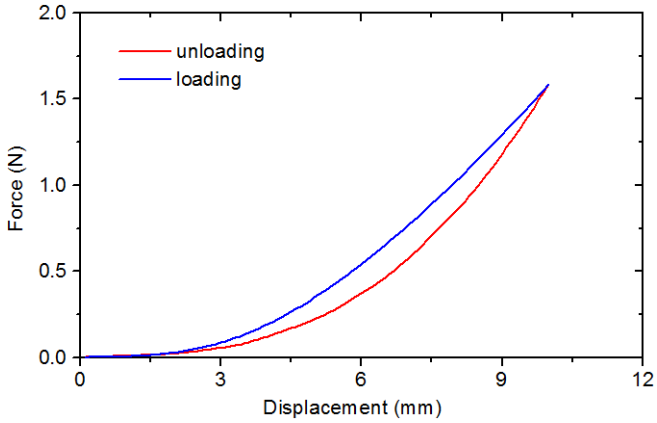

Figure 3.18 Hysteresis effect exhibited by the proposed ChainMail.

The stress relaxation is also examined by maintaining a constant displacement at the contact point and observing the variation of feedback force with respect to time. A material modelled with strain limit value of $\varepsilon = 0.3$ was tested. As shown in Fig. 3.19, the feedback force decreased asymptotically towards a minimum value. This is similar to the tissue relaxation response observed from living tissues [112].

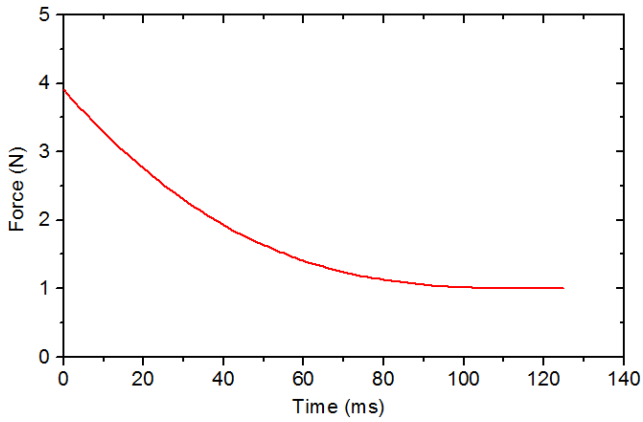

Figure 3.19 Stress relaxation exhibited by the proposed ChainMail.

3.3.5.2 Isotropic and Homogeneous, Anisotropic and Heterogeneous Deformations

Soft tissues are highly complex in terms of material compositions; therefore, the capability to handle different materials is essential for producing realistic soft tissue deformation. The deformations of three isotropic and homogeneous materials under tension and compression are illustrated in Fig. 3.20. The three materials are

modelled by a volumetric cubic model containing 1,331 chain elements with strain limit values of $\varepsilon = 0.1$, 0.3 and 0.5.

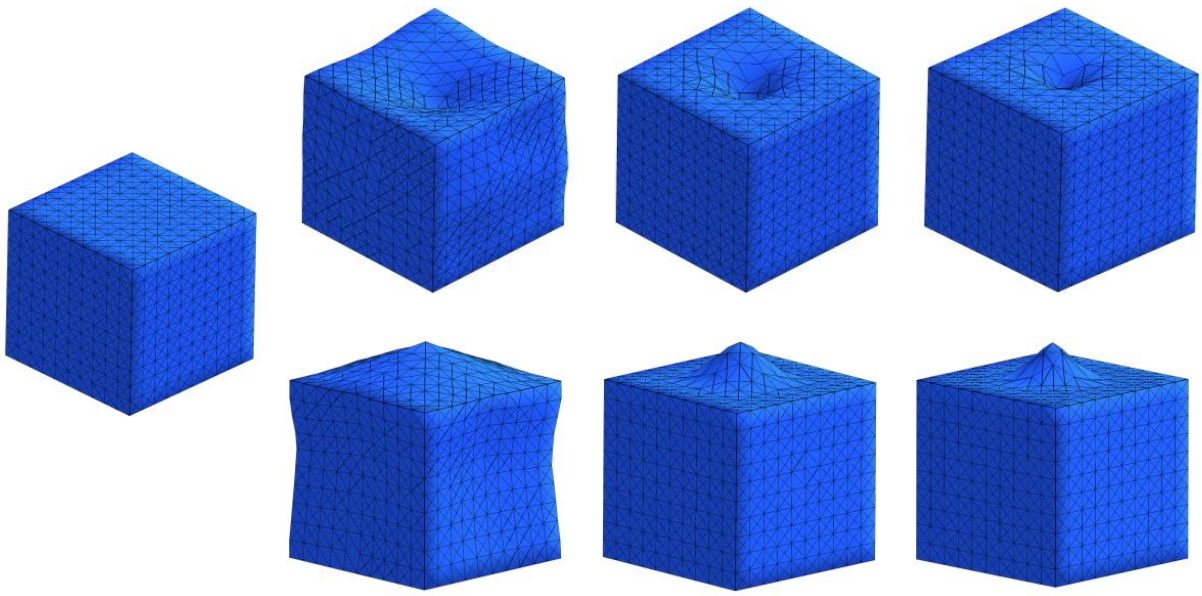

(a) (b) (c) (d)

Figure 3.20 Volumetric deformations of three isotropic and homogeneous materials using a common strain limit to all chain elements: (a) the rest state; the strain limit value is (b) 0.1, (c) 0.3 and (d) 0.5; the top row illustrates compressive deformations, whereas the bottom row illustrates tensile deformations.

The deformation of an anisotropic material has been achieved with the same volumetric cubic model by setting different values of strain limit in different directions, whereas the deformation of a heterogeneous material has been achieved by setting different values of strain limit to chain elements at different regions. A comparison of deformations of isotropic and homogeneous, anisotropic and heterogeneous materials is illustrated in Fig. 3.21.

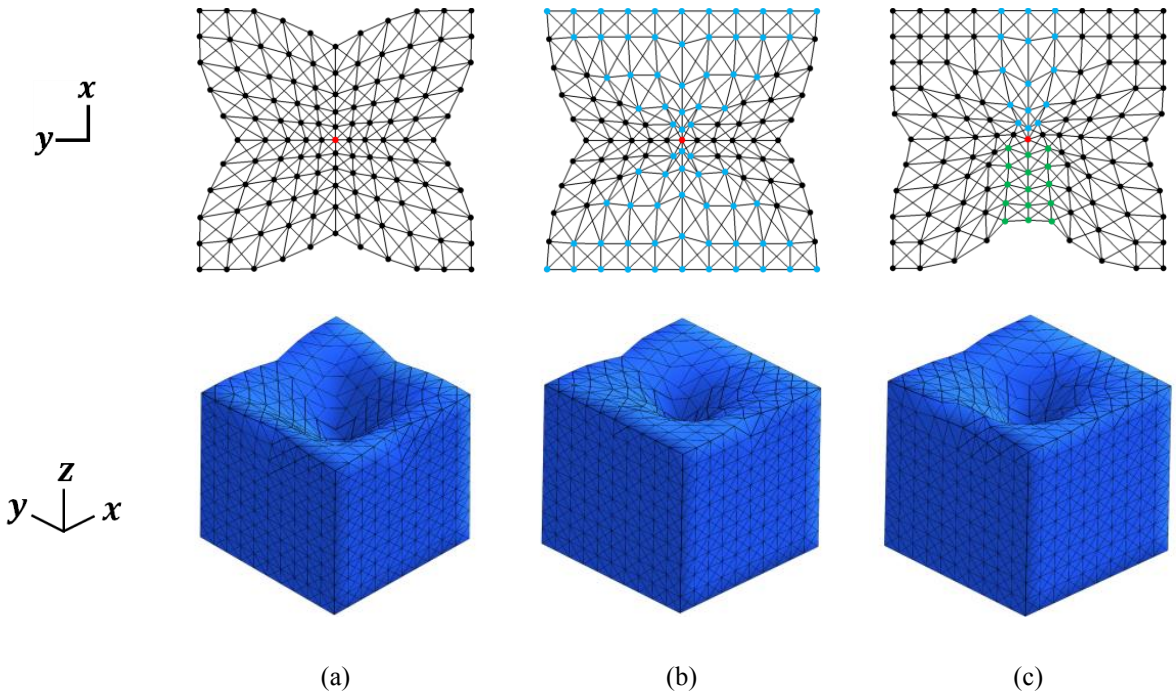

Figure 3.21 Volumetric deformations of (a) isotropic and homogeneous, (b) anisotropic and (c) heterogeneous materials: strain limit value is (a) 0.2 for all chain elements; (b) 0.2 for the black chain elements in the horizontal direction and 0.4 for the blue chain elements in the vertical direction; and (c) 0.1, 0.2 and 0.4 for the green, black and blue chain elements, respectively; and 0.2 for the red contact chain element in (a), (b) and (c).

Compared to the isotropic and homogeneous deformation shown in Fig. 3.21(a), the anisotropic deformation shown in Fig. 3.21(b) demonstrates that the model is deformed more significantly in the horizontal direction around the deformation area, whereas the heterogeneous deformation shown in Fig. 3.21(c) demonstrates that the model is deformed differently at different regions due to different strain limit values.

3.3.5.3 Comparison of Deformation and Computational Time with Traditional ChainMails

Trials are conducted to compare the proposed ChainMail with the traditional ChainMails under the same conditions. The effect of conserving linear and angular momentums is presented in Fig. 3.22 using shear deformations modelled by the proposed method and traditional ChainMails. It can be seen that the traditional ChainMail algorithms produced unrealistic deformation behaviours due to not conserving linear and angular momentums.

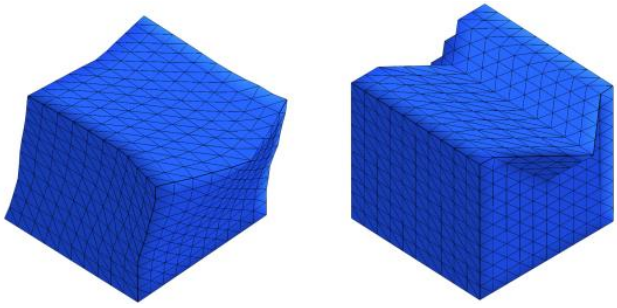

(a) (b)

Figure 3.22 Comparison of deformations between the (a) proposed ChainMail and (b) traditional ChainMails in terms of the conservation of linear and angular momentums; the strain limit is set to $\varepsilon = 0.1$ for both methods.

Further, it can also be seen from Fig. 3.22 that the deformed shape produced by the proposed method behaves nonlinearly, whereas the traditional ChainMails behave only linearly. The nonlinear deformation is attributed to the use of nonlinear bounding region of ellipsoid shape and associated position adjustments. Additional comparisons are presented in Fig. 3.23. The proposed ChainMail exhibits significantly more volumetric behaviours than that of the traditional ChainMails. With the proposed method, Fig. 3.23(a) shows that the side faces of the cubic model shrank inwards due to the tensile deformation on the top face, and Fig. 3.23(c) shows that the bottom side of the cylinder model followed the movement of the tensile deformation on the top side. With above deformation examples, all of the deformations exceed 10% of the original mesh size. This demonstrates that the proposed method can accommodate large deformation of soft tissues.

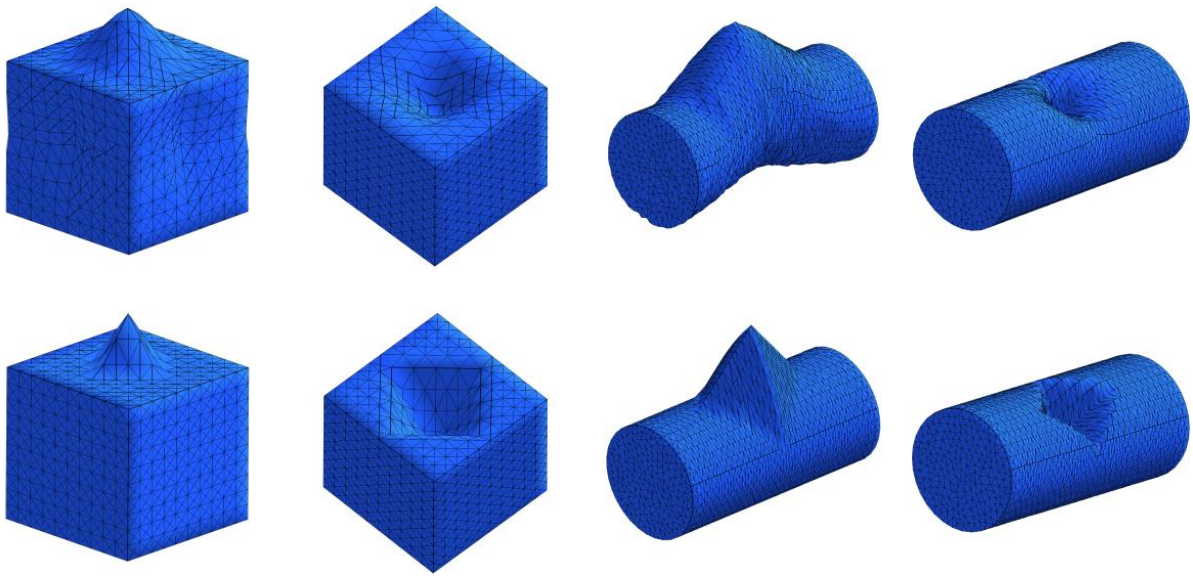

(a) (b) (c) (d)

Figure 3.23 Comparison of deformations between the proposed ChainMail method (top row) and the traditional ChainMails (bottom row): (a) cube extension; (b) cube compression; (c) cylinder extension; and (d) cylinder compression.

Trials are also conducted to compare the computational time of the proposed method with the traditional ChainMails under same conditions. The computational time was evaluated on an Intel(R) Core(TM) i5-2500k CPU@4.30 GHz and 8 GB RAM PC without efforts on optimising codes or hardware acceleration. Fig. 3.24 shows the computational time of both methods. The proposed ChainMail consumed more time than the traditional ChainMails due to the additional computation of the nonlinear bounding regions and the associated position adjustments. Real-time performance of 30 Hz was achieved with around 46,900 moved chain elements by the proposed method. The computational performance can be further improved by ChainMail GPU implementation [29].

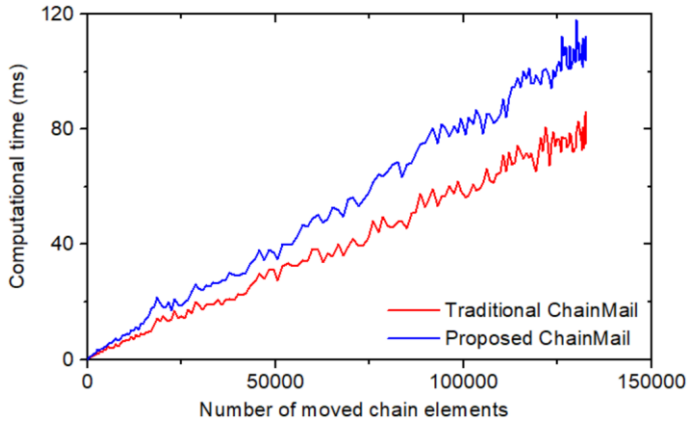

Figure 3.24 Comparison of computational time between the proposed ChainMail and traditional ChainMail algorithms.

It can also be seen from Fig. 3.24 that the computational time of the proposed method is only related to the number of moved chain elements rather than the model size, and it increased nearly linearly with the increase of the number of moved chain elements. This behaviour is attributed to the position adjustment rules, since position adjustments will only be applied if the chain link is extended or compressed beyond the calculated lengths.

3.3.5.4 Comparison of Deformation with FEM from Commercial Analysis Package

Experiments have been conducted to compare the deformation of the proposed ChainMail with those from commercial FEM analysis package. The FEM deformation is conducted by CATIA V5R21 with settings illustrated in Fig. 3.25(a). The volumetric cube is of size 20mm x 20mm x 20mm with its bottom surface constrained, and external compressive force is applied to the yellow contact area on the top surface in the normal direction. Isotropic and homogeneous soft tissue materials (Poisson's ratio $\nu = 0.47$ [112], Young's modulus $E = 3{,}500$ Pa [118] and mass density $\rho = 1{,}060$ kg/m^3 [119]) were employed for the FEM simulation. The strain limit is set to $\varepsilon = 0.1$ for all chain elements in the proposed ChainMail. It can be seen from Figs. 3.25(b) and (c) that the deformation produced by the proposed method is in good agreement with those from the commercial FEM software package. The mean absolute displacement error is around 0.105 mm (9.7%).

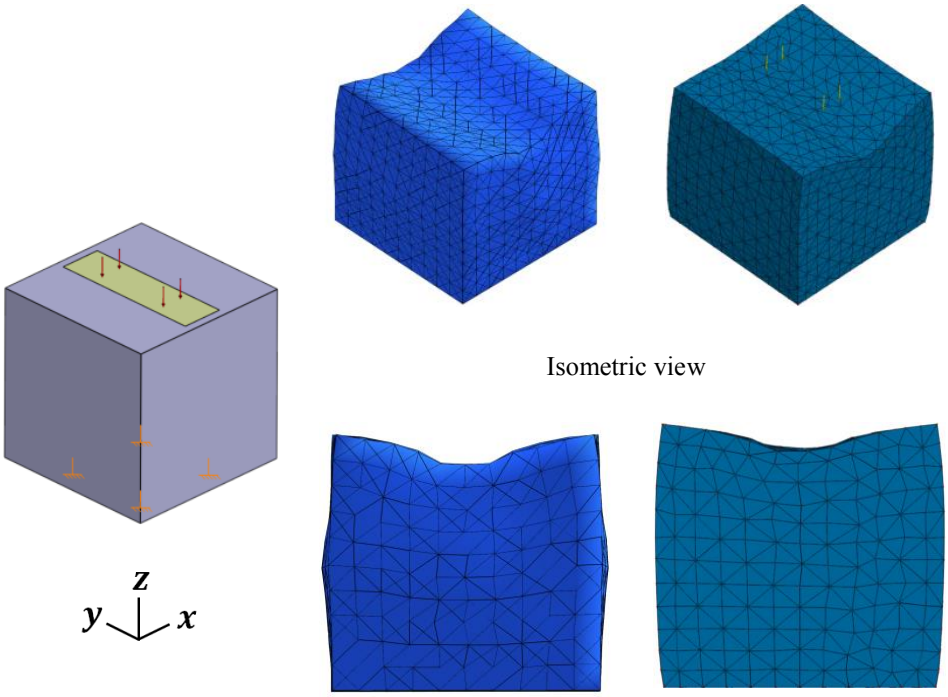

(a) (b) (c)

Figure 3.25 Comparison of deformations between the proposed ChainMail and FEM from commercial software: (a) FEM settings; (b) proposed ChainMail algorithm; and (c) FEM reference solution.

3.3.5.5 Soft Tissue Deformation with Haptic Feedback

A PHANToM haptic device from Geomagic has been integrated with the proposed ChainMail for interactive soft tissue deformation with haptic feedback. Fig. 3.26 shows an interactive deformation of a virtual volumetric human liver with haptic feedback. Deformation and feedback forces were calculated using the proposed method, with the calculated deformation rendered graphically on the monitor for visual feedback, and the calculated forces output to the PHANToM device for haptic feedback.

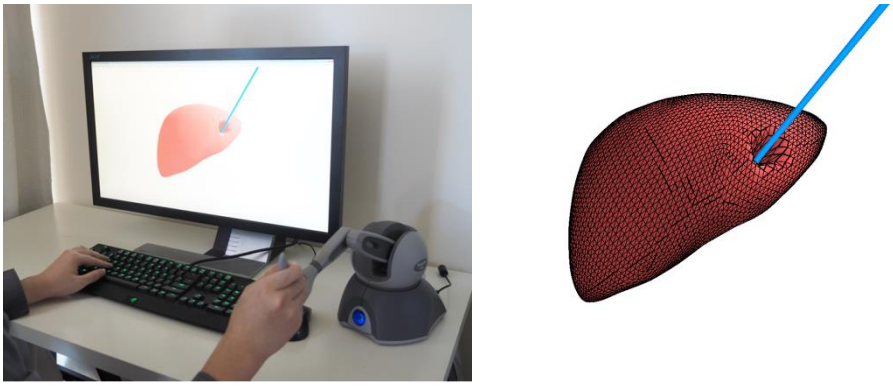

Figure 3.26 Interactive deformation of a virtual human liver model with haptic feedback via the virtual probe.

Fig. 3.27 illustrates deformations of the virtual human liver from different viewing angles.

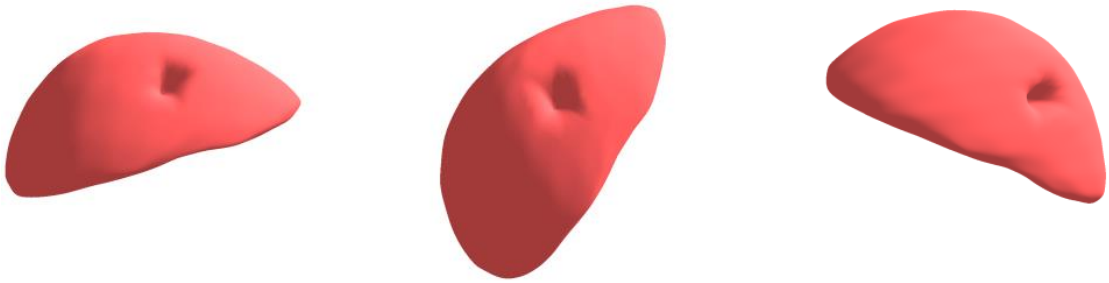

Figure 3.27 Deformations of the volumetric human liver model from different viewing angles.

As illustrated in Fig. 3.28, the haptic update rate decreased with the increase of the number of moved chain elements. The haptic update rate of at least 1,000 Hz for real-time force feedback is achieved with around 4,100 moved chain elements. When the computational speed cannot meet the haptic refresh update requirement, force extrapolation [120] was employed to improve the realism of force feedback by generating missing forces from the previous calculation loop.

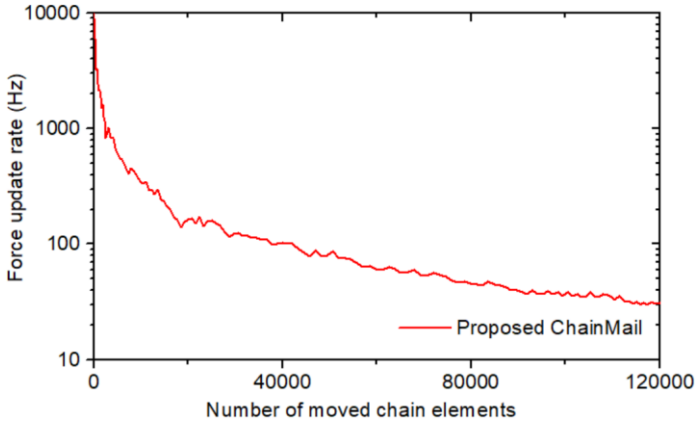

Figure 3.28 Haptic performance of the proposed ChainMail, the haptic update rate of at least 1,000 Hz for real-time force feedback is achieved with around 4,100 moved chain elements.

3.4 Neural Dynamics-based ChainMail Algorithm

As mentioned previously, surgical simulation requires not only realistic soft tissue deformation but also real-time computational performance. Given the fast computational advantage of neural networks, which would be able to achieve the real-time computational performance required by surgical simulation, a neural dynamics-based ChainMail algorithm is proposed. The proposed neural dynamics-based ChainMail formulates the problem of elastic deformation into cellular neural network activities to avoid the complex computation of elasticity. It combines the ChainMail position adjustment mechanism with nonlinear cellular neural dynamics for soft tissues' nonlinear deformation and the typical mechanical behaviours. It endows the principle of continuum mechanics to the neural network for soft tissue simulation by formulating the local connectivity of cells in the cellular neural network as the local position adjustments of ChainMail, through which the dynamic behaviours of soft tissue deformation are transformed into the neural dynamics of cellular neural network. The proposed method not only can model nonlinear soft tissue deformation via the nonlinear characteristics of neural dynamics but also enables the cellular neural network to follow the principle of continuum mechanics to simulate soft tissue deformation.

3.4.1 Neural Dynamics

The proposed method employs the cellular neural network (CNN) [121], which is a local-interconnected array-computing structure. The neuron in the CNN is called cell, which is a nonlinear dynamic processing unit consisting of capacitors, resistors and current sources of linear and nonlinear types. Cells are locally connected

and interact only with their nearest neighbours [122]; cells that are not directly connected affect each other indirectly via the global propagation effect of CNN [123].

The CNN can be applied to any type of geometric grid of any dimension. Consider a geometric grid shown in Fig. 3.29, points i and j at positions $\mathbf{P_i}$ and $\mathbf{P_j}$ are occupied by cells $C(i)$ and $C(j)$, respectively.

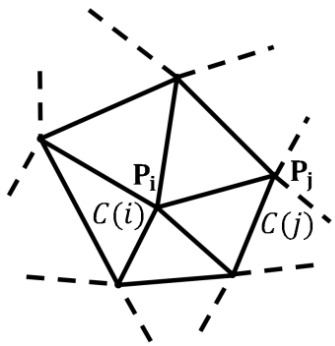

Figure 3.29 A CNN on an irregular grid: the spatial positions of $\mathbf{P_i}$ and $\mathbf{P_j}$ are occupied by cells $C(i)$ and $C(j)$, respectively.

To describe the interaction range between cells, the neighbourhood $N_r(i)$ of cell $C(i)$ is firstly defined by

$$N_r(i) = \{C(j) | edge(C(i), C(j)) \leq r\} \tag{3.49}$$

where r is a positive integer number denoting the number of edges between cells $C(i)$ and $C(j)$.

The dynamic behaviours of cell $C(i)$ are governed by the following equations

$$C\frac{dv_{xi}(t)}{dt} = -\frac{1}{R_x}v_{xi}(t) + \sum_{C(j)\in N_r(i)} A(i;j)v_{yj}(t) + \sum_{C(j)\in N_r(i)} B(i;j)v_{uj} + I_i \tag{3.50}$$

$$v_{yi}(t) = \frac{1}{2}(|v_{xi}(t) + K| - |v_{xi}(t) - K|), K \geq 1;\ |v_{xi}(0)| \leq K;\ |v_{ui}| \leq K \tag{3.51}$$

where C is the cell capacitance, which can be set to 1 for simplicity; R_x is the cell resistance; I_i is the current source; r is 1 in our case; $A(i;j)$ is the feedback template which defines the interactions between neighbouring cells, whereas $B(i;j)$ is the control template which characterises the influence of input on the cell; $v_{ui}(t)$, $v_{xi}(t)$ and $v_{yi}(t)$ are the cell input, state and output at time t; $v_{yi}(t)$ is a nonlinear sigmoid function of $v_{xi}(t)$, and it is bounded by a constant K.

Without cell input v_{ui}, Eq. (3.50) is reduced to an autonomous CNN [124] whose governing equation is given by

$$\frac{dv_{xi}(t)}{dt} = -\frac{1}{R_x}v_{xi}(t) + \sum_{C(j)\in N_r(i)} A(i;j)v_{yj}(t) + I_i \tag{3.52}$$

3.4.2 ChainMail Formulation of Local Connectivity of Cells

The CNN and ChainMail share common characteristics. Under the given initial conditions and external inputs, the dynamic behaviours of the proposed CNN are described by the local connectivity of cells. Similarly, the behaviours of ChainMail are also described by the local position adjustments under the same conditions. Further, similar to the CNN output, which is bounded by the constant K, the movement of a chain element is bounded by the maximum extension and minimum compression lengths. The position of a chain element will be adjusted locally only if the two lengths are violated, to keep the chain link between the two chain elements within the geometric bounding region. Therefore, in the proposed method, the local connectivity of cells in the CNN is formulated according to the local position adjustments of ChainMail. As mentioned previously, from the perspective of continuum mechanics of elasticity, the ChainMail can be viewed as a spring system in which a spring's length is bounded by its minimum compression and maximum extension lengths. Accordingly, the formulation of CNN's local connectivity as the ChainMail local position adjustments enables the CNN dynamics to follow the principle of continuum mechanics for soft tissue deformation.

For the sake of conciseness, the minimum compression l_{ij}^{min} and the maximum extension l_{ij}^{max} of the ChainMail algorithm are calculated by

$$l_{ij}^{min} = (1-\alpha)l_{ij}^{0} \tag{3.53}$$

$$l_{ij}^{max} = (1+\alpha)l_{ij}^{0}$$

where α is the material parameter whose value is set according to the spring stiffness k; and l_{ij}^{0} is the initial length of the chain link connecting chain elements i and j. The minimum compression l_{ij}^{min} and maximum extension l_{ij}^{max} of the ellipsoid bounding region-based ChainMail can be easily incorporated into the proposed neural dynamics model by substituting Eq.(3.53) by Eq. (3.42).

Thus, the current length l_{ij} between the current positions of chain elements i and j is bounded by

$$l_{ij}^{min} \leq l_{ij} \leq l_{ij}^{max} \tag{3.54}$$

Define the position adjustments for chain elements i and j to be $\Delta\mathbf{P_i}$ and $\Delta\mathbf{P_j}$. As illustrated in Fig. 3.30, position adjustments are applied to both chain elements to adjust the current length l_{ij} back to l_{ij}^{min} or l_{ij}^{max} if the current length is less than the minimum compression length or larger than the maximum extension length. The adjustments of l_{ij}^{max} are expressed by Eq. (3.55). The adjustments of l_{ij}^{min} can be expressed similarly by substituting l_{ij}^{max} with l_{ij}^{min}.

$$\Delta\mathbf{P_i} = \frac{1}{2}\left(\|\mathbf{P_j} - \mathbf{P_i}\| - l_{ij}^{max}\right)\frac{\mathbf{P_j} - \mathbf{P_i}}{\|\mathbf{P_j} - \mathbf{P_i}\|} \tag{3.55}$$

$$\Delta\mathbf{P_j} = -\frac{1}{2}\left(\|\mathbf{P_j} - \mathbf{P_i}\| - l_{ij}^{max}\right)\frac{\mathbf{P_j} - \mathbf{P_i}}{\|\mathbf{P_j} - \mathbf{P_i}\|}$$

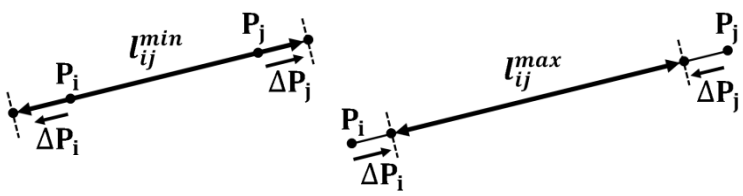

(a) (b)

Figure 3.30 Position adjustments $\Delta\mathbf{P_i}$ and $\Delta\mathbf{P_j}$ are applied to chain element positions $\mathbf{P_i}$ and $\mathbf{P_j}$ to adjust the current length between the two chain elements back to the (a) minimum compression length l_{ij}^{min} and (b) maximum extension length l_{ij}^{max}.

For the purpose of conciseness, consider a simple case where a chain element is connected with four neighbours as illustrated in Fig. 3.31.

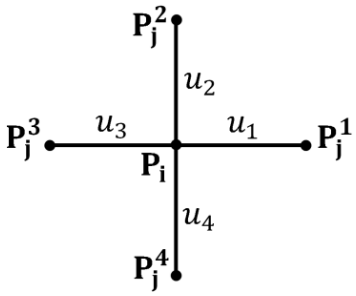

Figure 3.31 A grid with four local connections: chain element i at position $\mathbf{P_i}$ is connected with four neighbouring chain elements at positions $\mathbf{P_j^1}$, $\mathbf{P_j^2}$, $\mathbf{P_j^3}$ and $\mathbf{P_j^4}$ with distances in-between denoted by u_1, u_2, u_3 and u_4, respectively.

The net adjustment for chain element i can be expressed by the sum of the adjustments applied to position $\mathbf{P_i}$

$$\sum \Delta\mathbf{P_i} = \mu_1\mathbf{P_j^1} + \mu_2\mathbf{P_j^2} + \mu_3\mathbf{P_j^3} + \mu_4\mathbf{P_j^4} - (\mu_1 + \mu_2 + \mu_3 + \mu_4)\mathbf{P_i} \tag{3.56}$$

where

$$\mu_n = \frac{1}{2}\left(\frac{\left(u_n - l_{ij}^{n,max}\right)}{u_n}\delta_n^{max} + \frac{\left(u_n - l_{ij}^{n,min}\right)}{u_n}\delta_n^{min}\right); n = 1, 2, 3, 4 \tag{3.57}$$

where

$$u_n = \left\|\mathbf{P_j^n} - \mathbf{P_i}\right\| \tag{3.58}$$

$$\delta_n^{max} = \begin{cases} 1; \text{ if } \left(u_n > l_{ij}^{n,max}\right) \\ 0; \text{ if } \left(u_n \leq l_{ij}^{n,max}\right) \end{cases}$$

$$\delta_n^{min} = \begin{cases} 1; \text{ if } \left(u_n < l_{ij}^{n,min}\right) \\ 0; \text{ if } \left(u_n \geq l_{ij}^{n,min}\right) \end{cases}$$

By associating cell state $v_{xi}(t)$ with chain element position $\mathbf{P_i}$, the feedback template A of the proposed CNN can be expressed as

$$A = \begin{pmatrix} 0 & \mu_2 & 0 \\ \mu_3 & \frac{1}{R_x} - (\mu_1 + \mu_2 + \mu_3 + \mu_4) & \mu_1 \\ 0 & \mu_4 & 0 \end{pmatrix} \tag{3.59}$$

In case that chain element i is connected to any number of neighbouring chain elements, the net adjustment for chain element i can be expressed by the sum of the adjustments applied to position $\mathbf{P_i}$, i.e.

$$\sum \Delta \mathbf{P_i} = \sum_{\mathbf{P_j} \in N(\mathbf{P_i})} \mu_{ij}\, \mathbf{P_j} - \sum_{\mathbf{P_j} \in N(\mathbf{P_i})} \mu_{ij}\, \mathbf{P_i} \tag{3.60}$$

where $N(\mathbf{P_i})$ is the set of neighbouring chain elements of chain element i, and μ_{ij} is given by

$$\mu_{ij} = \frac{1}{2}\left(\frac{\left(u_{ij} - l_{ij}^{max}\right)}{u_{ij}} \delta_{ij}^{max} + \frac{\left(u_{ij} - l_{ij}^{min}\right)}{u_{ij}} \delta_{ij}^{min} \right) \tag{3.61}$$

where

$$u_{ij} = \left\| \mathbf{P_j} - \mathbf{P_i} \right\| \tag{3.62}$$

$$\delta_{ij}^{max} = \begin{cases} 1; \text{ if } \left(u_{ij} > l_{ij}^{max}\right) \\ 0; \text{ if } \left(u_{ij} \leq l_{ij}^{max}\right) \end{cases}$$

$$\delta_{ij}^{min} = \begin{cases} 1; \text{ if } \left(u_{ij} < l_{ij}^{min}\right) \\ 0; \text{ if } \left(u_{ij} \geq l_{ij}^{min}\right) \end{cases}$$

Similar to Eq. (3.59), the feedback template A can be written as

$$A(i;j) = \mu_{ij} \tag{3.63}$$

$$A(i;i) = \frac{1}{R_x} - \sum_{C(j) \in N_r(i)} \mu_{ij}$$

3.4.3 Current Source, Initial and Boundary Conditions

When soft tissues are deformed, there is a displacement experienced at the region of contact. Hence, the current source I_i is set to the input displacement at the contact point i, whereas its value is set to zero at other points. The initial condition for the CNN is the position of chain elements at the rest state. The boundary condition in the proposed method is the Dirichlet boundary condition which enforces fixed position to the related chain

elements of the problem domain at all times, and it is achieved by employing fixed-state cells.

3.4.4 Results

Trials are conducted with the proposed method to evaluate its performance in terms of soft tissues' nonlinear deformation and the typical mechanical behaviours.

3.4.4.1 Nonlinear Deformation

Fig. 3.32 compares the deformations of a rectangular plane (21 x 21 nodes) between the proposed CNN and traditional ChainMails. It can be seen that the deformation produced by the proposed CNN in Fig. 3.32(a) behaves nonlinearly while the traditional ChainMails in Fig.3.32(b) shows a linear deformation of pyramid shape.

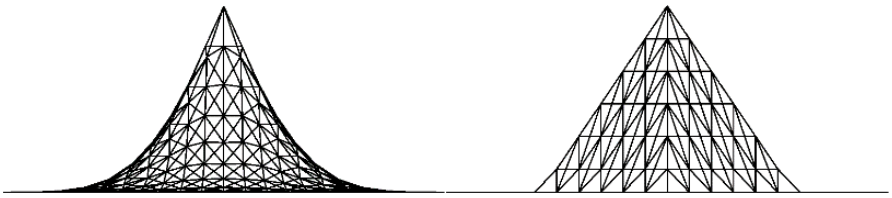

(a) (b)

Figure 3.32 Deformations of a plane by (a) the proposed CNN and (b) traditional ChainMails: the deformation produced by the proposed CNN shows nonlinear behaviours, whereas it shows only linear behaviours with the traditional ChainMails.

3.4.4.2 Mechanical Behaviours

Trials are also conducted to verify the proposed CNN against the soft tissues' typical mechanical behaviours, such as the nonlinear force-displacement relationship, hysteresis and stress relaxation [112]. Nonlinear force-displacement relationship is examined using a compression test with a displacement occurred at the contact point. Fig. 3.33(a) demonstrates the nonlinear force-displacement relationship (α = 0.1, 0.5 and 0.9). Hysteresis is examined using the same compression test for loading, while the unloading is achieved by resorting the chain links between chain elements to their initial lengths (α = 0.5). It can be seen from Fig. 3.33(b) that the variation of force with respect to displacement follows two distinct paths during loading and unloading, this behaviour is

similar to the hysteresis effect measured from living biological tissues [112]. Stress relaxation is also examined by maintaining a constant displacement at the contact point (α = 0.5). As shown in Fig. 3.33(c), the internal force decreases asymptotically towards a minimum value. This behaviour is in agreement with the stress relaxation observed from real soft tissues [112].

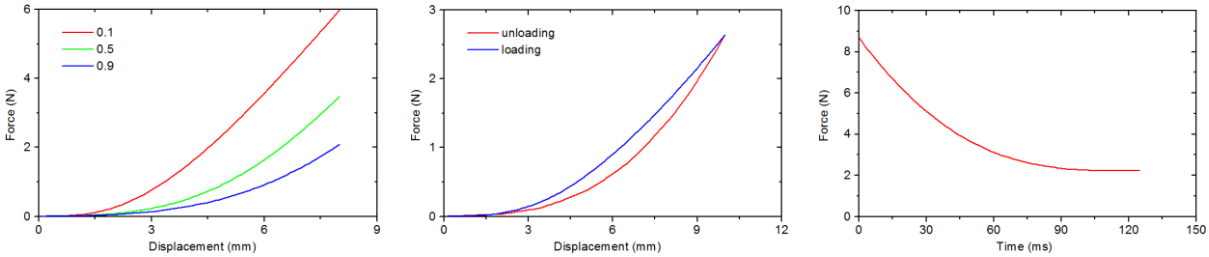

(a) (b) (c)

Figure 3.33 (a) Nonlinear force-displacement, (b) hysteresis and (c) stress relaxation observed from the proposed method.

3.4.4.3 Soft Tissue Deformation

The proposed CNN has been integrated into a prototype surgical simulation for interactive deformation of virtual human organs with haptic feedback. Fig. 3.34 illustrates the prototype surgical simulation system with a comparison of deformations modelled by the proposed CNN and traditional ChainMails. The volumetric human liver model contains 5,762 mass points and 20,255 tetrahedrons, and it is deformed via a virtual haptic probe. It can be seen that the proposed CNN generates a better deformation shape than the traditional ChainMails.

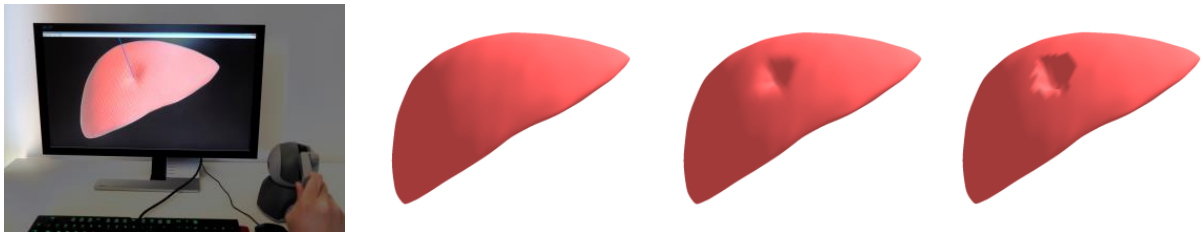

(a) (b) (c) (d)

Figure 3.34 Interactive deformation of the human liver model: (a) the interactive simulation system; (b) the initial state of the volumetric liver model; (c) the deformation by the proposed CNN; (d) the deformation by the traditional ChainMails.

4. Energy Propagation Method

In this chapter, a novel neural dynamics-based energy propagation method is proposed for realistic, real-time and stable soft tissue deformation. The realistic, real-time and stable soft tissue deformation is addressed in Chapters 4.1, 4.2 and 4.3, respectively. The novelties of the proposed method are presented as follows:

- **Proposed Energy Propagation Method (Chapter 4.1):** The proposed method can (i) accommodate various soft tissue material properties; and (ii) achieve nonlinear soft tissue deformation.
- **Neural Dynamics-based Energy Propagation Method (Chapter 4.2):** The proposed method can achieve real-time computational performance for surgical simulation.
- **Neural Dynamics-based Stable Simulation of Soft Tissue Deformation (Chapter 4.3):** The proposed method can achieve stable simulation for soft tissue deformation.

4.1 Proposed Energy Propagation Method

In this chapter, an energy propagation method based on the Poisson propagation of potential energy is presented for modelling of nonlinear soft tissue deformation for surgical simulation. The proposed method considers external forces as physical input, compared to the input displacement in ChainMail algorithms. It carries out soft tissue deformation from the viewpoint of potential energy propagation, in which the mechanical load of an external force applied to soft tissues is considered as the equivalent potential energy, according to the law of conservation of energy, and is further propagated in the volume of soft tissues based on the principle of Poisson energy propagation. The proposed method combines Poisson propagation of mechanical load and non-rigid mechanics of motion to govern the dynamics of soft tissue deformation. A finite volume scheme is developed for discretisation of Poisson equation on 3D volume mesh. Results demonstrate that the proposed method is not only able to handle isotropic and homogeneous, anisotropic and heterogeneous materials, but also able to accommodate nonlinear deformation of soft tissues.

4.1.1 Theory of Energy Propagation

Biologically, soft tissues are complex in terms of material compositions, structural formations, and biomechanical behaviours. In continuum mechanics of solid, a soft tissue model can be considered as a continuum medium [55]. When a soft tissue previously at rest state is subject to an external force, the tissue is deformed. According to the non-rigid mechanics of motion, the dynamics of soft tissue deformation is governed by the Lagrange's form of continuum mechanics, i.e.

$$m\frac{\partial^2 \mathbf{P}}{\partial t^2} + \gamma\frac{\partial \mathbf{P}}{\partial t} + \frac{\delta W(\mathbf{P})}{\delta \mathbf{P}} = \mathbf{f}(\mathbf{P}, t) \tag{4.1}$$

where $\mathbf{P}$ is the position vector of a point with mass density m and damping coefficient γ; $\mathbf{f}(\mathbf{P}, t)$ is the external force applied to the point at time t; and $W(\mathbf{P})$ is the net instantaneous potential energy at the point to cause the soft tissue deform away from its rest state.

It can be seen from Eq. (4.1) that soft tissue deformation is the consequence of the distribution of mechanical load of an external force applied to the tissue. When a soft tissue model is deformed under an external force, there is a displacement occurred. The mechanical load of an external force is propagated and distributed among masses of the soft tissue in the form of strain energy according to tissue's material properties, leading to an energy distribution to deform the soft tissue away from its rest state [125]. Under a given external force, the energy distribution is determined by soft tissue material properties and boundary conditions. Therefore, the deformation of soft tissues is actually a process of energy propagation [126].

Poisson equation provides a natural manner for describing energy propagation. The spatiotemporal-continuous Poisson equation with a continuous energy source in a continuum medium is described by a nonlinear second-order partial differential equation (PDE)

$$\frac{\partial \varphi}{\partial t} + Q = \nabla \cdot (\rho \nabla \varphi) \tag{4.2}$$

where φ is the scalar potential function at the considered point at time t; Q is the source function which describes the potential density; $\nabla \cdot$ is the divergence operator; ρ is the constitutive coefficient of the point; and ∇ is the gradient operator.

The Poisson equation has been extensively used to study various problems in mechanics of elastic solid, such as the displacement field of elastic solids under torsion loading [127]. In the Poisson equation, the constitutive coefficient is equivalent to the modulus constant of an elastic material, which describes the physical behaviours of the material. The source to generate energy in the field is similar to the mechanical load applied to the soft tissue. The strain energy stored and distributed in the soft tissue to cause deformation is similar to the optimal Poisson distribution of potential energy. Therefore, the energy propagation occurred in the process of soft tissue deformation can be considered as a Poisson energy propagation process with an energy source at the contact point, through which the mechanical load is treated as the equivalent potential energy and further propagated among masses of the soft tissue based on the Poisson equation, leading to an optimal energy distribution for soft tissue deformation.

Since the mechanical load is applied to the soft tissue in the direction of applied force, the energy source in the Poisson equation should be directional. Accordingly, Eq. (4.2) is further written into a vector form

$$\frac{\partial \boldsymbol{\varphi}}{\partial t} + \mathbf{Q} = \nabla \cdot (\boldsymbol{\rho} \nabla \boldsymbol{\varphi}) \tag{4.3}$$

where $\boldsymbol{\varphi}$ is the vector form of potential function, whose magnitude is the potential energy of the point at time t; $\mathbf{Q}$ is the vector form of energy source; and $\boldsymbol{\rho}$ is the matrix of constitutive coefficients.

As mentioned previously, when a soft tissue model is deformed by an external force, the mechanical load is applied in the direction of the external force and is further stored in the soft tissue in the form of strain energy. Therefore, the energy source in the Poisson equation can be formulated as the strain energy density in the direction of the applied force, i.e.

$$\mathbf{Q} = \int \boldsymbol{\sigma} \; d\boldsymbol{\varepsilon} \; \frac{\mathbf{F}}{\|\mathbf{F}\|} \tag{4.4}$$

where $\boldsymbol{\sigma}$ and $\boldsymbol{\varepsilon}$ are the stress and strain at the point; and $\mathbf{F}$ is the external force with magnitude of $\|\mathbf{F}\|$. Since the mechanical load only occurs at the point where an external force is applied, the obtained energy source $\mathbf{Q}$ is set at the contact point only, whereas its value is set to zero at other points. By substituting Eq. (4.4) into Eq. (4.3), it can be seen that soft tissue deformation is described as the Poisson energy propagation, leading to an energy distribution for soft tissue deformation governed by Eq. (4.1).

Since the rest state of the soft tissue is stress-free, the initial condition is the zero potential at all mass points of the solution domain. The boundary condition for solving Eq. (4.3) is realised by the Dirichlet boundary condition, in which a specified potential function is enforced to the related points on the problem domain boundary at all times.

4.1.2 Numerical Discretisation

The proposed Poisson equation is continuous in both space and time. In order to analyse the potential energy field developed from energy propagation, both spatial and temporal domains need to be discretised. The spatial continuous Poisson equation is approximated using an edge-based median-dual finite volume method [128]. The spatial domain is discretised into a number of non-overlapping control volumes, over which the conservation of energy is enforced in a discrete sense. As illustrated in Fig. 4.1, the control volume is formed by employing a median-dual mesh connecting edge-midpoints, face-centroids, and centroid of a geometric enclosure around a mass point. The geometric enclosure can be of any geometric shapes such as triangles or quadrilaterals in 2D and tetrahedrons, hexahedrons, prisms or pyramids in 3D. Numerical integration is performed by looping all of the edges in the discretised spatial domain where potential functions are calculated with respect to each mass point.

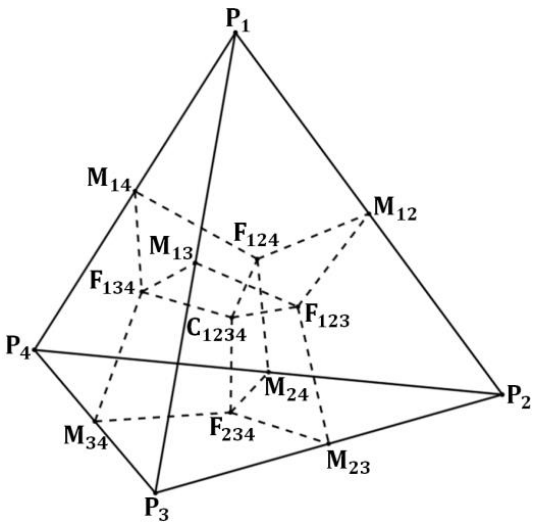

Figure 4.1 Median-dual control volumes: the tetrahedron $\mathbf{P_1P_2P_3P_4}$ is divided into four hexahedrons of equal volumes by connecting edge-midpoints $\mathbf{M_{ij}}$, face-centroids $\mathbf{F_{ijk}}$ and centroid of tetrahedron $\mathbf{C_{ijkl}}$. A portion of the median-dual control volume of point $\mathbf{P_1}$ is represented by the hexahedron $\mathbf{P_1M_{12}F_{123}M_{13}F_{134}M_{14}F_{124}C_{1234}}$. The control volume Ω_1 of point $\mathbf{P_1}$ is the union of all such hexahedrons that share the point.

For the purpose of conciseness, a scalar form of the proposed Poisson equation is considered for discretisation. The discretisation of the vector form can be achieved by discretising each scalar component. Recall the Poisson equation and write in an integral form for point $\mathbf{P_i}$ enclosed by its control volume Ω_i yields

$$\int_{\Omega_i} \left(\frac{\partial \varphi_i}{\partial t} + Q_i\right) d\Omega = \int_{\Omega_i} \nabla \cdot (\rho_i \nabla \varphi_i)\, d\Omega \tag{4.5}$$

Applying Gauss's divergence theorem to above equation yields

$$\int_{\Omega_i} \left(\frac{\partial \varphi_i}{\partial t} + Q_i\right) d\Omega = \int_{S_i} (\rho_i \nabla \varphi_i) \cdot \mathbf{n}\, dS \tag{4.6}$$

where $\mathbf{n}$ is the outward unit normal vector to the infinitesimal surface element dS on the boundary surface S_i of control volume Ω_i.

Rewriting Eq. (4.6) in a discrete form for point $\mathbf{P_i}$ yields

$$\frac{\partial \varphi_i}{\partial t} + Q_i = \frac{1}{\Omega_i} \sum_{\mathbf{P_j} \in N(\mathbf{P_i})} (\rho_i \nabla \varphi_i) \cdot \mathbf{S_{ij}} \tag{4.7}$$

where $N(\mathbf{P_i})$ is the set of neighbouring points of $\mathbf{P_i}$, and $\mathbf{S_{ij}}$ is the surface area projection in the direction of the unit normal vector $\mathbf{n_{ij}}$ of S_{ij} which is a common surface shared by control volumes Ω_i and Ω_j.

Considering point $\mathbf{P_i}$ and its neighbouring point $\mathbf{P_j}$ with four quadrilateral boundary surfaces S_1, S_2, S_3 and S_4 illustrated in Fig. 4.2, the $\mathbf{S_{ij}}$ can be calculated by

$$\mathbf{S_{ij}} = \mathbf{n_1} S_1 + \mathbf{n_2} S_2 + \mathbf{n_3} S_3 + \mathbf{n_4} S_4 \tag{4.8}$$

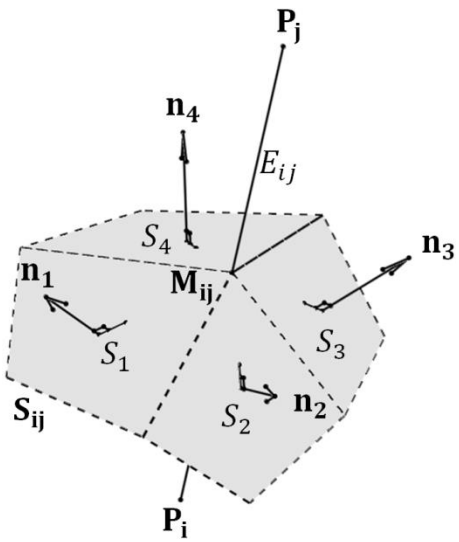

Figure 4.2 Boundary surface $\mathbf{S_{ij}}$, comprising surfaces S_1, S_2, S_3 and S_4 with unit normal vectors $\mathbf{n}_1$, $\mathbf{n}_2$, $\mathbf{n}_3$ and $\mathbf{n}_4$, respectively, attached to the edge E_{ij} connecting points $\mathbf{P_i}$ and $\mathbf{P_j}$ with its mid-point denoted by $\mathbf{M_{ij}}$.

The boundary surface S_i of the control volume Ω_i enclosing point $\mathbf{P_i}$ is the union of all such boundary surfaces attached to the edge E_{ij} that connects point $\mathbf{P_i}$ and its neighbouring point $\mathbf{P_j}$. Therefore, the numerical integration can be performed by looping all of the edges in the discretised spatial domain.

The $\rho_i \nabla \varphi_i$ in Eq. (4.7) is the flux on the boundary surface, and it can be approximated by considering linear interpolation of the constitutive coefficients and potential functions along the edge and evaluated at the edge mid-point [129]. Hence, $\rho_i \nabla \varphi_i$ may be represented by $\rho_i \nabla \varphi_i|_{\mathbf{M_{ij}}}$ at the edge mid-point $\mathbf{M_{ij}}$, i.e.

$$\rho_i \nabla \varphi_i|_{\mathbf{M_{ij}}} = \frac{\rho_i \nabla \varphi_i + \rho_j \nabla \varphi_j}{2} \tag{4.9}$$

where ρ_i and ρ_j are the constitutive coefficients, and φ_i and φ_j are the potential functions at respective points.

Isotropic and homogeneous materials can be achieved by employing a common constitutive coefficient ρ throughout the entire volumetric soft tissue model, whereas anisotropic and heterogeneous materials can be achieved by setting different values of constitutive coefficients to mass points at different directions and different regions, respectively.

To calculate $\nabla \varphi_i$ and $\nabla \varphi_j$ in Eq. (4.9), Gauss's divergence theorem is once again employed

$$\int_{\Omega_i} \nabla \varphi_i \, d\Omega = \int_{S_i} \varphi_i \cdot \mathbf{n} \, dS \tag{4.10}$$

Similar to Eqs. (4.7) and (4.9), simplifying Eq. (4.10) yields

$$\nabla \varphi_i = \frac{1}{\Omega_i} \sum_{\mathbf{P_j} \in N(\mathbf{P_i})} \frac{\varphi_i + \varphi_j}{2} \mathbf{S_{ij}} \tag{4.11}$$

The calculation of $\nabla \varphi_j$ in Eq. (4.9) can be performed in a similar manner. The control volume Ω_i at point $\mathbf{P_i}$ can be calculated by taking the sum of volumes over all hexahedrons that share the point. Due to the use of median-dual mesh, the volume V_{dual} of a hexahedron is simply one fourth of the volume V_{tet} of a tetrahedron in the tetrahedral mesh. The V_{dual} of other geometric enclosures such as hexahedron, prism and pyramid are $\frac{1}{8}V_{hex}$, $\frac{1}{6}V_{prism}$ and $\frac{3}{16}V_{pyramid}$, respectively [130].

The temporal derivative $\partial \varphi_i / \partial t$ at point $\mathbf{P_i}$ in Eq. (4.7) is approximated by a first-order explicit forward time stepping scheme, i.e.

$$\frac{\partial \varphi_i}{\partial t} \cong \frac{\varphi_i(t + \Delta t) - \varphi_i(t)}{\Delta t} \tag{4.12}$$

where Δt is the time step, and $\varphi_i(t)$ and $\varphi_i(t + \Delta t)$ are the potential functions of point $\mathbf{P_i}$ at time t and $t + \Delta t$, respectively.

4.1.3 Results

Trials are conducted with the proposed method to evaluate its performance in terms of (1) isotropic and

homogeneous, anisotropic and heterogeneous deformations; (2) nonlinear force-displacement relationship; (3) soft tissue deformation; and (4) computational performance.

4.1.3.1 Isotropic and Homogeneous, Anisotropic and Heterogeneous Deformations

Isotropic and homogeneous, anisotropic and heterogeneous deformations can be achieved with the proposed method by using the property of constitutive coefficient. Fig. 4.3 illustrates the deformation of an isotropic and homogeneous material at 20 iterations. The volumetric cylinder model in Fig. 4.3(a) contains 441 mass points (mass density $m = 1.0$, damping constant $\gamma = 2.0$ and constitutive coefficient $\rho = 0.05$) and 1,469 tetrahedrons, and it is deformed by a compressive force applied to the surface of the cylinder in the normal direction. It can be seen that the cylinder is deformed evenly for an isotropic and homogeneous material in Fig. 4.3(b).

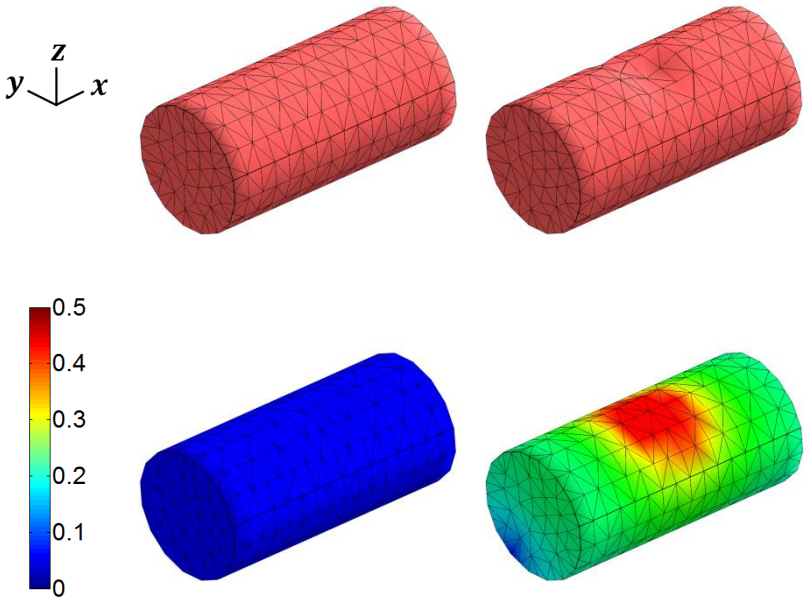

(a) (b)

Figure 4.3 Deformation and potential energy distribution (coloured) of an isotropic and homogeneous material: (a) the rest state of the cylinder and (b) the deformed state of the cylinder under a compressive force.

Fig. 4.4 illustrates the deformations of an anisotropic and a heterogeneous material along with the deformation

comparison with the homogeneous material at the same iteration. The anisotropic material has the same material parameters as the homogeneous material except that the constitutive coefficient values are different in different directions (constitutive coefficient $\rho = 0.08$ in the direction of x axis). Compared to the isotropic and homogeneous deformation in Fig. 4.4(a), the anisotropic material in Fig. 4.4(b) is deformed more significantly in the direction of x axis around the deformation area. The heterogeneous material in Fig. 4.4(c) with different constitutive coefficient values at different regions is deformed differently according to the constitutive coefficient values (constitutive coefficient $\rho = 0.08$ in the direction of x axis at the right portion of the cylinder, whereas the constitutive coefficient $\rho = 0.05$ at the left portion of the cylinder).

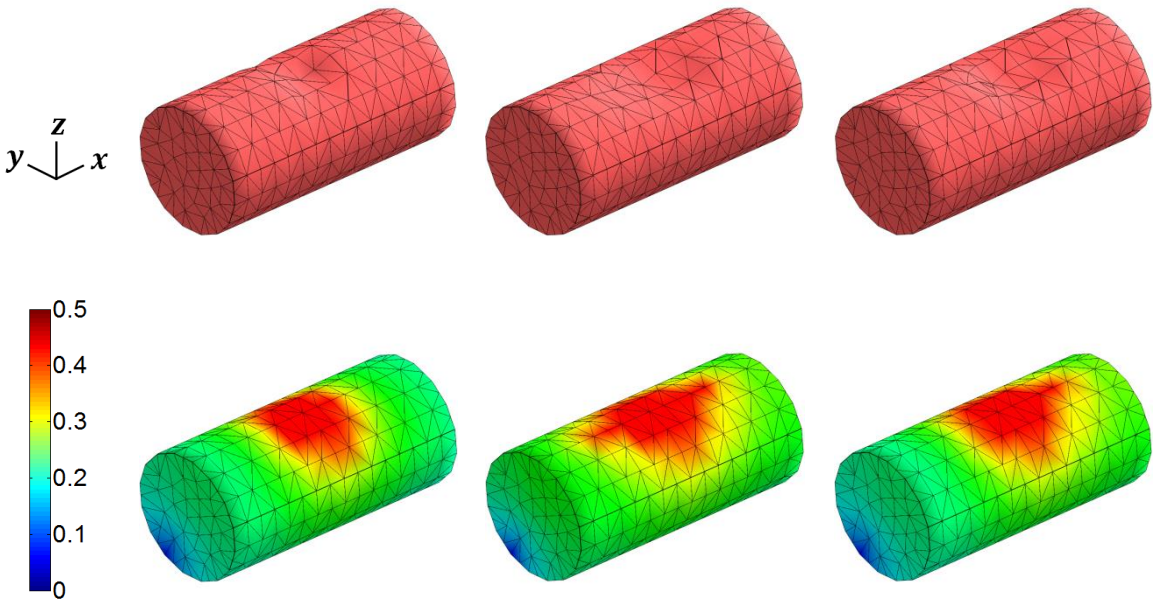

(a) (b) (c)

Figure 4.4 Comparison of deformation and potential energy distribution (coloured) of an isotropic and homogeneous, an anisotropic and a heterogeneous material: (a) the homogeneous material is deformed evenly around the deformation area; (b) the anisotropic material is deformed more significantly in the direction of x axis around the deformation area; and (c) the heterogeneous material is deformed differently according to the constitutive coefficient values.

4.1.3.2 Nonlinear Force-Displacement Relationship

Trials are conducted to verify the nonlinear force-displacement relationship of the proposed method. Three

materials with three different damping coefficients ($\gamma = 1.0$, 4.0 and 6.0) were examined using a compression test. Results in Fig. 4.5 show that the displacement varied nonlinearly with the applied force. The nonlinear force-displacement relationship further reveals that the proposed method is capable of accommodating nonlinear deformation of soft tissues.

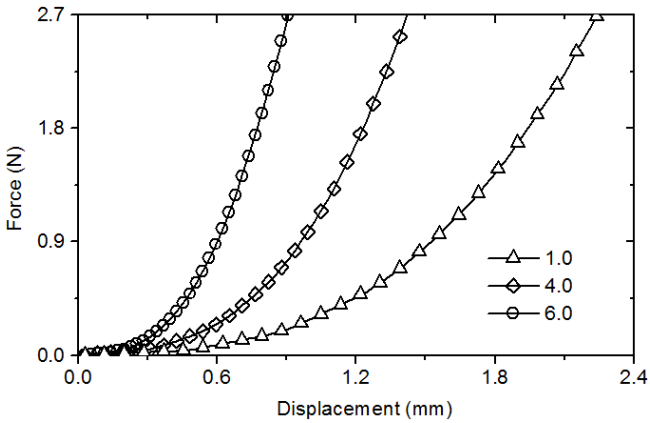

Figure 4.5 Nonlinear force-displacement relationship observed from the proposed method.

4.1.3.3 Soft Tissue Deformation

Trials are also conducted on a virtual human kidney model and a lung model to demonstrate soft tissue deformation for surgical simulation. The kidney model consists of 1,378 mass points and 4,691 tetrahedrons, and the human lung model consists of 1,706 mass points and 5,414 tetrahedrons. Figs. 4.6 and 4.7 illustrate the kidney and lung deformations and their associated distributions of potential energy by the proposed method at 25 iterations, respectively.

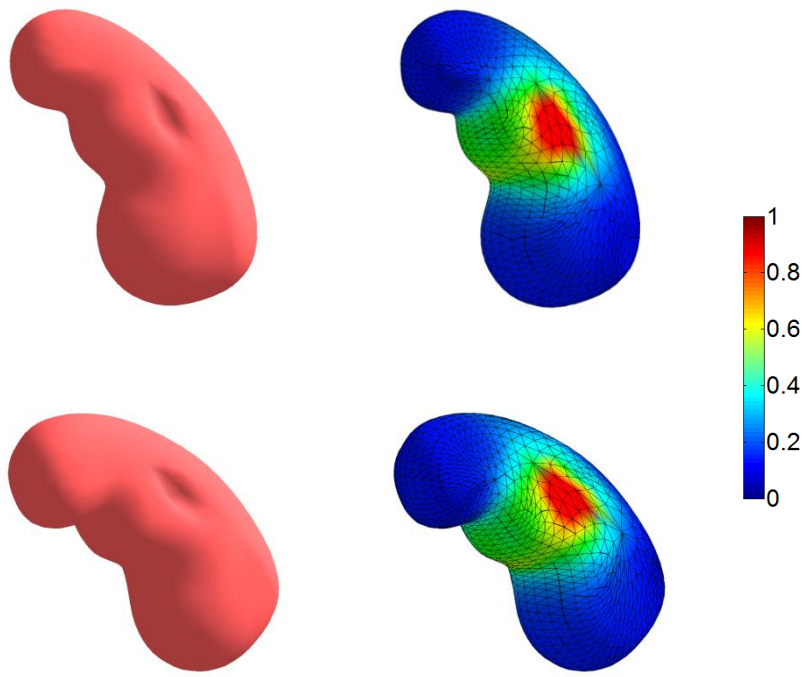

(a) (b)

Figure 4.6 Deformation and potential energy distribution (coloured) of a human kidney model from different views: (a) the deformed states of the kidney, and (b) the distribution of potential energy of the kidney under a compressive force.

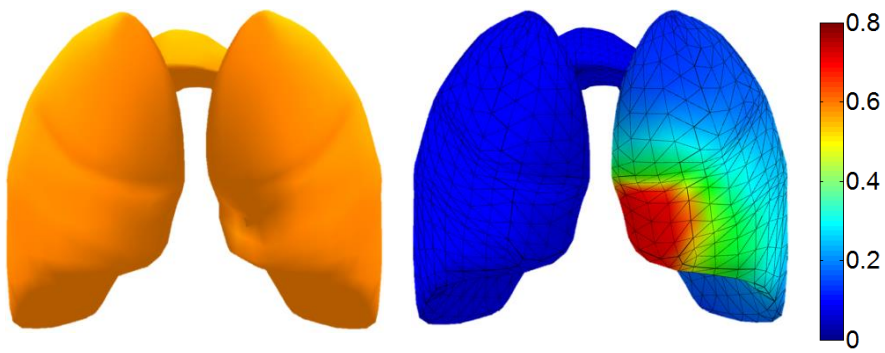

(a) (b)

Figure 4.7 Deformation and potential energy distribution (coloured) of a human lung model: (a) the deformed state of the lung, and (b) the distribution of potential energy of the lung under a compressive force.

4.1.3.4 Computational Performance

Trials are conducted to evaluate the computational performance of the proposed method in terms of visual and haptic feedbacks on an Intel(R) Core(TM) i7-4770 CPU@3.40 GHz and 8 GB RAM memory PC. It can be seen from Fig. 4.8(a) that the computational time for visual feedback is increased with the increase of mesh points. The visually satisfactory refresh rate of 30 Hz (33 ms) to maintain a realistic visual feedback is achieved with around 1,200 mesh points. However, under the same conditions, the computational time of linear FEM [55] is 1.04 s, demonstrating that the proposed method has a better computational performance than linear FEM.

The PHANToM haptic device requires forces to be updated at the rate of at least 1,000 Hz for realistic force feedback. As it can be seen from Fig. 4.8(b), the force update rate above 1,000 Hz is achieved with around 350 mesh points. When the computational speed cannot meet the haptic refresh update requirement, force extrapolation [120] was employed to improve the realism of haptic feedback by generating missing forces from previous calculation loop.

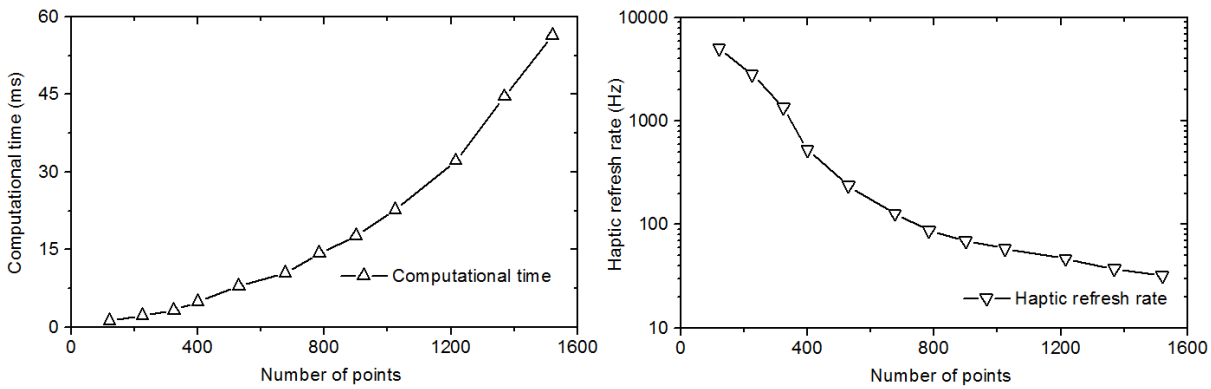

(a) (b)

Figure 4.8 Computational performance of the proposed method: (a) visual feedback; and (b) haptic feedback.

4.1.4 Remarks

In the proposed method, the nonlinear soft tissue deformation is formulated as a process of energy propagation, in which the mechanical load is propagated and distributed in the soft tissue in the form of strain energy to deform the soft tissue away from its rest state. To analyse the propagation and distribution of mechanical load, the proposed method formulates the propagation of mechanical load from the viewpoint of Poisson energy propagation. By formulating the energy source as the strain energy density, based on the law of conservation of

energy, the soft tissue deformation is described as a Poisson propagation of mechanical load that is applied to the soft tissue to cause deformation.

The proposed method is connected with the classical continuum mechanics in the sense that it considers a soft tissue model as a continuum medium, whose deformation is due to the distribution of strain energy as described by the non-rigid mechanics of motion of continuum mechanics. Further, the proposed method is based on the balance of mechanical energy for soft tissue deformation. The soft tissue deformation is due to the strain energy, which is further due to the external mechanical load. Therefore, the energy source is formulated as the strain energy density in the direction of the applied force at the contact point.

Compared to other deformation methods based on linear elasticity to describe soft tissue deformation, the proposed method can achieve nonlinear force-displacement relationships, and hence handle nonlinear deformation of soft tissues. Different from the method based on geometric nonlinearity [131] for nonlinear deformation, the proposed method achieves nonlinear deformation with the nonlinear force-displacement relationship. Unlike the method based on material nonlinearity [56] for soft tissue deformation, the proposed method does not require pre-computation and can handle not only isotropic and homogeneous but also anisotropic and heterogeneous materials by simply changing the constitutive coefficient value of mass points.

4.2 Neural Dynamics-based Energy Propagation Method

To simulate soft tissue deformation, the deformation behaviours of soft tissues and their dynamics need to be solved at all times. Given the computational advantage of cellular neural network afforded by the collective and simultaneous computing nature of neural cells, which would be suitable for the real-time computational requirement of surgical simulation, the cellular neural network is employed in the proposed method for real-time simulation of soft tissue deformation.

4.2.1 Cellular Neural Network

Solving Eqs. (4.1) and (4.3) using traditional solving algorithms is a time-consuming task. The discretisation of spatial-continuous Eqs. (4.1) and (4.3) leads to a sparse system of equations that is usually solved by traditional solving algorithms such as the Gaussian elimination or Gauss-Seidel iteration. However, traditional solving algorithms involve an iterative solution process, leading to an expensive computational cost, especially in the case of volumetric objects with a large number of mass points.

Compared to traditional solving algorithms, CNN offers an incomparable computational advantage owing to the collective and simultaneous computing nature of cells. As mentioned in Chapter 3.4, CNN is a locally interconnected analogue array-computing structure made of cells. Each cell is a time-continuous nonlinear dynamic processing unit consisting of capacitors, resistors and current sources of linear and nonlinear types [132]. Cells are locally connected and exchange information only with their neighbours [122], while cells that are not directly connected affect each other indirectly via the global propagation effect of CNN [123]. The computational advantage, nonlinear cell dynamics, spatial local interactions and global propagation behaviours, make CNN a natural choice for solving Eqs. (4.1) and (4.3) for real-time nonlinear deformable modelling. It has been evident in literature that the CNN solutions represent excellent approximations to many nonlinear PDEs [133] and dynamic systems [134]. Further, CNN solutions are continuous in time and continuous and bounded in value [135]. The transient state can also be physically modelled through the time-continuous nature of CNN, whereas it is only modelled through numerical time integrations in MSM and FEM.

Recall the dynamics of a cell described by the following equations and conditions [121]:

Cell state

$$C_x \frac{dv_{xi}(t)}{dt} = -\frac{1}{R_x} v_{xi}(t) + \sum_{C(j)\in N_r(i)} A(i;j) v_{yj}(t) + \sum_{C(j)\in N_r(i)} B(i;j) v_{uj}(t) + I_i \tag{4.13}$$

Cell output

$$v_{yi}(t) = f\big(v_{xi}(t)\big) = \frac{1}{2}\left(|v_{xi}(t) + K| - |v_{xi}(t) - K|\right), \qquad K \geq 1 \tag{4.14}$$

Conditions

$$|v_{xi}(0)| \leq K;\ |v_{ui}| \leq K \tag{4.15}$$

where $i = 1, 2, \dots, n$, and $n \geq 2$ is the number of cells in the network; for the ith cell $C(i)$, $v_{ui}(t)$, $v_{xi}(t)$ and $v_{yi}(t)$ denote the input, state and output of the cell at time t; C_x, R_x and I_i are the capacitance of cell capacitor, resistance of cell resistor and current of cell current source; $A(i;j)$ is the feedback template that defines the interactions of cell $C(i)$ with neighbouring cell $C(j)$, and $B(i;j)$ is the control template that characterises the influence of input of neighbouring cells on the cell state; K is the saturation voltage of the voltage-controlled source [136]; and $N_r(i)$ is the set of connected neighbouring cells of cell $C(i)$ within a radius r, which is defined as

$$N_r(i) = \{C(j) | edge(C(i), C(j)) \leq r\} \tag{4.16}$$

where r is a positive integer number defining the local interaction range of cell $C(i)$. For the sake of simplicity without loss of generality, the case of the smallest neighbourhood, i.e. $r = 1$ is considered.

4.2.1.1 CNN Formulation of Energy Propagation

The space-continuous Poisson equation is discretised in a similar way in Chapter 4.1.2 by subdividing the spatial domain of a soft tissue model into a number of non-overlapping control volumes with computational points located at centres, over which the conservation of energy is enforced in a discrete sense. The control volume is formed by employing a dual mesh connecting edge-midpoints, face-centroids, and centroid of a geometric enclosure around a computational point. The geometric enclosure can be of any shape such as triangles or quadrilaterals in 2D and tetrahedrons, hexahedrons, prisms or pyramids in 3D. The control volume Ω_i of a point i at position $\mathbf{P_i}$ in a tetrahedral and hexahedral mesh is illustrated in Fig. 4.9.

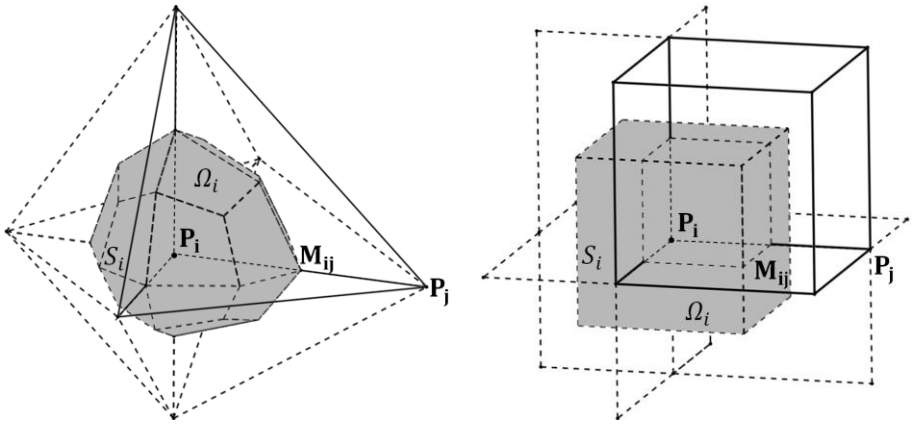

(a) (b)

Figure 4.9 The control volume Ω_i of point i at position $\mathbf{P_i}$ is shown in grey in a (a) tetrahedral mesh and (b) hexahedral mesh, with its enveloping boundary surface denoted by S_i; the neighbouring point of point i is denoted by j at position $\mathbf{P_j}$ and the midpoint of the edge between points i and j is denoted by $\mathbf{M_{ij}}$.

For the purpose of conciseness, a scalar form of the Poisson equation is considered for discretisation, while the discretisation of the vector form can be achieved similarly for each scalar component. The discrete Poisson equation for point i enclosed by its control volume Ω_i can be written as

$$\int_{\Omega_i} \left(\frac{\partial \varphi_i(t)}{\partial t} + Q_i\right) d\Omega = \int_{\Omega_i} \nabla \cdot (\rho_i \nabla \varphi_i(t))\, d\Omega \tag{4.17}$$

Applying Gauss's divergence theorem, the above equation yields

$$\int_{\Omega_i} \left(\frac{\partial \varphi_i(t)}{\partial t} + Q_i\right) d\Omega = \int_{S_i} \rho_i \nabla \varphi_i(t) \cdot \mathbf{n}\, dS = \int_{S_i} \rho_i \left(\frac{\partial \varphi(t)}{\partial \mathbf{n}}\right)_i dS \tag{4.18}$$

where $\mathbf{n}$ is the outward unit normal vector at boundary surface S_i.

Writing the first term in Eq. (4.18) in a discrete form for point i yields

$$\left(\frac{\partial \varphi_i(t)}{\partial t} + Q_i\right) \Omega_i = \int_{S_i} \rho_i \left(\frac{\partial \varphi(t)}{\partial \mathbf{n}}\right)_i dS \tag{4.19}$$

which can be further arranged to

$$\frac{\partial \varphi_i(t)}{\partial t} = \frac{1}{\Omega_i} \int_{S_i} \rho_i \left(\frac{\partial \varphi(t)}{\partial \mathbf{n}}\right)_i dS - Q_i \tag{4.20}$$

where Ω_i is the volume of the control volume of point i.

Considering the neighbouring points of point i, a straightforward approximation of Eq. (4.20) may be written as

$$\frac{\partial \varphi_i(t)}{\partial t} = \frac{1}{\Omega_i} \sum_{j \in N(i)} \left[\frac{\rho_j \varphi_j(t) - \rho_i \varphi_i(t)}{l_{ij}} \sum_{n \in S(ij)} S_n\right] - Q_i \tag{4.21}$$

where $N(i)$ is the set of connected neighbouring points of point i; l_{ij} is the distance between points i and j; and $S(ij)$ is the set of surfaces attached to the edge between points i and j with each surface denoted by S_n.

Recalling the governing equation of cell state in Eq. (4.13), without cell input $v_u(t)$, Eq. (4.13) is simplified to an autonomous CNN [124] whose dynamic behaviour is written as

$$C_x \frac{dv_{xi}(t)}{dt} = -\frac{1}{R_x} v_{xi}(t) + \sum_{C(j) \in N_r(i)} A(i;j) v_{yj}(t) + I_i \tag{4.22}$$

Rearranging the discrete Poisson equation in Eq. (4.21) yields

$$\frac{\partial \varphi_i(t)}{\partial t} = -\frac{1}{\Omega_i}\sum_{j\in N(i)}\left[\frac{\rho_i}{l_{ij}}\sum_{n\in S(ij)} S_n\right]\varphi_i(t) + \frac{1}{\Omega_i}\sum_{j\in N(i)}\left[\frac{\rho_j}{l_{ij}}\sum_{n\in S(ij)} S_n\right]\varphi_j(t) - Q_i \tag{4.23}$$

It can be seen that Eqs. (4.22) and (4.23) are remarkably similar. Therefore, the discrete Poisson equation is mapped onto the CNN array by associating the parameters of the autonomous CNN with the parameters of the Poisson equation such that

$$C_x = 1;\ v_{xi}(t) = \varphi_i(t);\ v_{yj}(t) = \varphi_j(t);\ I_i = -Q_i \tag{4.24}$$

$$A(i;i) = \frac{1}{R_x} - \frac{1}{\Omega_i}\sum_{j\in N(i)}\left[\frac{\rho_i}{l_{ij}}\sum_{n\in S(ij)} S_n\right]$$

$$A(i;j) = \frac{\rho_j}{\Omega_i l_{ij}}\sum_{n\in S(ij)} S_n$$

To fully define the autonomous CNN, the initial and boundary conditions must be specified. The initial condition is realised by associating the initial potential energy with the initial state of the cell, i.e.

$$v_{xi}(0) = \varphi_i(0) \tag{4.25}$$

The Dirichlet boundary condition is realised by using fixed-state cells which enforce a specified potential energy to the related cells at the boundary of the problem domain at all times, i.e.

$$v_{x,b}(t) = \varphi \tag{4.26}$$

where $v_{x,b}(t)$ denotes the state of a cell at the boundary of the solution domain at time t.

Similarly, a three-layer CNN can be constructed for the vector form of the Poisson equation to compute the three components of the potential vector. The time evolution of the CNN array directly provides the solution to the Poisson equation, leading to the optimal distribution of mechanical load for soft tissue deformation.

4.2.1.2 CNN Formulation of Non-Rigid Mechanics of Motion

As mentioned previously, CNN represents good approximations to many dynamic systems, such as the mechanical vibrating system, which can be efficiently and effectively solved by CNN [134]. Therefore, CNN is not only used to solve the nonlinear Poisson equation for energy propagation in the object, but it is also used to solve the non-rigid mechanics of motion for dynamic simulation of soft tissue deformation. The non-rigid

mechanics of motion can be discretised in the same manner as the spatial discretisation of the Poisson equation. The discrete non-rigid mechanics of motion for point i can be written as

$$m_i \frac{\partial^2 \mathbf{P_i}}{\partial t^2} + \gamma_i \frac{\partial \mathbf{P_i}}{\partial t} + \frac{\partial W(\mathbf{P_i})}{\partial \mathbf{P_i}} = \mathbf{f_i}(\mathbf{P_i}, t) \tag{4.27}$$

The $\partial W(\mathbf{P_i})/\partial \mathbf{P_i}$ at point i can be calculated from the energy distribution resulted from the Poisson propagation. Considering point i and its neighbouring point j with potential energy φ_i and φ_j, respectively, the gradient vector of $W(\mathbf{P_i})$ at position $\mathbf{P_i}$ with respect to point j at position $\mathbf{P_j}$ can be calculated by

$$\frac{\partial W(\mathbf{P_i}, \mathbf{P_j})}{\partial \mathbf{P_i}} = -\frac{|\varphi_j - \varphi_i|}{\|\mathbf{P_j} - \mathbf{P_i}\|} \frac{\mathbf{P_j} - \mathbf{P_i}}{\|\mathbf{P_j} - \mathbf{P_i}\|} \tag{4.28}$$

Hence, the $\partial W(\mathbf{P_i})/\partial \mathbf{P_i}$ at point i can be calculated by

$$\frac{\partial W(\mathbf{P_i})}{\partial \mathbf{P_i}} = \sum_{j \in N(i)} \frac{\partial W(\mathbf{P_i}, \mathbf{P_j})}{\partial \mathbf{P_i}} = -\sum_{j \in N(i)} \frac{|\varphi_j - \varphi_i|}{\|\mathbf{P_j} - \mathbf{P_i}\|} \frac{\mathbf{P_j} - \mathbf{P_i}}{\|\mathbf{P_j} - \mathbf{P_i}\|} \tag{4.29}$$

where $N(i)$ is the set of connected neighbouring points of point i.

Substituting Eq. (4.29) into Eq. (4.27) yields

$$m_i \frac{\partial^2 \mathbf{P_i}}{\partial t^2} = -\gamma_i \frac{\partial \mathbf{P_i}}{\partial t} + \sum_{j \in N(i)} \frac{|\varphi_j - \varphi_i|}{\|\mathbf{P_j} - \mathbf{P_i}\|} \frac{\mathbf{P_j} - \mathbf{P_i}}{\|\mathbf{P_j} - \mathbf{P_i}\|} + \mathbf{f_i}(\mathbf{P_i}, t) \tag{4.30}$$

The equation of motion for the entire system can be obtained by assembling Eq. (4.30) for all the mass points in the object. The resultant system of equations can be written as

$$\mathbf{M} \frac{\partial^2 \mathbf{P}}{\partial t^2} = -\mathbf{D} \frac{\partial \mathbf{P}}{\partial t} + \mathbf{KP} + \mathbf{F} \tag{4.31}$$

where **M** is the mass matrix with m as diagonal components; **D** is the damping matrix with γ as diagonal components; **K** is the stiffness matrix encoding potential energy at neighbouring points; **P** is the position of individual points; and **F** is the force vector representing the external force which can be either constant or variable with time.

Eq. (4.31) is the second-order in the temporal domain, whereas the original CNN is only the first-order, an augmented CNN [134], which introduces a new capacitor C_y in the cell output and a new template $C(i;j)$ in the cell state, is employed to account for the second-order term. With the augmented CNN, the dynamics of a cell $C(i)$ is described by the following equations

$$C_x \frac{dv_{xi}(t)}{dt} = -\sum_{C(j)\in N_r(i)} C(i;j)v_{xi}(t) + \sum_{C(j)\in N_r(i)} A(i;j)v_{yj}(t) + \sum_{C(j)\in N_r(i)} B(i;j)v_{uj}(t) + I_i \tag{4.32}$$

$$C_y \frac{dv_{yi}(t)}{dt} = \frac{1}{2}(|v_{xi}(t) + K| - |v_{xi}(t) - K|), \qquad K \geq 1 \tag{4.33}$$

For the sake of conciseness, consider the one-dimensional case of Eq. (4.31). The position, velocity and external force are associated with cell output $v_{yj}(t)$, state $v_{xi}(t)$ and input $v_{uj}(t)$ with respective templates $\mathbf{A} = \mathbf{M}^{-1}\mathbf{K}$, $\mathbf{C} = \mathbf{M}^{-1}\mathbf{D}$ and $\mathbf{B} = \mathbf{M}^{-1}$. The cell capacitances C_x and C_y are both set to 1, whereas the cell current source I_i is set to 0 for all cells. In the general 3D case, a three-layer augmented CNN can be constructed by CNN modelling of each scalar component to compute the three components of the displacement and velocity vectors.

To fully define the augmented CNN, three initial conditions: initial position $v_{yj}(0)$, velocity $v_{xj}(0)$ and external force $v_{uj}(0)$, need to be specified. The Dirichlet boundary condition is realised by using fixed-state and fixed-output cells which enforce a fixed position to the related cells at the boundary of the solution domain at all times, i.e.

$$v_{x,b}(t) = v_{y,b}(t) = 0 \tag{4.34}$$

where $v_{x,b}(t)$ and $v_{y,b}(t)$ denote the state and output of a cell at the boundary of the problem domain at time t.

4.2.2 Results

Simulations, experiments and comparisons have been conducted to investigate the performance of the proposed method in terms of (1) mechanical behaviours, (2) isotropic and homogeneous, anisotropic and heterogeneous deformations, (3) human organ deformation, (4) comparison with the surface model method [137], and (5) computational performance. Interactive soft object deformation with haptic feedback has also been achieved with the proposed method.

4.2.2.1 Mechanical Behaviours

Experiments are conducted to verify the mechanical behaviours of the proposed method against those of real soft tissues. Fig. 4.10 shows the experimental setup, where compression tests are conducted on a lamb kidney to measure the force-displacement data. A digital force gauge whose displacement is controlled and recorded by a

micrometer barrel is used to apply a compressive force to the lamb kidney. The kidney specimen is placed in a plastic tray with oil applied to the interface of plastic tray and tissue to minimise friction. The tray is constrained from sliding by using a small weight placed inside. The compressive force is applied perpendicularly to the surface of the kidney. Meanwhile, for the purpose of comparison analysis, simulation trials were also conducted under the same conditions as the experimental analysis to simulate the mechanical behaviours of kidney tissues. Kidney tissue density $m = 1{,}050$ kg/m^3 [47] and electrical conductivity $k = 0.34$ were used in the simulation trials.

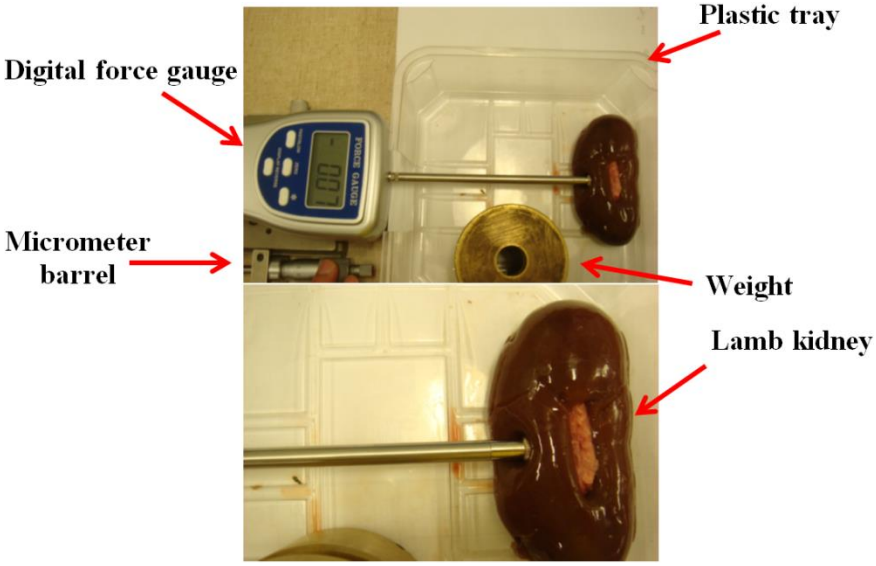

Figure 4.10 Experimental setup for measurement of force-displacement data of biological soft tissues.

Fig. 4.11 illustrates the simulated mechanical behaviours against the experimental mechanical behaviours. It can be seen that the simulated results are in agreement with the experimental curve and both deformations varied nonlinearly with the applied forces. This demonstrates that due to the nonlinearity of CNN dynamics, the proposed method can achieve nonlinear force-displacement relationship of biological soft tissues. The nonlinear force-displacement relationship further reveals that the proposed method can accommodate nonlinear deformation of soft tissues.

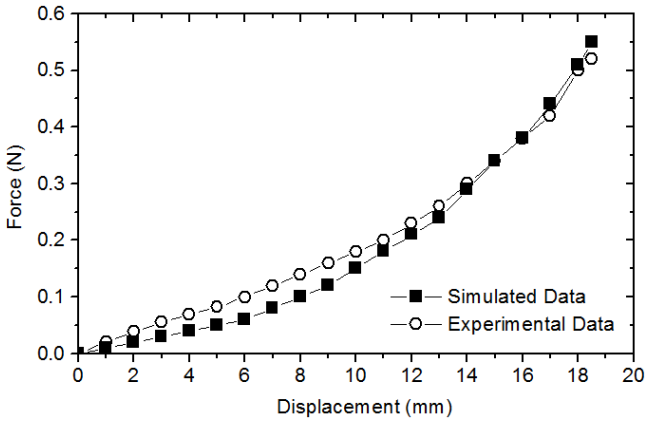

Figure 4.11 Comparison between the simulated and experimental soft tissue mechanical behaviours: both deformations vary nonlinearly with the applied forces.

4.2.2.2 Isotropic and Homogeneous, Anisotropic and Heterogeneous Deformations

As mentioned previously, the constitutive coefficient is equivalent to the elastic constant of an elastic material, which describes the physical behaviours of the material. Therefore, various material properties such as isotropic and homogeneous, anisotropic and heterogeneous materials can be modelled using the property of constitutive coefficient. Fig. 4.12 shows the deformation of an isotropic and homogeneous material under an external force applied to the centre of the top surface in the normal direction. The material is of a volumetric box shape containing 845 mass points with damping constant $\gamma = 3.0$ and constitutive coefficient $\rho = 0.08$ for all points. The distribution of potential energy and resultant deformation are illustrated in Fig. 4.12.

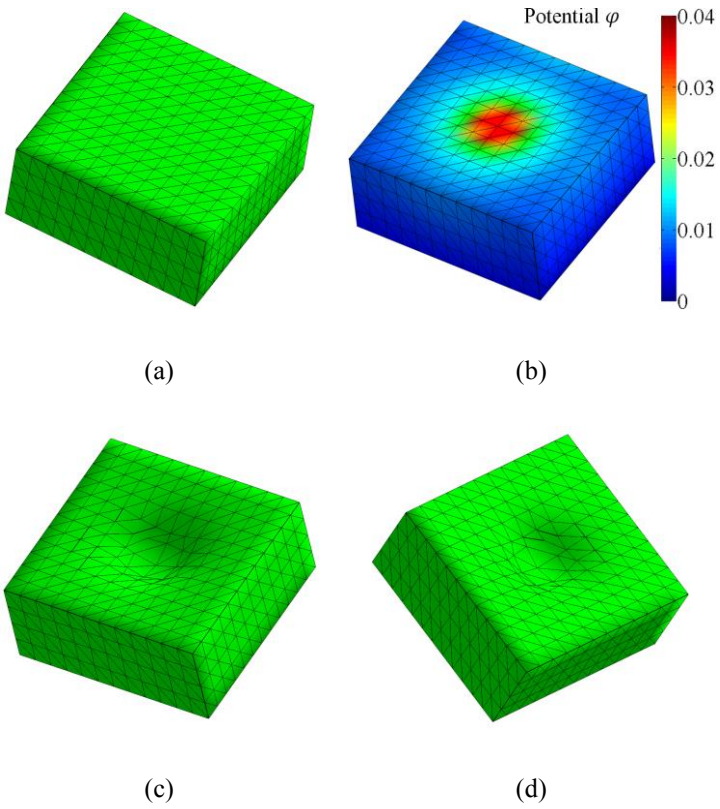

Figure 4.12 Volumetric deformation of an isotropic and homogeneous material with constitutive coefficient $\rho = 0.08$ at all points: (a) the rest state; (b) the distribution of potential energy; and (c) and (d) the respective deformation in different views.

With the same volumetric model and under the same loading conditions, the deformation of an anisotropic material is achieved by setting the constitutive coefficient to different values in different directions ($\rho = 0.24$ and 0.08 at the red and black points), whereas the deformation of a heterogeneous material is achieved by setting the constitutive coefficient to different values at different regions ($\rho = 0.24$, 0.16 and 0.08 at the red, white and black points). The anisotropic and heterogeneous deformations and their associated distributions of potential energy are shown in Fig. 4.13.

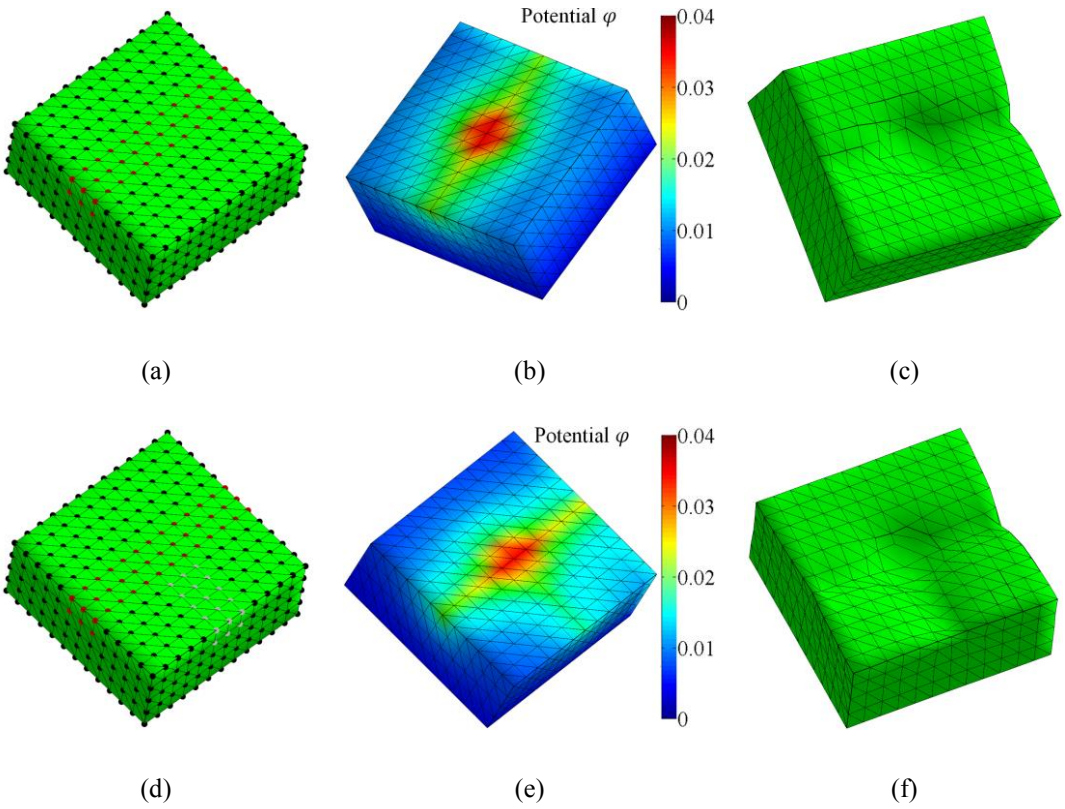

Figure 4.13 Volumetric deformations of an anisotropic and a heterogeneous material: (a) the constitutive coefficient $\rho = 0.24$ and 0.08 at the red and black points, respectively, in the anisotropic material; (b) and (c) the distribution of potential energy in the anisotropic material and associated anisotropic deformation; (d) the constitutive coefficient $\rho = 0.24$, 0.16, and 0.08 at the red, white and black points, respectively, in the heterogeneous material; and (e) and (f) the distribution of potential energy in the heterogeneous material and associated heterogeneous deformation.

Compared to the distribution of potential energy and homogeneous deformation shown in Fig. 4.12, the potential energy in the anisotropic material is distributed more significantly in the direction of red points with higher constitutive coefficient values, and hence the material is deformed more significantly along this direction around the deformation area (see Figs. 4.13(a)-(c)). Similarly, due to different constitutive coefficient values at different regions, the potential energy in the heterogeneous material is distributed differently, and thus the material is deformed differently in these regions (see Figs. 4.13(d)-(f)). With above deformation examples, all of the deformations exceed 10% of the original mesh size. Along with the nonlinear force-displacement relationship demonstrated in Fig. 4.11, it shows that the proposed method can achieve nonlinear large

deformation of soft tissues, whereas other modelling methods based on linear elasticity can only handle small deformation.

4.2.2.3 Soft Tissue Deformation with Haptic Feedback

A prototype surgical simulation system has been implemented with the proposed method for interactive soft tissue deformation with haptic feedback. As illustrated in Fig. 4.14, the prototype simulation system is a multi-thread platform with three threads for deformation simulation, haptic feedback, and visualisation. The visualisation thread is in charge of rendering the simulation scene using the OpenGL graphics library on the display monitor to provide users with visual feedback. The deformation simulation thread carries out the deformation calculation. Based on the geometry and material properties of the soft tissue model, the deformation of the soft tissue is calculated through the CNN modelling of propagation of mechanical load and non-rigid mechanics of motion. Finally, the manipulation and force feedback are achieved by the haptic thread via a PHANToM haptic device from Geomagic supported by the OpenHaptic toolkit. The user can manipulate objects via the virtual haptic probe of the PHANToM haptic device and interactively deform the virtual soft tissue model with force feedback. Fig. 4.15 shows an interactive deformation of a virtual volumetric human liver model with haptic feedback.

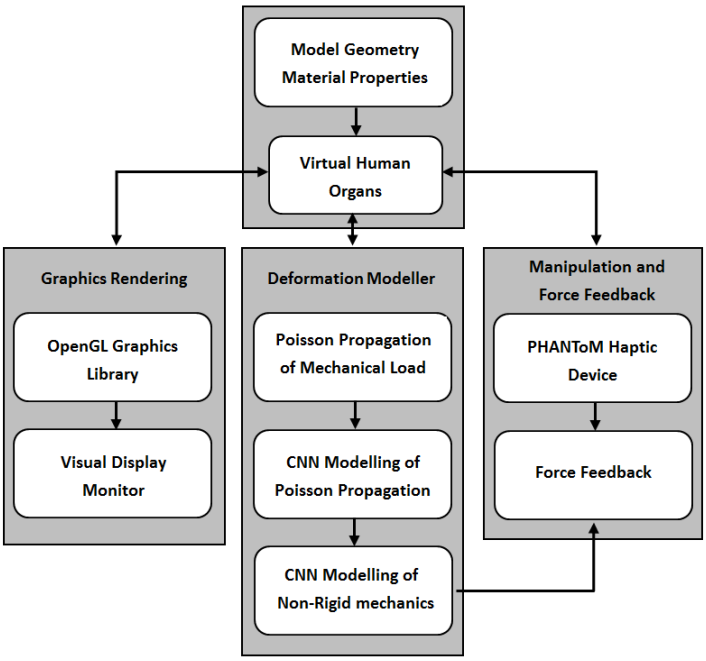

Figure 4.14 System overview of the prototype surgical simulation system with haptic feedback.

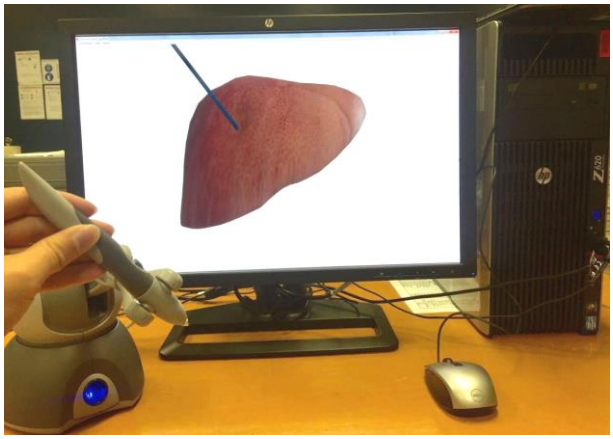

Figure 4.15 Interactive deformation of a virtual human liver via the virtual haptic probe.

Fig. 4.16 illustrates the deformation of a virtual human liver model by the proposed method.

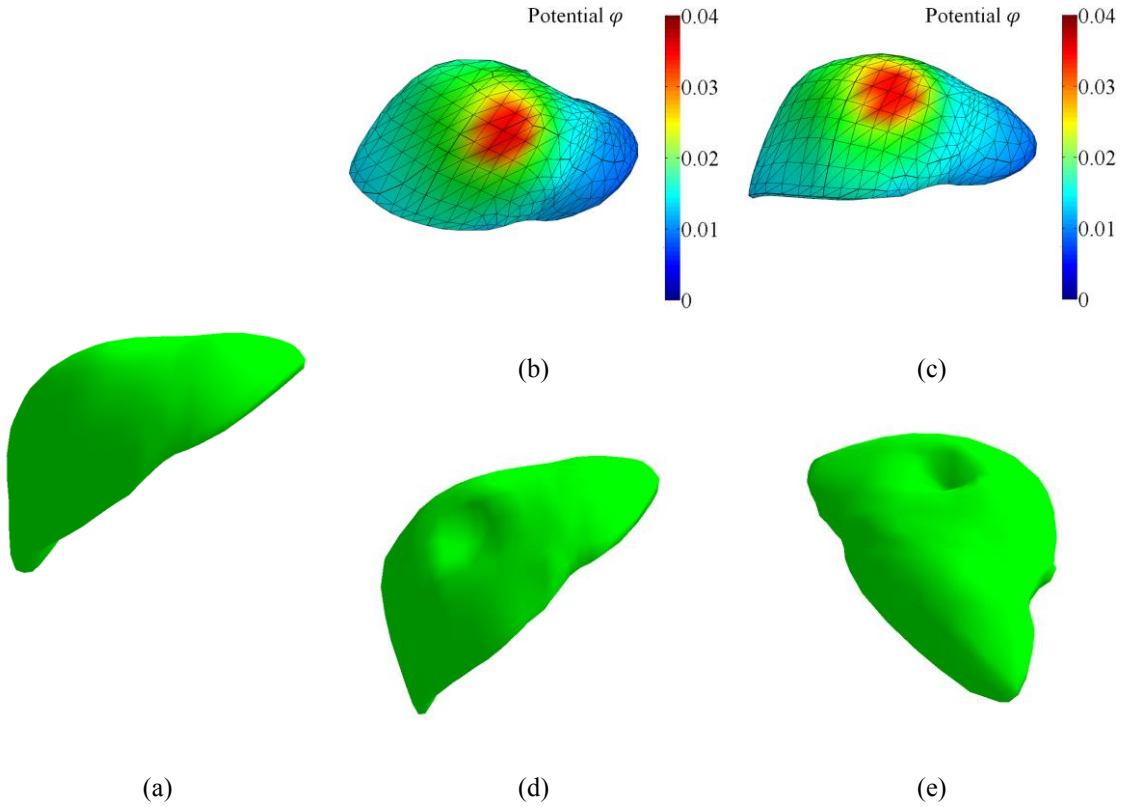

Figure 4.16 Deformation of a volumetric human liver model: (a) the rest state; (b) and (c) the distribution of potential energy; and (d) and (e) the liver deformation in different views.

4.2.2.4 Visual and Haptic Performances

The proposed method is programmed in C++ and implemented on an Intel(R) Core(TM) i7-5500U CPU@2.40 GHz and 4 GB RAM memory PC without hardware acceleration. With one external stimulus, the computational time utilising different numbers of points is illustrated in Fig. 4.17. It can be seen that the computational time is increased with the increase in numbers of mass points. The visually satisfactory refresh rate of 30 Hz (33 ms per iteration) to maintain a realistic visual feedback is achieved with a volumetric model of around 1,500 mesh points. Since the minimum requirement for correct visualisation of an object is around 600 points [138], it is more than sufficient to provide realistic visual feedback with the proposed method. However, under the same conditions, the computational time per iteration for linear FEM [57] is 1.1 s. This demonstrates the proposed method has a much better computational performance than linear FEM. The computational performance of the proposed method can be further improved by CNN hardware implementation [139] and adaptive technique [140].

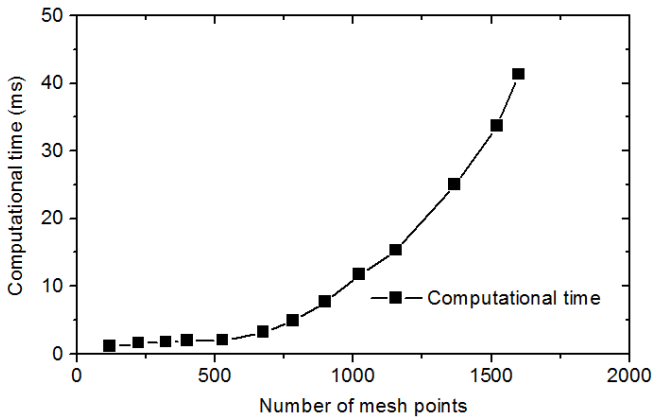

Figure 4.17 Visual performance: the visually satisfactory refresh rate of 30 Hz (33 ms) is achieved with around 1,500 mesh points.

The PHANToM haptic device requires forces to be updated at the rate of at least 1,000 Hz for realistic force feedback. As it can be seen from Fig. 4.18, the force update rate is above 1,000 Hz when the number of points is around 500 mesh points. When the computational speed cannot meet the haptic refresh update requirement, force extrapolation [120, 141] is employed to improve the realism of haptic feedback by generating missing forces from the previous calculation loop.

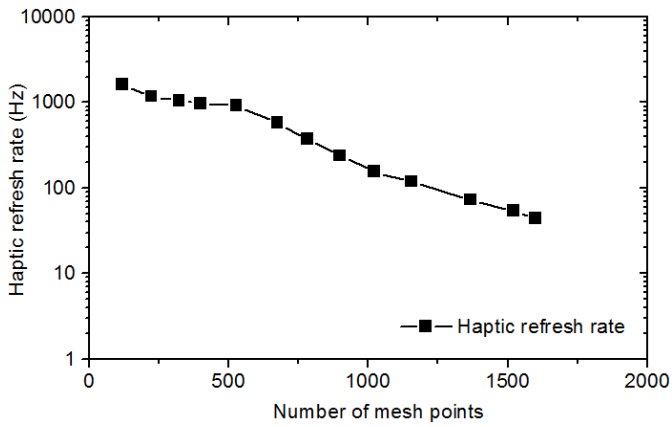

Figure 4.18 Haptic performance: the force update rate of 1,000 Hz for realistic force feedback is achieved with around 500 mesh points.

4.3 Neural Dynamics-based Stable Simulation of Soft Tissue Deformation

In addition to the requirements of real-time computational performance and physical realism for soft tissue simulation, numerical stability of integration in the temporal domain also plays a key factor in interactive surgical simulation. Currently, the mechanical dynamics of soft tissue deformation is achieved by numerical time integrations such as the explicit or implicit integrations; however, the explicit integration is stable only under a small time step, whereas the implicit integration is computationally expensive despite the accommodation of a large time step. In this chapter, the proposed neural dynamics-based methodology is demonstrated that it can achieve stable simulation of soft tissue deformation thanks to the nonlinear characteristics of CNN. It can achieve good accuracy at a small time step, while still remaining stable at a large time step, both achieved with the computational efficiency of the explicit integration.

4.3.1 Nonlinear Template of Neural Dynamics

As shown in Fig. 4.19, cell output $v_{yi}(t)$ is represented by a nonlinear function $f\big(v_{xi}(t)\big)$ with the following nonlinear properties

$$df\big(v_{xi}(t)\big)/dv_{xi}(t) = 1, \text{ if } |v_{xi}| < K \tag{4.35}$$

$$df\big(v_{xi}(t)\big)/dv_{xi}(t) = 0, \text{ if } |v_{xi}| \geq K$$

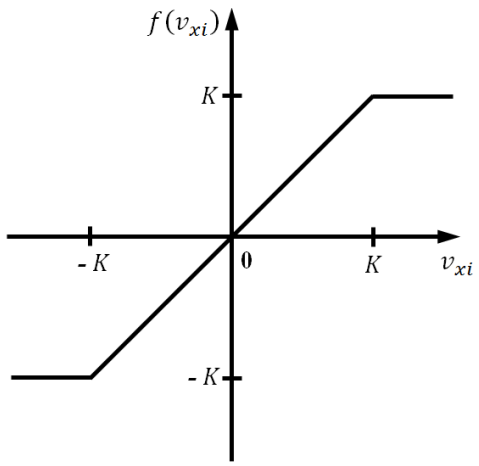

Figure 4.19 Characteristics of the nonlinear voltage-controlled source in the CNN: $f\big(v_{xi}(t)\big)$ is a nonlinear function of $v_{xi}(t)$, and K is the saturation voltage of the voltage-controlled source.

The saturation voltage K of the nonlinear voltage-controlled source in the proposed CNN controls the maximum output of a cell. Since the augmented CNN is second-order in the temporal domain and is used for modelling the dynamics of soft tissue deformation where the cell output is associated with point position, the saturation voltage K actually controls the maximum velocity of point movement. This property can be used to achieve stable soft tissue simulation.

4.3.2 Results

Simulations and comparisons are conducted on (1) a mass-spring-damper system and (2) soft tissue deformation to investigate the performance of the proposed method in terms of stable dynamic simulation.

4.3.2.1 Mass-Spring-Damper System

To demonstrate the performance of the proposed CNN model, consider a simple mass-spring-damper system illustrated in Fig. 4.20(a), where a weight with mass m at position $P_y = -1$ m is connected to the origin at $P_y = 0$ m by a spring with stiffness k and rest length l_0 and a damper with damping coefficient d. The weight undergoes a damped vibration in the y direction. The parameters are set to $m = 0.2$ kg, $k = 400$ N/m, $d = 2$, $l_0 = 1$ m and initial velocity $v_y = -5$ m/s. Fig. 4.20(b) illustrates the solutions calculated by the explicit integration under different time steps in comparison with analytical solution as reference. It can be seen that at a

small time step (e.g. $t = 0.0008$ s) the explicit integration can achieve a good approximation which is almost identical to the reference solution. However, the solutions become unstable and diverge at a large time step (e.g. $t = 0.01$ s).

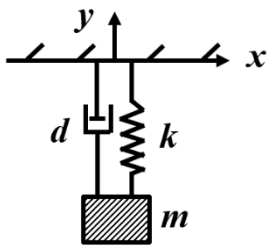

(a)

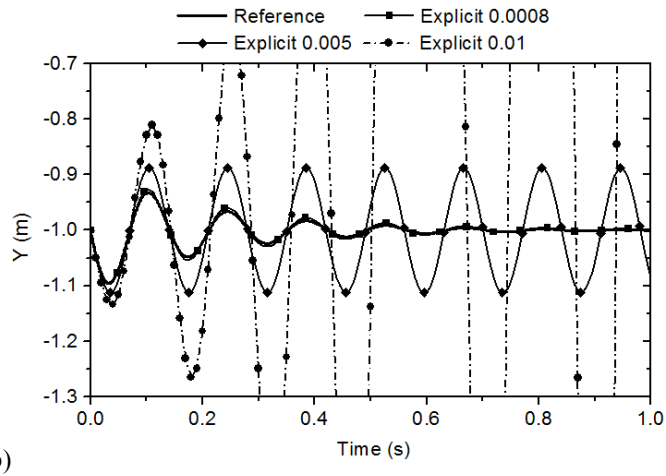

(b)

Figure 4.20 (a) A simple mass-spring-damper system with mass m, stiffness k and damping coefficient d; and (b) solutions of explicit integration with different time steps.

With the above same time steps, the CNN solutions shown in Fig. 4.21(a) are better than those of the explicit integration. At a small time step (e.g. $t = 0.0008$ s), the CNN solution ($K = 5.0$) is almost identical to the reference solution. At a large time step (e.g. $t = 0.01$ s), unlike the unstable behaviour of the explicit integration, the CNN solution remains stable. A more clear illustration can be seen from Fig. 4.21(b), which demonstrates that the CNN solution is stable whereas the explicit integration's solution is divergent at a large time step.

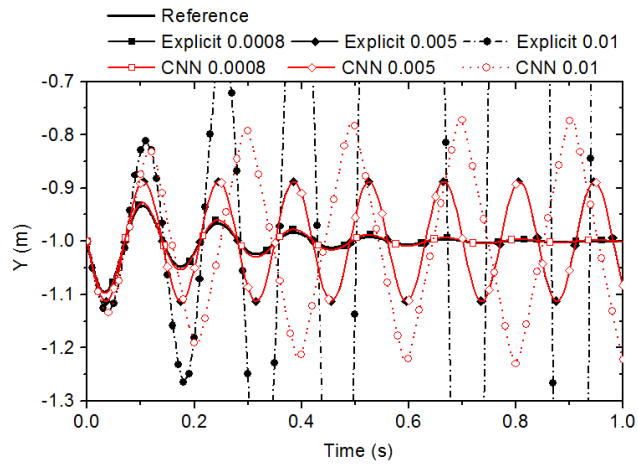

(a)

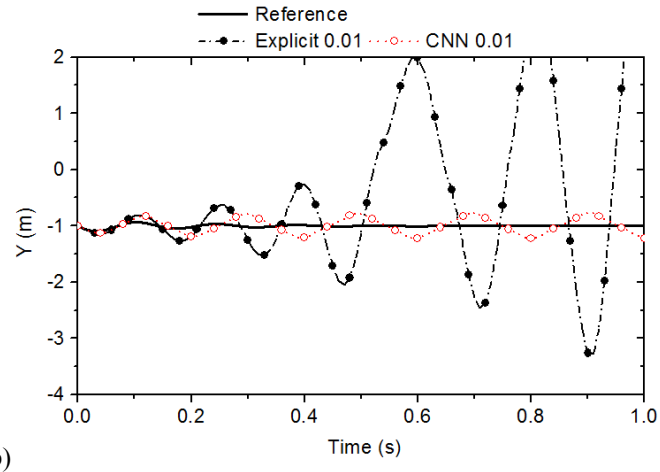

(b)

Figure 4.21 (a) A comparison between the explicit integration and CNN; and (b) the CNN solution remains stable at a large time step.

Trials with three different K values (saturation voltage $K = 5$, 4 and 2) were also conducted to examine the effect of K on the CNN solution. As illustrated in Fig. 4.22(a), the CNN solutions are converged for various K values at a small time step, and they all have a good approximation to the reference solution. Among them, the CNN solutions with $K = 5$ and $K = 4$ are much better than that with $K = 2$. This is because the cell state $v_x(t)$ is always in the region of $df\left(v_{xi}(t)\right)/dv_{xi}(t) = 1$ of the nonlinear voltage-controlled source. With the smaller value $K = 2$, the cell state $v_x(t)$ falls into the region of $df\left(v_{xi}(t)\right)/dv_{xi}(t) = 0$ of the nonlinear voltage-controlled source, leading to a damped velocity for position calculation. Hence, the results are affected at a small time step with smaller displacements than the reference solution (see the case of $K = 2$ in Fig. 4.22(a)). However, as shown in Fig. 4.22(b), at a large time step, the smaller the value of K is, the better the CNN

solution is, and thus the better the soft tissue deformation is. The above demonstrates that a smaller K value is preferred to ensure numerical accuracy while maintaining stability at a large time step.

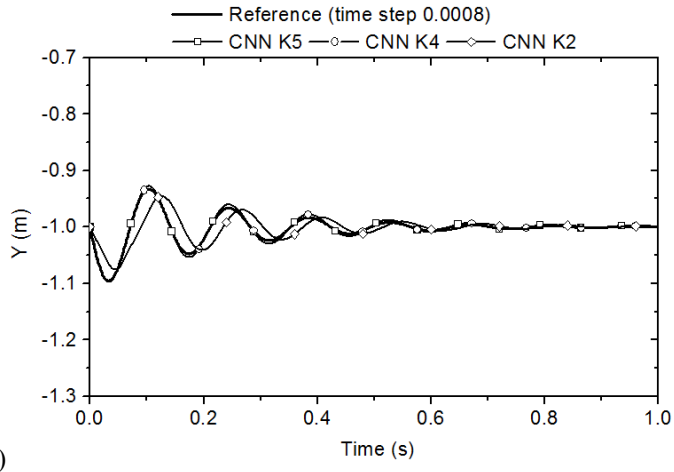

(a)

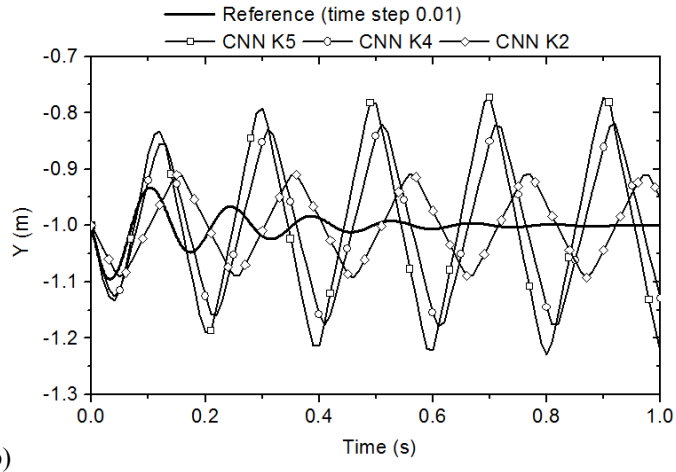

(b)

Figure 4.22 Comparisons between different K values in the proposed CNN at (a) a small time step and (b) a large time step.

4.3.2.2 Soft Tissue Deformation

Trials are also conducted on a cubic volumetric model of 1,331 mass points and 6,000 tetrahedrons, with side faces fixed (see Fig. 4.23(a)) subjected to an applied force on the top surface in the normal direction, to evaluate the performance of the proposed CNN in terms of simulating soft tissue deformation. The mass matrix **M**, damping matrix **D** and stiffness matrix **K** are initialised according to the formulation proposed by Duan *et al.*[8], where the mass density m and Young's modules E were set to 1,060 kg/m^3 [119] and 3,500 Pa [118] of the soft

tissue material properties, respectively. Both CNN and explicit integration were conducted under the same conditions with $K = 4$ used in the CNN. As shown in Fig. 4.23(b), both methods yield identical results at the small time step $t = 0.001$ s. However, as shown in Fig.4.23(c), the solution of the explicit integration becomes unstable at the large time step $t = 0.02$ s, whereas the CNN solution remains stable in Fig. 4.23(d). This demonstrates that the CNN not only inherits the accuracy of the explicit integration at a small time step but also overcomes the unstable problem of the explicit integration at a large time step. It should be mentioned that the computational time of one iteration for both CNN and explicit integration are similar which is around 2 ms.

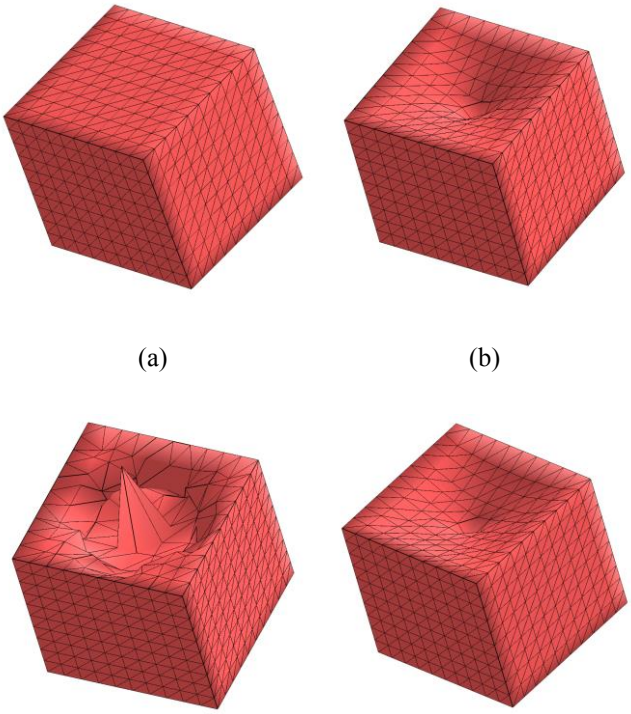

(a) (b)

(c) (d)

Figure 4.23 Comparison between the proposed CNN and explicit integration at a small and large time step: (a) cubic volumetric model at rest state; (b) both solutions at a small time step $t = 0.001$ s; (c) explicit integration at a large time step $t = 0.02$ s; and (d) CNN solution at a large time step $t = 0.02$ s.

Trials were also conducted on a human kidney model with a mesh size of 1,378 nodes and 4,691 tetrahedrons to evaluate the performance of the proposed CNN in terms of stable soft tissue simulation. Both CNN and explicit integration were conducted under same conditions with $K = 4$ used in the CNN. As shown in Fig. 4.24(b), both methods yield identical results at the small time step $t = 0.0008$ s. However, as shown in Fig. 4.24(c), the

solution of the explicit integration becomes unstable at the large time step $t = 0.01$ s, whereas the CNN solution remains stable in Fig. 4.24(d).

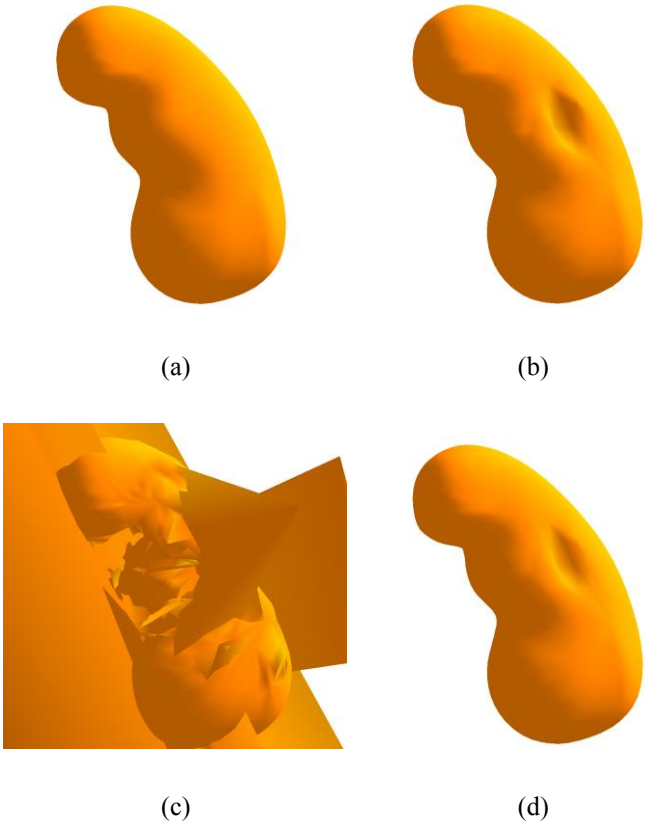

Figure 4.24 Comparison between the proposed CNN and explicit integration both at a small and large time step: (a) volumetric kidney model at rest state; (b) both solutions at a small time step $t = 0.0008$ s; (c) explicit integration at a large time step $t = 0.01$ s; and (d) CNN solution at a large time step $t = 0.01$ s.

5. Energy Balance Method

In this chapter, a novel methodology is presented for modelling of soft tissue deformation for surgical simulation, from the standpoint of work-energy balance based on the law of conservation of energy. The work done by an external force is always balanced against the strain energy due to the internal force of an object. A position-based incremental approach is established, in which the work-energy balance is achieved via an iterative position increment process for the new equilibrium state of the object. The position-based incremental approach is further combined with non-rigid mechanics of motion to govern the dynamics of soft tissue deformation. The proposed method employs nonlinear geometric and material formulations to account for nonlinear soft tissue deformation. Soft tissue material properties can be accommodated by specifying strain energy density functions. Integration with a haptic device is achieved for soft tissue deformation with haptic feedback for surgical simulation. Experimental results demonstrate that the deformations by the proposed method are in good agreement with those by the commercial package of finite element analysis. Isotropic and anisotropic deformations, as well as soft tissue viscoelastic behaviours, can be accommodated by the proposed methodology via strain energy density functions.

5.1 Formulation of Energy Balance Method

As mentioned previously, surgical simulation requires both realistic and real-time performances of soft tissue deformation. To this end, the proposed energy balance method (EBM) conducts soft tissue deformation via a position-based increment in an iterative process to achieve work-energy balance for new equilibrium state of soft tissues. It employs the concept of strain energy to incorporate both geometric and material nonlinear formulations for soft tissue deformation. Soft tissue constitutive models of material properties such as compressibility and incompressibility, isotropy and anisotropy, and viscoelasticity are also developed and integrated with the proposed EBM via strain energy density functions.

5.1.1 Theory

The proposed EBM is based on the law of conservation of energy to balance the input energy with stored energy under the condition that there is no energy loss to the environment. For a time continuous domain Ω, the law of conservation of energy states that

$$\frac{\partial W_{in}}{\partial t} - \frac{\partial W_{out}}{\partial t} = \frac{\partial W_{stored}}{\partial t} \in \Omega \tag{5.1}$$

where W_{in} is the input energy, W_{out} is the lost energy, and W_{stored} is the stored energy in the domain Ω at time t.

It can be seen from Eq. (5.1) that soft tissue deformation is actually a process of work-energy balance. When a soft tissue is subject to an external force, the soft tissue experiences deformation. As per the law of conservation of energy, if there is no energy loss to the environmental surroundings, the work done by the external force can be considered as the input energy W_{in} supplied to the soft tissue, and it is balanced against the stored energy W_{stored}, i.e. the strain energy W_{strain}, which describes the energy to deform the soft tissue away from its natural state under the internal force. The work-energy balance of soft tissue deformation can be written as

$$\int_{\Gamma_f} \mathbf{F}_{ext} \cdot \mathbf{S}_{ext}\, d\Gamma_f = W_{strain} = \int_{\Omega} \mathbf{F}_{int} \cdot \mathbf{S}_{int}\, d\Omega \tag{5.2}$$

where Ω represents the whole geometry of the soft tissue with its natural boundary denoted by Γ_f, $\mathbf{F}_{ext}$ and $\mathbf{S}_{ext}$ are the external force and displacement, respectively, $\mathbf{F}_{int}$ and $\mathbf{S}_{int}$ are the internal force and displacement, respectively, and the symbol "·" represents the dot product of two vectors.

Hence, from the viewpoint of work-energy balance, the deformation process of soft tissues can be treated as a process of applying the work done by the external force to the soft tissue and subsequently balancing this work with the strain energy due to internal force.

For hyperelastic materials, the internal force can be described by the gradient of strain energy with respect to deformation. Consider a particle i at position $\mathbf{x}_i$, the internal force $\mathbf{f}_{int}(\mathbf{x}_i)$ exerted on particle i is described by

$$\mathbf{f}_{int}(\mathbf{x}_i) = -\frac{\partial W_{strain}(\mathbf{x}_i)}{\partial \mathbf{x}_i} \tag{5.3}$$

As per the principle of virtual work in continuum mechanics [117], in order to guarantee that both linear and angular momentums are conserved during soft tissue deformation, the position increment $\Delta\mathbf{x}_i$ of particle i due to internal force $\mathbf{f}_{int}(\mathbf{x}_i)$ can be defined as

$$\Delta\mathbf{x}_i = -w_i \lambda_i \frac{\partial W_{strain}(\mathbf{x}_i)}{\partial \mathbf{x}_i} \tag{5.4}$$

where $w_i = 1/\, m_i$ is the inverse mass, and λ_i is the Lagrange multiplier of particle i.

If the variation of internal force is small within the time step, the strain energy of displacement $\Delta\mathbf{x}_i$ under internal force $\mathbf{f}_{int}(\mathbf{x}_i)$ for particle i can be calculated as

$$W_{strain}(\mathbf{x}_i) = \mathbf{f}_{int}(\mathbf{x}_i) \cdot \Delta\mathbf{x}_i \tag{5.5}$$

Substituting Eqs. (5.3) and (5.4) into Eq. (5.5) and solving for the Lagrange multiplier λ_i yield

$$\lambda_i = \frac{W_{strain}(\mathbf{x}_i)}{w_i \left\| \frac{\partial W_{strain}(\mathbf{x}_i)}{\partial \mathbf{x}_i} \right\|^2} \tag{5.6}$$

where the symbol "$\|\cdot\|$" represents the modulus of the gradient vector of strain energy at a given point.

Since a soft tissue model is discretised into a number of finite elements with particles (nodes) joining together, the position increment of a particle can be calculated by taking the sum of position increments contributed from all the neighbouring elements of this particle. Let $T(\mathbf{x}_i)$ be the set of neighbouring elements joining at particle i, $T_k(\mathbf{x}_i)$ an element joining at particle i with $T_k(\mathbf{x}_i) \in T(\mathbf{x}_i)$. For element $T_k(\mathbf{x}_i)$, the Lagrange multiplier $\lambda_{i,k}$ for position increment $\Delta\mathbf{x}_{i,k}$ contributed by element $T_k(\mathbf{x}_i)$ can be determined by

$$\lambda_{i,k} = \frac{W_k(\mathbf{x}_i)}{\sum_{j \in N(T_k(\mathbf{x}_i))} w_{j,k} \left\| \frac{\partial W_k(\mathbf{x}_{j,k})}{\partial \mathbf{x}_{j,k}} \right\|^2} \tag{5.7}$$

where $W_k(\mathbf{x}_i)$ is the strain energy of element $T_k(\mathbf{x}_i)$; $N(T_k(\mathbf{x}_i))$ is the set of particles in element $T_k(\mathbf{x}_i)$; and $w_{j,k}$ and $\mathbf{x}_{j,k}$ denote the inverse mass and position vector of particle j in element $T_k(\mathbf{x}_i)$, respectively.

Based on Eq. (5.7), the position increment $\Delta\mathbf{x}_{i,k}$ contributed by element $T_k(\mathbf{x}_i)$ can be written as

$$\Delta\mathbf{x}_{i,k} = -w_i \frac{W_k(\mathbf{x}_i)}{\sum_{j \in N(T_k(\mathbf{x}_i))} w_{j,k} \left\| \frac{\partial W_k(\mathbf{x}_{j,k})}{\partial \mathbf{x}_{j,k}} \right\|^2} \frac{\partial W_k(\mathbf{x}_i)}{\partial \mathbf{x}_i} \tag{5.8}$$

The net position increment $\Delta\mathbf{x}_i$ of particle i is calculated by taking the sum of $\Delta\mathbf{x}_{i,k}$ from all the neighbouring contributing elements $T_k(\mathbf{x}_i) \in T(\mathbf{x}_i)$ of particle i, i.e.

$$\Delta\mathbf{x}_i = \sum_{T_k(\mathbf{x}_i) \in T(\mathbf{x}_i)} \Delta\mathbf{x}_{i,k} \tag{5.9}$$

5.1.2 Discretisation

Since the variation of strain energy is zero of an element in the absence of external force, Eq. (5.8) holds only when an external force exists to seek a new equilibrium state for the entire system. To determine the position

increment $\Delta\mathbf{x}_i$ of particle i in Eq. (5.9), it is necessary to determine the strain energy and associated gradient vector at each node, as shown in Eq. (5.8).

Consider a soft tissue model discretised using four-node linear tetrahedral elements. Let $\mathbf{x}_1$, $\mathbf{x}_2$, $\mathbf{x}_3$ and $\mathbf{x}_4$ denote the four nodes of a tetrahedral element T_k. The gradient vector of the strain energy at each node can be determined by

$$\left[\frac{\partial W_k(\mathbf{x}_1)}{\partial \mathbf{x}_1} \quad \frac{\partial W_k(\mathbf{x}_2)}{\partial \mathbf{x}_2} \quad \frac{\partial W_k(\mathbf{x}_3)}{\partial \mathbf{x}_3}\right] \tag{5.10}$$

$$= V_k \left[\frac{\partial \Psi_k(\mathbf{x}_1)}{\partial \mathbf{x}_1} \quad \frac{\partial \Psi_k(\mathbf{x}_2)}{\partial \mathbf{x}_2} \quad \frac{\partial \Psi_k(\mathbf{x}_3)}{\partial \mathbf{x}_3}\right]$$

$$= V_k \mathbf{F} \cdot \mathbf{S} \cdot \frac{\partial \mathbf{F}}{\partial \mathbf{x}}$$

$$= V_k \mathbf{D}_\mathbf{x} \cdot \mathbf{D}_\mathbf{X}^{-1} \cdot \mathbf{S} \cdot \mathbf{D}_\mathbf{X}^{-\mathrm{T}}$$

$$\frac{\partial W_k(\mathbf{x}_4)}{\partial \mathbf{x}_4} = -\sum_{i=1}^{3} \frac{\partial W_k(\mathbf{x}_i)}{\partial \mathbf{x}_i}$$

where V_k is the volume, Ψ_k is the strain energy density, $\mathbf{F}$ is the deformation gradient, and $\mathbf{S}$ is the second Piola-Kirchhoff stress of element T_k (see Chapter 5.2); $\mathbf{D}_\mathbf{x}$ and $\mathbf{D}_\mathbf{X}$ are the deformed and undeformed shape matrices of the tetrahedron with respect to the local coordinates, which are defined by

$$\mathbf{D}_\mathbf{x} = [\mathbf{x}_1 - \mathbf{x}_4 \quad \mathbf{x}_2 - \mathbf{x}_4 \quad \mathbf{x}_3 - \mathbf{x}_4] \tag{5.11}$$

$$\mathbf{D}_\mathbf{X} = [\mathbf{X}_1 - \mathbf{X}_4 \quad \mathbf{X}_2 - \mathbf{X}_4 \quad \mathbf{X}_3 - \mathbf{X}_4]$$

where $\mathbf{X}$ is the position vector of a particle in the undeformed configuration, and $\mathbf{x}$ is the position vector of the particle in the deformed configuration.

5.1.3 Model Dynamics

To achieve physical animation, the dynamics of discretised soft tissue model need to be solved at each time step during the simulation. Explicit time integration [60] and implicit time integration [102] are the two popular numerical schemes to evolve model dynamics in the temporal domain. The explicit integration is easy to implement and computationally efficient since it does not require the calculation of stiffness matrix inversion for model update. However, the time step in the explicit integrations is limited by a critical value to achieve stable

solutions. The implicit integration does not suffer from numerical instability, but it requires the calculation of stiffness matrix inversion or solving a linear system of equations at each iteration, leading to an expensive computational load. The explicit symplectic integration [142] is also a numerical integration scheme. It can achieve energy conservation via a high-order approximation, but at the cost of additional computational complexity.

For the sake of simplicity and fast computation, the proposed EBM is proceeded in time using a first-order explicit forward scheme. Since the explicit scheme is only conditionally stable, precautions need to be taken for the time step to ensure numerical stability. The critical time step Δt_{cr} can by determined by [56]

$$\Delta t_{cr} \leq \frac{L_e}{c} \tag{5.12}$$

where L_e is the smallest characteristic length of an element in the mesh, and c is the dilatational wave speed.

The algorithm of the proposed EBM is shown in Fig. 5.1. At each time step Δt, the new position of particle i is first calculated by considering the external force only, which is equivalent to applying the work done by the external force to the soft tissue

$$\mathbf{x}_i{}^{t+\Delta t} \leftarrow \mathbf{x}_i{}^{t} + \Delta t \left(\mathbf{v}_i{}^{t} + \Delta t \frac{\mathbf{f}_{ext}{}^{t}}{m_i} \right) \tag{5.13}$$

where $\mathbf{x}_i{}^{t+\Delta t}$ and $\mathbf{x}_i{}^{t}$ are the positions of particle i at time $t + \Delta t$ and t, respectively; $\mathbf{v}_i{}^{t}$ is the velocity of particle i at time t, $\mathbf{f}_{ext}{}^{t}$ is the external force applied to particle i at time t, and m_i is the mass of particle i.

The work-energy balance can be achieved in only one iteration if only one finite element is considered; however, since the soft tissue object is discretised into a number of finite elements, it leads to an iterative process to achieve work-energy balance for the entire soft tissue model. With the new position of particle i given by Eq. (5.13), the equilibrium state is sought by satisfying the work-energy balance iteratively via the position increment $\Delta \mathbf{x}_i$ applied to each particle i, i.e.

$$\mathbf{x}_i{}^{t+\Delta t} \leftarrow \mathbf{x}_i{}^{t+\Delta t} + \Delta \mathbf{x}_i \tag{5.14}$$

where $\Delta \mathbf{x}_i$ is calculated based on Eq. (5.9) by considering position increment $\Delta \mathbf{x}_{i,k}$ from neighbouring tetrahedral elements $T_k(\mathbf{x}_i)$.

The new velocity $\mathbf{v}_i{}^{t+\Delta t}$ of particle i at time $t + \Delta t$ is calculated once the new equilibrium state is reached. The $\mathbf{v}_i{}^{t+\Delta t}$ is calculated by

$$\mathbf{v}_i^{t+\Delta t} \leftarrow \frac{\mathbf{x}_i^{t+\Delta t} - \mathbf{x}_i^{t}}{\Delta t} \tag{5.15}$$

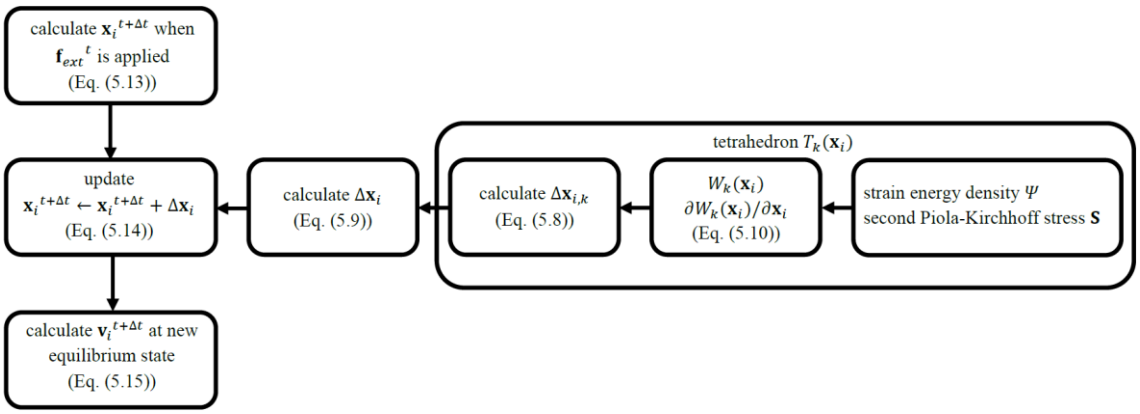

Figure 5.1 EBM algorithm.

5.2 Strain Energy Density

The strain energy density is a measure of strain energy stored in a small volume element in the material. The strain energy density at a particle can be expressed by

$$\Psi = \int_{\boldsymbol{\varepsilon}} \boldsymbol{\sigma}\, d\boldsymbol{\varepsilon} \tag{5.16}$$

where $\boldsymbol{\sigma}$ and $\boldsymbol{\varepsilon}$ are the stress and strain at the particle.

Since the strain energy is zero when the object is at the rest state, it is straightforward to measure the variations of stress and strain at the particle with reference to the rest state. The stress and strain at the particle can be expressed by the second Piola-Kirchhoff stress $\mathbf{S}$ and Green-Saint Venant strain $\mathbf{E}$. The Green-Saint Venant strain $\mathbf{E}$ can be calculated by

$$\mathbf{E} = \frac{1}{2}(\mathbf{C} - \mathbf{I}) \tag{5.17}$$

where $\mathbf{I}$ is the identity matrix of the second rank, and $\mathbf{C}$ is the right Cauchy-Green deformation tensor given by $\mathbf{C} = \mathbf{F}^{\mathrm{T}} \cdot \mathbf{F}$, where $\mathbf{F}$ is the deformation gradient given by

$$\mathbf{F} = \frac{\partial \mathbf{x}}{\partial \mathbf{X}} \tag{5.18}$$

The gradient vector of strain energy density at a given particle in the deformed configuration can be determined by

$$\frac{\partial \Psi}{\partial \mathbf{x}} = \mathbf{F} \cdot \mathbf{F}^{-1} \cdot \frac{\partial \Psi}{\partial \mathbf{F}} \cdot \frac{\partial \mathbf{F}}{\partial \mathbf{x}} = \mathbf{F} \cdot \mathbf{S} \cdot \frac{\partial \mathbf{F}}{\partial \mathbf{x}} \tag{5.19}$$

5.2.1 Isotropic Materials

Various soft tissue materials can be applied to the proposed EBM method. For the purpose of conciseness, let us first consider an isotropic hyperelastic material. Its strain energy density can be described as a function of the invariants of the right Cauchy-Green deformation tensor, i.e.

$$\Psi = \Psi(I_1, I_2, I_3) \tag{5.20}$$

where I_1, I_2 and I_3 are the three invariants of the right Cauchy-Green deformation tensor $\mathbf{C}$, which are given by

$$I_1 = \mathrm{tr}(\mathbf{C});\ I_2 = \frac{1}{2}[[\mathrm{tr}(\mathbf{C})]^2 - \mathrm{tr}(\mathbf{C}^2)];\ I_3 = \det(\mathbf{C}) \tag{5.21}$$

where $\mathrm{tr}(\cdot)$ and $\det(\cdot)$ denote the trace and determinant of a matrix.

The second Piola-Kirchhoff stress $\mathbf{S}$ can be calculated in terms of the strain energy density Ψ and right Cauchy-Green deformation tensor $\mathbf{C}$

$$\mathbf{S} = 2\frac{\partial \Psi}{\partial \mathbf{C}} = 2\left(\frac{\partial \Psi}{\partial I_1}\frac{\partial I_1}{\partial \mathbf{C}} + \frac{\partial \Psi}{\partial I_2}\frac{\partial I_2}{\partial \mathbf{C}} + \frac{\partial \Psi}{\partial I_3}\frac{\partial I_3}{\partial \mathbf{C}}\right) \tag{5.22}$$

with relations [143]:

$$\frac{\partial I_1}{\partial \mathbf{C}} = \mathbf{I};\ \frac{\partial I_2}{\partial \mathbf{C}} = I_1\mathbf{I} - \mathbf{C};\ \frac{\partial I_3}{\partial \mathbf{C}} = I_2\mathbf{I} - I_1\mathbf{C} + \mathbf{C}^2 \tag{5.23}$$

5.2.2 Compressibility

When there is a certain compressibility involved in the deformation of materials, the strain energy density may be decomposed into a volumetric part Ψ^{vol} and an isochoric part Ψ^{iso} [71], i.e.

$$\Psi = \Psi^{iso}(\bar{I}_1, \bar{I}_2) + \Psi^{vol}(J) \tag{5.24}$$

where $\bar{I_1}$ and $\bar{I_2}$ are the invariants of the isochoric part of the right Cauchy-Green deformation tensor and J is the volume ratio. $\bar{I_1}$, $\bar{I_2}$ and J can be calculated by

$$J = \det(\mathbf{F});\ \bar{I_1} = \mathrm{tr}(\bar{\mathbf{C}});\ \bar{I_2} = \frac{1}{2}[[\mathrm{tr}(\bar{\mathbf{C}})]^2 - \mathrm{tr}(\bar{\mathbf{C}}^2)] \tag{5.25}$$

where $\bar{\mathbf{C}}$ is the isochoric part of the right Cauchy-Green deformation tensor given by $\bar{\mathbf{C}} = J^{-2/3}\mathbf{C}$.

5.2.3 Anisotropy

Anisotropic materials, which exhibit directional-dependent behaviours, can also be accommodated via a modified strain energy density function. Employing a unit vector $\mathbf{a}^0$ in the rest state to describe local fibre direction [143], the strain energy density can be expressed by

$$\Psi = \Psi(I_1, I_2, I_3, I_4, I_5) \tag{5.26}$$

where I_1, I_2 and I_3 are the invariants of the right Cauchy-Green deformation tensor $\mathbf{C}$ given by Eq. (5.21); and I_4 and I_5 are the two additional invariants, which arise from the anisotropy introduced by the local fibre. I_4 and I_5 along with their derivatives with respect to $\mathbf{C}$ can be calculated by [143]

$$I_4 = \mathbf{a}^0 \cdot \mathbf{C} \cdot \mathbf{a}^0;\ I_5 = \mathbf{a}^0 \cdot \mathbf{C}^2 \cdot \mathbf{a}^0 \tag{5.27}$$

$$\frac{\partial I_4}{\partial \mathbf{C}} = \mathbf{a}^0 \otimes \mathbf{a}^0;\ \frac{\partial I_5}{\partial \mathbf{C}} = \mathbf{a}^0 \otimes \mathbf{C} \cdot \mathbf{a}^0 + \mathbf{a}^0 \cdot \mathbf{C} \otimes \mathbf{a}^0$$

where $\otimes$ represents the tensor outer product.

The corresponding second Piola-Kirchhoff stress $\mathbf{S}$ can be expressed by

$$\mathbf{S} = 2\left[\frac{\partial \Psi}{\partial I_1}\mathbf{I} + \frac{\partial \Psi}{\partial I_2}(I_1\mathbf{I} - \mathbf{C}) + \frac{\partial \Psi}{\partial I_3}(I_2\mathbf{I} - I_1\mathbf{C} + \mathbf{C}^2) + \frac{\partial \Psi}{\partial I_4}(\mathbf{a}^0 \otimes \mathbf{a}^0) + \frac{\partial \Psi}{\partial I_5}(\mathbf{a}^0 \otimes \mathbf{C} \cdot \mathbf{a}^0 + \mathbf{a}^0 \cdot \mathbf{C} \otimes \mathbf{a}^0)\right] \tag{5.28}$$

5.2.4 Viscoelasticity

Biological soft tissues exhibit time-dependent mechanical behaviours which are often referred to as viscoelastic behaviours [112]. In the proposed method, a time-dependent strain energy density function $\widehat{\Psi}$ [70] is adopted to

simulate the viscoelastic behaviours of soft tissues. The time-dependent strain energy density function is expressed in the form of a convolution integral, i.e.

$$\widehat{\Psi} = \int_0^t \alpha(t-s)\frac{\partial \Psi}{\partial s}\, ds \tag{5.29}$$

where t is time and $\alpha(t)$ is a relaxation function expressed in terms of a Prony series, i.e. $\alpha(t) = \alpha_\infty + \sum_{i=1}^{N} \alpha_i e^{-t/\tau_i}$ with positive constants α_∞, α_i and τ_i. By imposing condition $\alpha_\infty + \sum_{i=1}^{N} \alpha_i = 1$, $\alpha(t)$ can be further written as

$$\alpha(t) = 1 - \sum_{i=1}^{N} \alpha_i\left(1 - e^{-t/\tau_i}\right). \tag{5.30}$$

Accordingly, the second Piola-Kirchhoff stress $\mathbf{S}$ is modified as

$$\hat{\mathbf{S}} = 2\frac{\partial \widehat{\Psi}}{\partial \mathbf{C}} = \int_0^t \alpha(t-s)\frac{\partial \mathbf{S}}{\partial s}\, ds = \int_0^t \left[1 - \sum_{i=1}^{N} \alpha_i\left(1 - e^{(s-t)/\tau_i}\right)\right]\frac{\partial \mathbf{S}}{\partial s}\, ds = \mathbf{S} - \sum_{i=1}^{N} \boldsymbol{\gamma}_i \tag{5.31}$$

where $\boldsymbol{\gamma}_i$ is a time-dependent term given by

$$\boldsymbol{\gamma}_i = \int_0^t \alpha_i\left(1 - e^{(s-t)/\tau_i}\right)\frac{\partial \mathbf{S}}{\partial s}\, ds \tag{5.32}$$

Eq. (5.32) can be converted into an incremental update ${\boldsymbol{\gamma}_i}^t = A_i \mathbf{S}^t + B_i {\boldsymbol{\gamma}_i}^{t-\Delta t}$ applied at each time step Δt with constant coefficients A_i and B_i determined by $A_i = \frac{\Delta t \alpha_i}{(\Delta t + \tau_i)}$ and $B_i = \frac{\tau_i}{(\Delta t + \tau_i)}$.

5.2.5 Material Models

In our simulation, two isotropic and one anisotropic constitutive models are developed and integrated with the proposed EBM. They are the Saint Venant-Kirchhoff model, Neo-Hookean model and anisotropic Neo-Hookean model. The viscoelasticity can be incorporated into each model by employing the time-dependent strain energy density function and associated second Piola-Kirchhoff stress given by Eqs. (5.29) and (5.31), respectively.

5.2.5.1 Saint Venant-Kirchhoff Model

The strain energy density function of the Saint Venant-Kirchhoff model is expressed by

$$\Psi = \frac{\lambda}{2}[\mathrm{tr}(\mathbf{E})]^2 + \mu \mathrm{tr}(\mathbf{E}^2) \tag{5.33}$$

where λ and μ are the Lamé coefficients, which can be expressed by the Young's modulus E and Poisson's ratio v as $\lambda = \frac{Ev}{(1+v)(1-2v)}$ and $\mu = \frac{E}{2(1+v)}$.

The second Piola-Kirchhoff stress $\mathbf{S}$ is expressed by

$$\mathbf{S} = \lambda\, \mathrm{tr}(\mathbf{E})\mathbf{I} + 2\mu\mathbf{E}\,. \tag{5.34}$$

5.2.5.2 Neo-Hookean Model

The strain energy density function of the compressible Neo-Hookean model [73] is expressed by

$$\Psi = \frac{\mu}{2}(\bar{I}_1 - 3) + \frac{\kappa}{2}(J-1)^2 \tag{5.35}$$

where κ is the bulk modulus, which can be expressed by the Young's modulus E and Poisson's ratio v as $\kappa = \frac{E}{3(1-2v)}$.

The second Piola-Kirchhoff stress $\mathbf{S}$ is expressed by

$$\mathbf{S} = \mu J^{-2/3}\mathbf{I} + \left(-\frac{1}{3}\mu J^{-2/3} I_1 + \kappa J(J-1)\right)\mathbf{C}^{-1}\,. \tag{5.36}$$

5.2.5.3 Anisotropic Neo-Hookean Model

The strain energy density function of the Neo-Hookean model is modified to account for the anisotropy introduced by the preferred local fibre direction. The modified strain energy density function for the anisotropic Neo-Hookean model is written as

$$\Psi = \frac{\mu}{2}(\bar{I}_1 - 3) + \frac{\eta}{2}(\bar{I}_4 - 1)^2 + \frac{\kappa}{2}(J-1)^2 \tag{5.37}$$

where η is a material parameter with the unit of Pa, and it is set to $\eta = 2\mu$ according to [70]; and $\overline{I_4}$ is related to I_4 by $\overline{I_4} = J^{-2/3} I_4$. For simplicity and as a common practical feature of anisotropic models for soft tissues [70], only $\overline{I_4}$ is considered in the anisotropic Neo-Hookean model while $\overline{I_5}$ is omitted.

The second Piola-Kirchhoff stress $\mathbf{S}$ corresponding to the anisotropic Neo-Hookean model can be expressed by

$$\mathbf{S} = \mu J^{-2/3}\mathbf{I} + \left(-\frac{1}{3}\mu J^{-2/3} I_1 + \kappa J(J-1)\right)\mathbf{C^{-1}} + J^{-2/3}\eta(\overline{I_4} - 1)\left(\mathbf{A}^0 + \frac{I_4}{3}\mathbf{C^{-1}}\right) \tag{5.38}$$

where $\mathbf{A}^0 = \mathbf{a}^0 \otimes \mathbf{a}^0$.

5.3 Results and Discussion

A prototype surgical simulation system has been implemented with the proposed EBM for soft tissue deformation. Simulations, experiments, and comparison analysis have been conducted to investigate the performance of the proposed method in terms of the following aspects: (i) the work-energy balance effect; (ii) compression, extension and shear tests in comparison with the simulations using a commercial package of finite element analysis; (ii) anisotropic deformation and the effect of viscoelasticity; and (iii) the computational performance and human organ deformation with haptic feedback.

5.3.1 Verification of Work-Energy Balance

To demonstrate the work-energy balance for the equilibrium state of object deformation, let us consider the deformation of a beam under an external tensile force. The beam is 2 m in length with a square cross-section of 0.2 m x 0.2 m, and it is modelled by an isotropic Neo-Hookean material model. The mass density of 1,000 kg/m^3, Young's modulus E = 3,000 Pa and Poisson's ratio v = 0.49, which reflect the mechanical properties of human brain [56], were used for the simulation. The beam was constrained at the left-side face, while the entire right-side face was subject to a tensile force of 0.8 N in the positive x direction. As illustrated in Fig. 5.2, the work done by the tensile force is supplied to the beam from its right-side face. The work is balanced iteratively against the strain energy due to the internal force to find the new equilibrium state of the beam. After 2,000 iterations, the relative energy difference (RED) is nearly zero, which means the equilibrium state is reached.

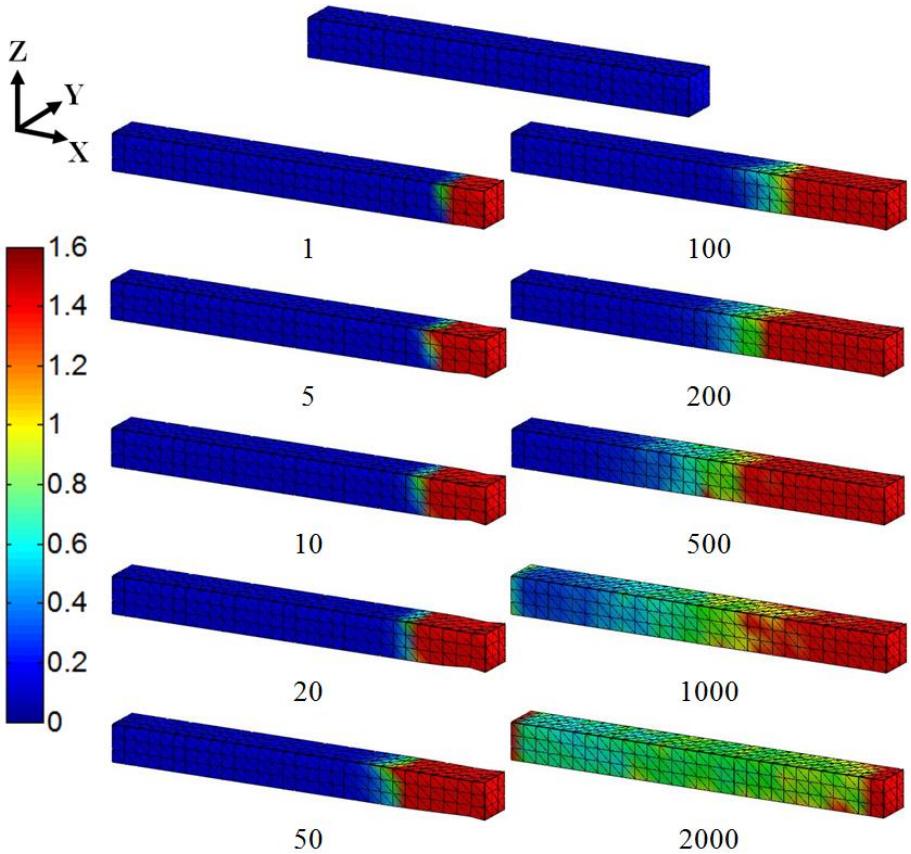

Figure 5.2 Strain energy of a beam, where the left-side face of the beam is constrained while a tensile force in the positive *x* direction is applied to the entire right-side face: the top image (in full blue colour) shows the rest state of the beam; the rest images show the strain energy distributions (coloured) at iterations 1, 5, 10, 20, 50, 100, 200, 500, 1,000 and 2,000; the beam reaches the equilibrium state after 2,000 iterations.

As mentioned previously, since the soft tissue model is made up of a number of finite elements, it leads to an iterative process to achieve work-energy balance for the entire soft tissue model. Fig. 5.3 illustrates the work-energy balance effect during the iterative solution process. It can be seen from Fig. 5.3(a) that the initial difference between the work done by the external force and strain energy due to internal force is around 23 J where only the effect of the external force is considered. The energy difference is subsequently reduced via the iterative position-based incremental process to achieve work-energy balance, i.e. zero difference. Fig. 5.3(c) shows a detailed view of Fig. 5.3(a), with a particular focus on the first 100 iterations. It can be seen that the energy difference is reduced substantially within the initial small number of iterations and then gradually converges to zero. Fig. 5.3(b) and (d) illustrate the RED for the total 2,000 iterations and first 100 iterations, respectively. It can be seen that the energy difference drops drastically at the initial stage, leading to 7.0% RED

at 20 iterations. However, after 20 iterations, the decrease of energy difference becomes slow, leading to only 2.5% RED at 100 iterations achieved at the cost of 80 more iterations. Further, Fig. 5.4 illustrates the maximum error for displacement u_x in the x direction by the proposed method with reference to ABAQUS (Version 6.14-1) finite element analysis. The maximum displacement error is 0.00532 m (9.112%) at 20 iterations and 0.00169 m (2.892%) at 100 iterations. These demonstrate the condition of energy balance can be satisfied at a high level of accuracy with a certain number of iterations, but further improvement of accuracy is limited at a large cost of numerical iterations. Therefore, an appropriate number of iterations can be selected to achieve a balance between numerical accuracy and computational performance for surgical simulation. In order to further analyse the condition of energy balance, the number of iterations was selected as 20 in the following simulations, where the results further verify the above conclusion.

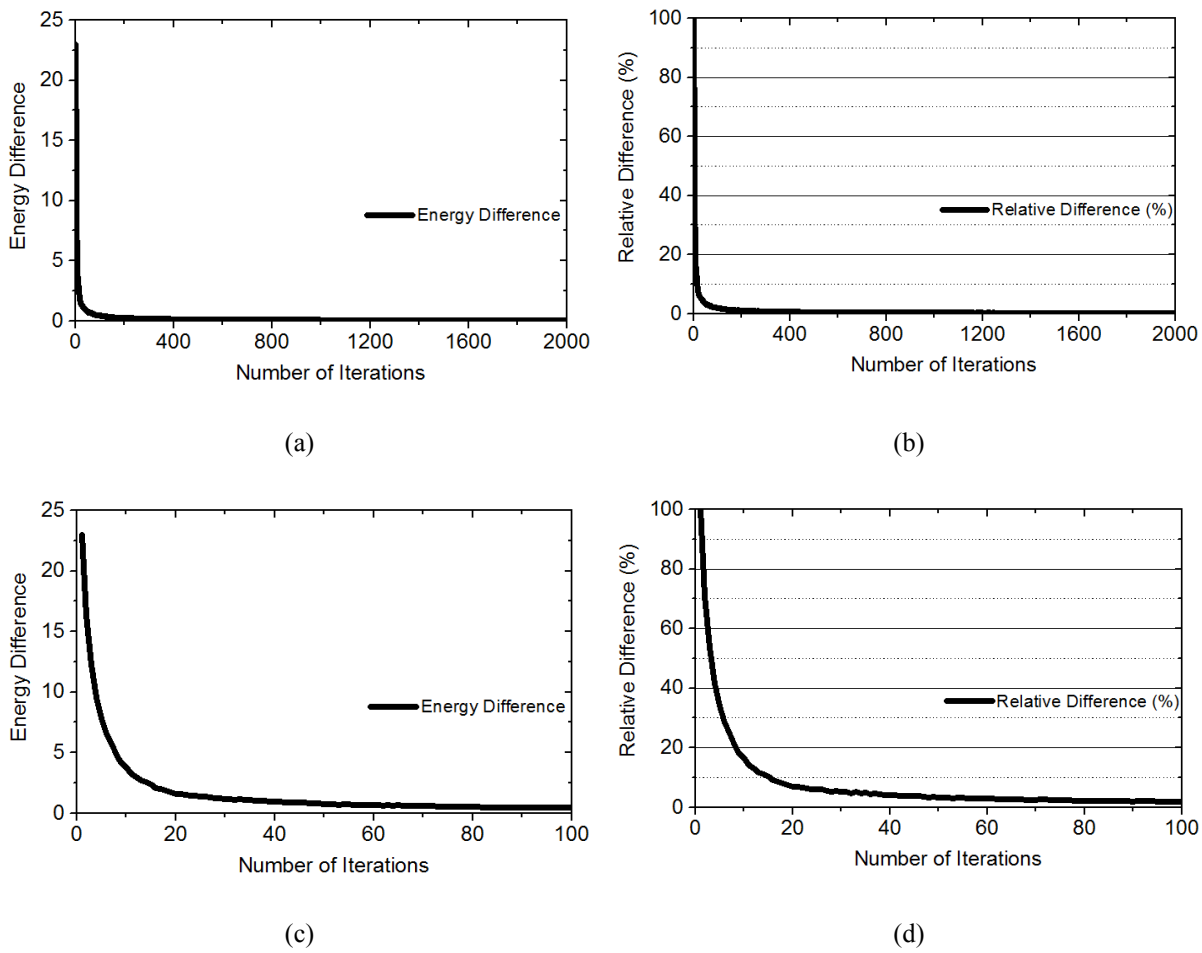

Figure 5.3 Energy difference between the strain energy and external work with respect to the number of iterations: (a) energy difference for the total 2,000 iterations; (b) relative difference for the total 2,000 iterations; (c) a detail view of (a) for the first 100 iterations; and (d) a detail view of (b) for the first 100 iterations.

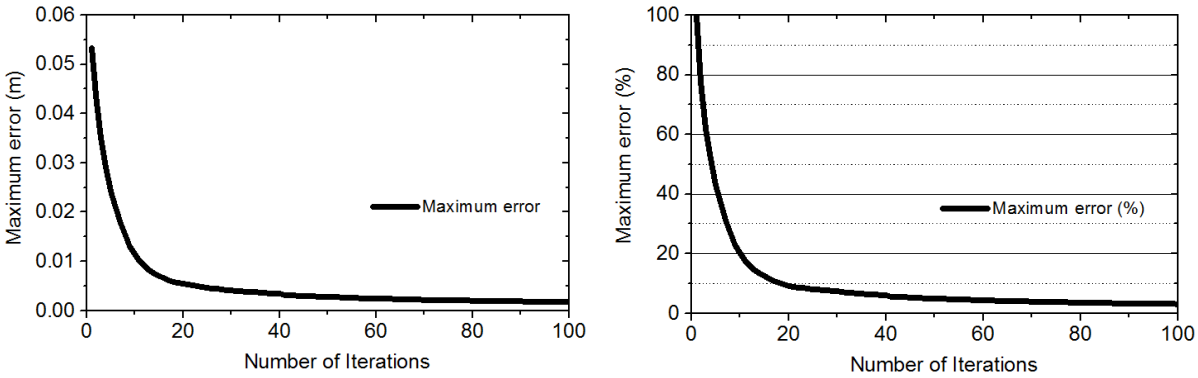

(a) (b)

Figure 5.4 Maximum errors for displacement u_x in the x direction by the proposed EBM: (a) in displacement; and (b) in percentage.

5.3.2 Compression, Extension and Shear Deformations

The proposed EBM is verified by comparing the compression, extension and shear deformations against those obtained using ABAQUS finite element analysis package. A Neo-Hookean model with a mass density of 1,000 kg/m^3, Young's modulus E = 3,000 Pa and Poisson's ratio v = 0.49 were used for all cases. The parameters C10 and D1 used in the ABAQUS to define the Neo-Hookean model were calculated from the Young's modulus E and Poisson's ratio v. Figs. 5.5 and 5.6 illustrate the compression and extension deformations of a cylinder. The cylinder is 2 m in length with radius of 0.5 m at the rest state. It is deformed by constraining the left-side face while moving the entire right-side face 0.4 m in the negative z direction in Fig. 5.5 and positive z direction in Fig. 5.6. The comparisons with ABAQUS results in terms of displacements at nodes on the red line are illustrated in Figs. 5.5(c) and 5.6(c), where the red line is the intersection between the XZ plane and cylindrical face, and the coordinate system is located at the centre point of cylinder's left-side face. The resultant RED is 4.6% for the compression deformation and 4.5% for the extension deformation. The maximum error, mean error and root mean square error (RMSE) are 0.00388 m (7.721%), 0.00206 m (3.539%) and 0.00232 m (4.152%) for the compression deformation, and 0.00202 m (7.766%), 0.00104 m (2.439%) and 0.00119 m (3.054%) for the extension deformation.

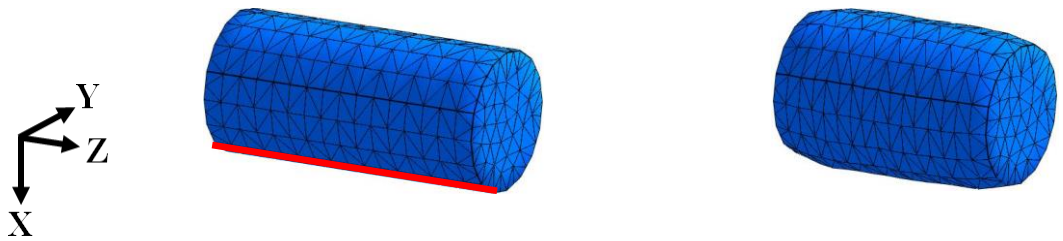

(a) (b)

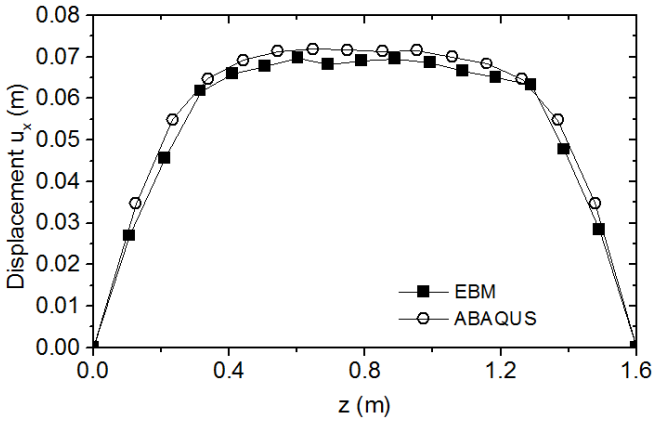

(c)

Figure 5.5 Compression of a cylinder: (a) undeformed state, where the intersection line between XZ plane with cylindrical face is highlighted in red; (b) deformed state; and (c) comparison with ABAQUS results in terms of displacement u_x in the *x* direction at the nodes on the red line highlighted in (a).

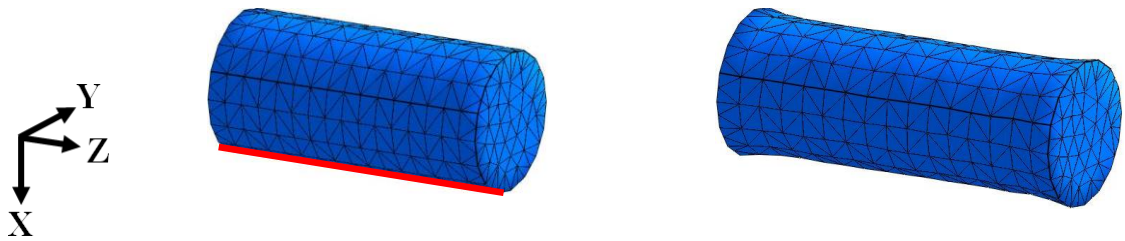

(a) (b)

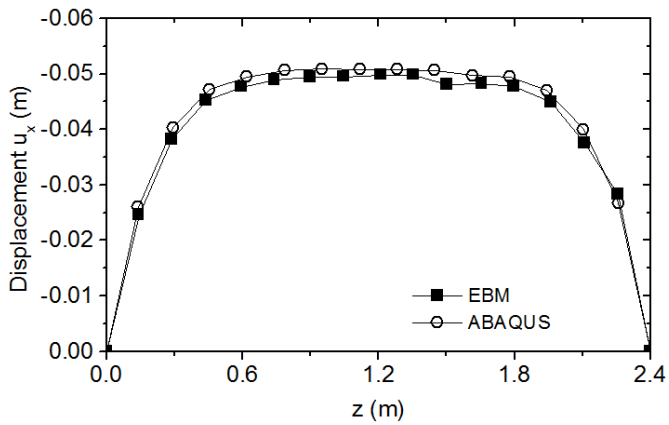

(c)

Figure 5.6 Extension of a cylinder: (a) undeformed state, where the intersection line between XZ plane with cylindrical face is highlighted in red; (b) deformed state; and (c) comparison with ABAQUS results in terms of displacement u_x in the *x* direction at the nodes on the red line highlighted in (a).

Fig. 5.7 illustrates the shear deformation of a cube. The cube is 2 m in length, width, and height. It is deformed by constraining the bottom face while moving the entire top face 0.5 m in the positive *z* direction. The comparison with ABAQUS results in terms of displacements at nodes on the red line is shown in Fig. 5.7(c), where the red line is the intersection between the plane $y = 1$ m and the right face of the cube, and the coordinate system is located at the intersection point of the bottom, left and back faces. The resultant RED is 7.4%. The maximum error, mean error and RMSE are 0.01464 m (7.945%), 0.00847 m (3.825%) and 0.00976 m (4.603%), respectively.

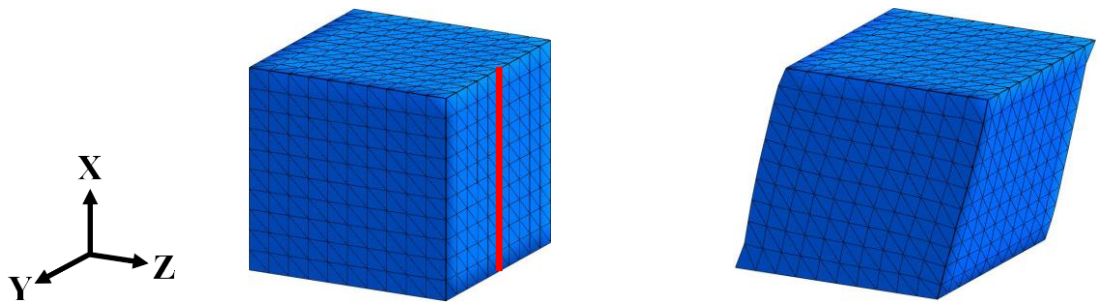

(a) (b)

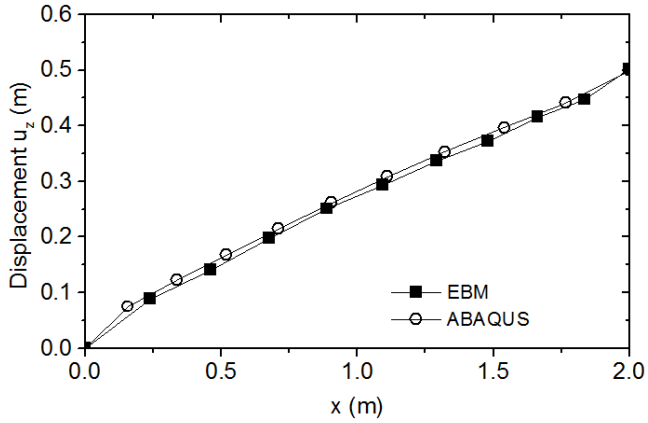

(c)

Figure 5.7 Shear deformation of a cube: (a) undeformed state, where the intersection line between plane $y = 1$ m and right face of the cube is highlighted in red; (b) deformed state; and (c) comparison with ABAQUS results in terms of displacement u_z in the z direction at the nodes on the red line highlighted in (a).

It can be seen from Figs. 5.5(c), 5.6(c) and 5.7(c) that the deformations obtained from the proposed EBM are in good agreement with those obtained from ABAQUS finite element analysis.

5.3.3 Anisotropic Deformation

As mentioned in Chapter 5.2.3, anisotropic deformation can be achieved via a preferred local fibre direction $\mathbf{a}^0$. To demonstrate anisotropic deformation, let us consider the deformation of a cubic model with the preferred local fibre direction $\mathbf{a}^0 = [0 \quad 0 \quad 1]$ using the anisotropic Neo-Hookean model. The cube is 2 m in length, width, and height, with a mass density of 1,000 kg/m^3, Young's modulus E = 3,000 Pa and Poisson's ratio v =

0.49. It is deformed by constraining the bottom face while moving the entire top face 0.3 m in both positive and negative x directions to extend and compress the cube. Fig. 5.8 shows the comparison of deformations between the isotropic and anisotropic models, where REDs are 7.3% and 7.4% for the isotropic extension and compression, respectively, whereas REDs are 7.5% and 7.6% for anisotropic extension and compression, respectively. With no preferred fibre direction in the isotropic model ($\eta = 0$), the expansion and contraction in the y and z directions are uniform as shown in Figs. 5.8(a) and 5.8(c), respectively. In Figs. 5.8(b) and 5.8(d), by setting the local fibre direction in the anisotropic model as $\mathbf{a}^0 = [0 \quad 0 \quad 1]$, which leads to an increase in stiffness in the z direction, the expansion and contraction in the z direction become much smaller, while in the y direction become larger than the isotropic deformation (see the green and red regions in Figs. 5.8(b) and 5.8(d)).

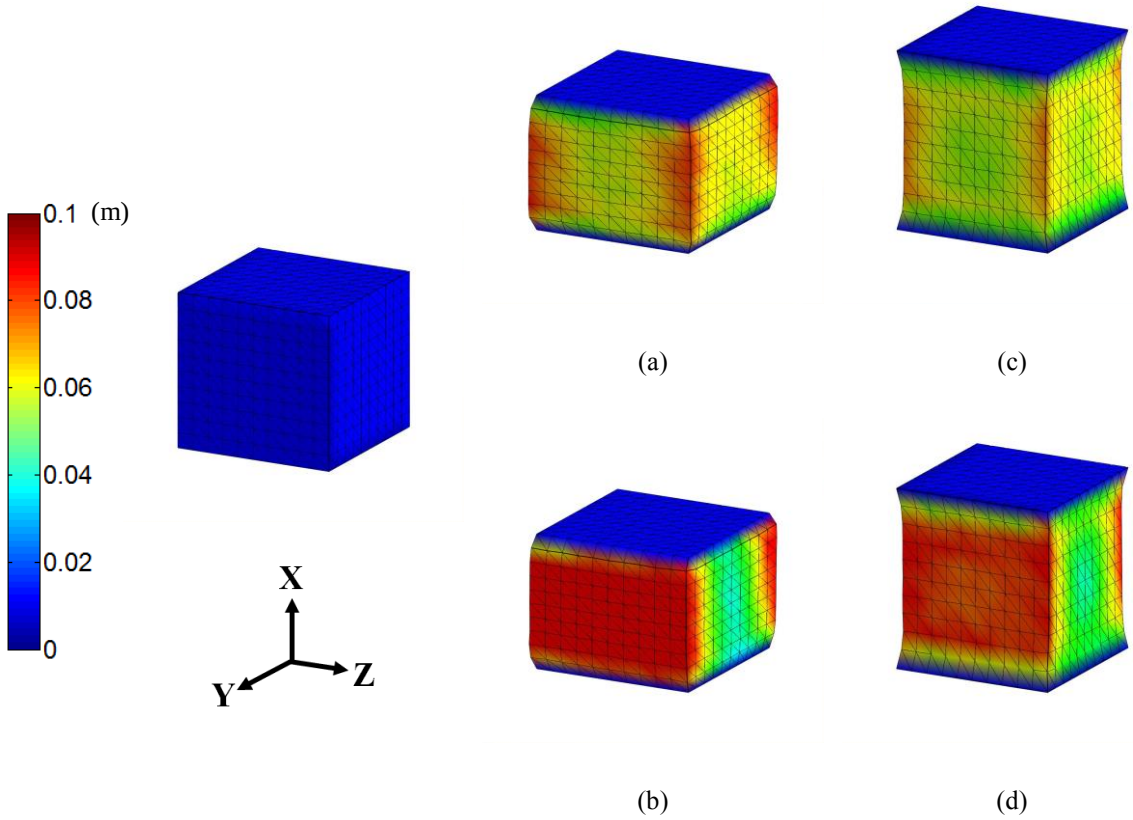

Figure 5.8 Comparison of isotropic and anisotropic deformations: (a) compressed isotropic model; (b) compressed anisotropic model with preferred local fibre direction $\mathbf{a}^0 = [0 \quad 0 \quad 1]$; (c) extended isotropic model; (d) extended anisotropic model with preferred local fibre direction $\mathbf{a}^0 = [0 \quad 0 \quad 1]$. Colour maps indicate the relative magnitude of displacement $\left({u_y}^2 + {u_z}^2\right)^{1/2}$.

5.3.4 Viscoelastic Effect

The viscoelastic behaviours of soft tissues can also be achieved by the proposed EBM via the time-dependent strain energy density function discussed in Chapter 5.2.4. To demonstrate the viscoelasticity effect simulated by the proposed EBM, a single Prony series term was selected for simplicity and set with parameters $\alpha_1 = 0.5$ and $\tau_1 = 0.58$ [70]. A material of cubic shape with the same dimensions as that in Chapter 5.3.3 is deformed by a test protocol of stress-relaxation type. The bottom face of the cube is constrained while compressing the entire top face in the negative x direction for 0.5 s by a displacement of 0.3 m and further holding at the displacement for 4.5 s. It can be seen from Fig. 5.9 that the reaction forces at the bottom face show a distinct delay resulting from stress relaxation. This response is similar to the tissue relaxation observed from living tissues [112]. It is also observed that the increased stiffness in the anisotropic model results in greater reaction forces than the isotropic model. The resultant RED is 7.4% for isotropic and 7.6% for anisotropic model.

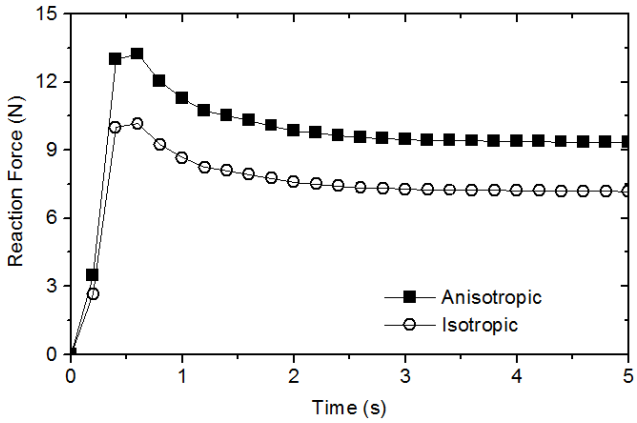

Figure 5.9 Reaction forces at the bottom face of the cube over time: the simulated reaction forces show a distinct delay, which is similar to the tissue relaxation observed from living tissues.

5.3.5 Soft Tissue Deformation with Haptic Feedback

The proposed EBM is integrated with a PHANToM haptic device from Geomagic for interactive soft tissue deformation with haptic feedback. Users can deform a virtual human organ model via the virtual haptic probe. The organ deformation and associated internal forces are calculated by the proposed EBM. Subsequently, the internal forces are output to the PHANToM device for haptic feedback, and the calculated deformation is rendered on the monitor for visual feedback. Fig. 5.10 shows an interactive deformation of a virtual volumetric human liver model with haptic feedback.

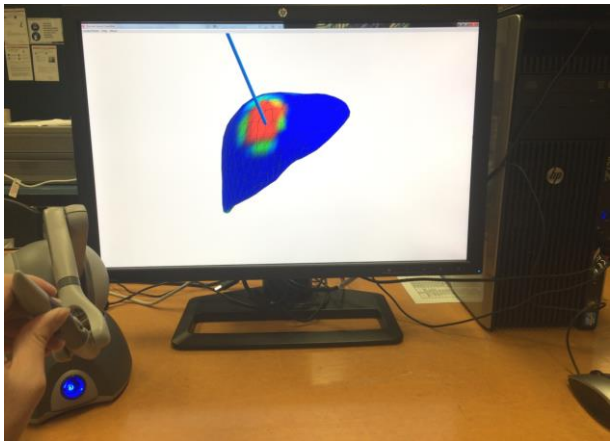

Figure 5.10 Interactive deformation of a virtual human liver model via the haptic probe.

The virtual human liver model is discretised into a tetrahedral mesh consisting of 1,106 nodes and 5,096 tetrahedrons using the open-source mesh generator 'TetGen' with built-in mesh quality control functions [144]. However, a four-node linear tetrahedral element can be stiff, known as volumetric locking, for nearly incompressible materials such as soft tissues. To address this issue, the tetrahedral mesh was further improved by averaging a volumetric element over adjacent nodes [71]. The liver model is modelled using the Neo-Hookean material with a mass density of 1,060 kg/m^3, Young's modulus E = 3,500 Pa and Poisson's ratio v = 0.49, which approximate the mechanical properties of human liver [8, 118]. The virtual liver model is constrained at the lower-left region with both pulling-up and dragging-down forces applied to the upper-right and bottom-right regions, respectively, to deform the liver away from its natural state. Fig. 5.11 shows deformations of the virtual human liver model and the associated strain energy distributions. The resultant RED is 6.2%.

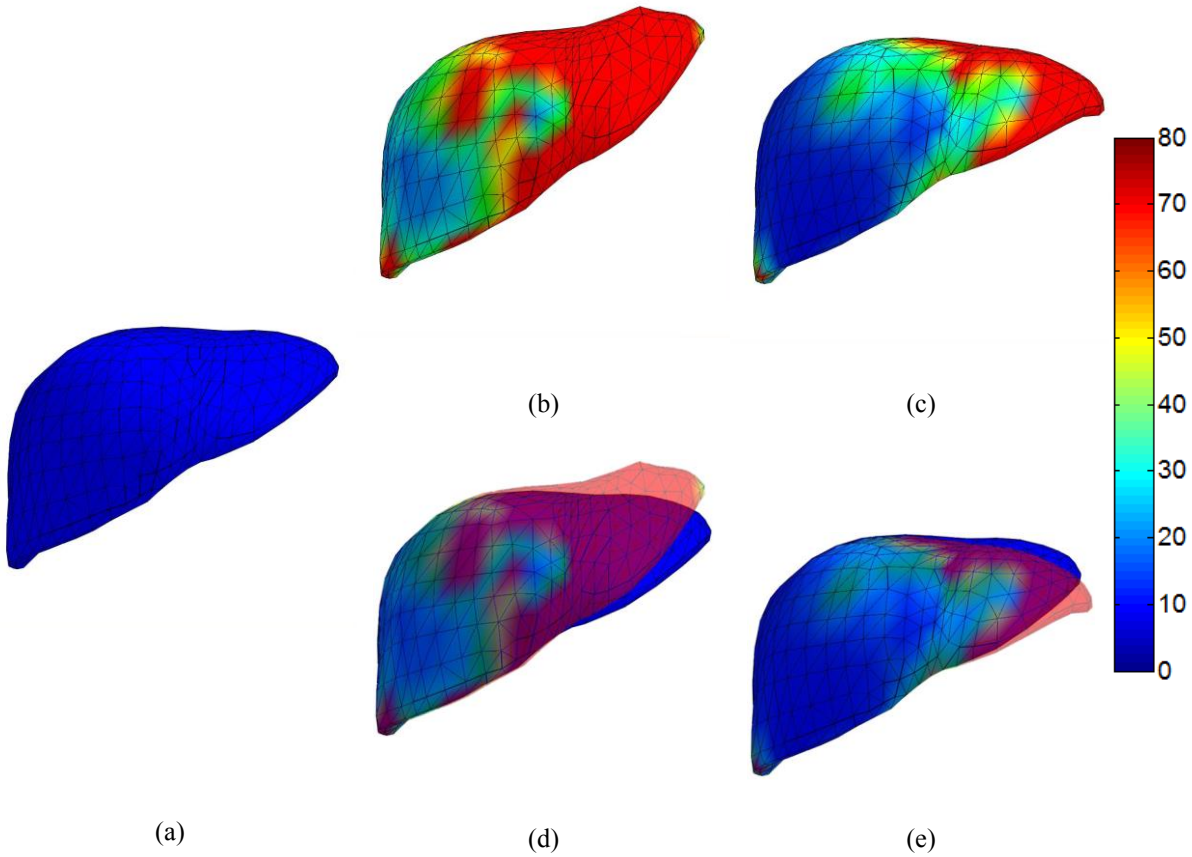

Figure 5.11 Deformations of a virtual human liver model and their associated strain energy distributions: (a) undeformed state; (b) deformed state of the liver with pulling-up forces applied to the upper-right region; (c) deformed state of the liver with dragging-down forces applied to the bottom-right region; (d) and (e) comparisons of the deformed states in (b) and (c) with the undeformed state in (a), respectively.

5.3.6 Computational Performance

The proposed EBM is programmed in C++ and evaluated on an Intel(R) Core(TM) i7-4770 CPU@3.40 GHz and 8 GB RAM memory PC. The CPU solution time utilising different numbers of tetrahedrons is illustrated in Fig. 5.12. From Fig. 5.12, it can be seen that the computational time is almost linear with the number of tetrahedrons. The solution time of the anisotropic model is slightly higher than that of the isotropic model due to the computation of additional terms in the strain energy density function and second Piola-Kirchhoff stress of the anisotropic model. It is also noticed that the update of time-dependent term $\boldsymbol{\gamma}$ for viscoelasticity further contributes 1 ms to the total computational time at each time step. The computational performance can be further improved by multi-core CPU implementation, GPU acceleration [73, 75] or adaptive technique [140].

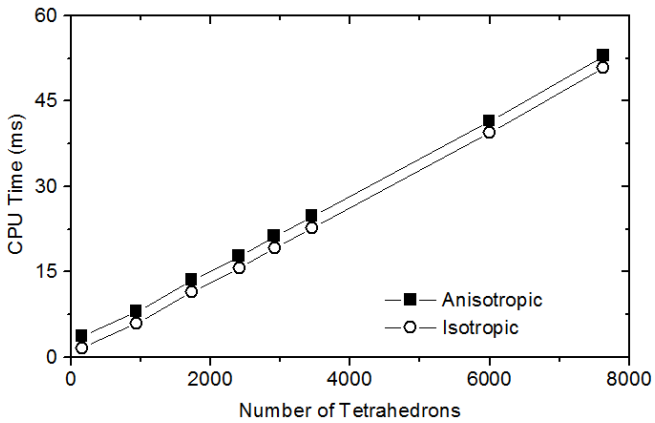

Figure 5.12 Computational performance: CPU solution time for isotropic and anisotropic models.

The PHANToM haptic device requires forces to be updated at the rate of at least 1,000 Hz for realistic force feedback. As it can be seen from Fig. 5.13, the force update rate is above 1,000 Hz when the number of tetrahedrons is around 500 in the case of the isotropic material and 200 in the case of the anisotropic material. The number of tetrahedrons in the case of the anisotropic model is slightly less than that of the isotropic model due to the computation of additional terms in the strain energy density function and second Piola-Kirchhoff stress of the anisotropic model. When the computational speed cannot meet the haptic refresh update requirement, force extrapolation [120] was employed to improve the realism of haptic feedback by generating missing forces from the previous calculation loop.

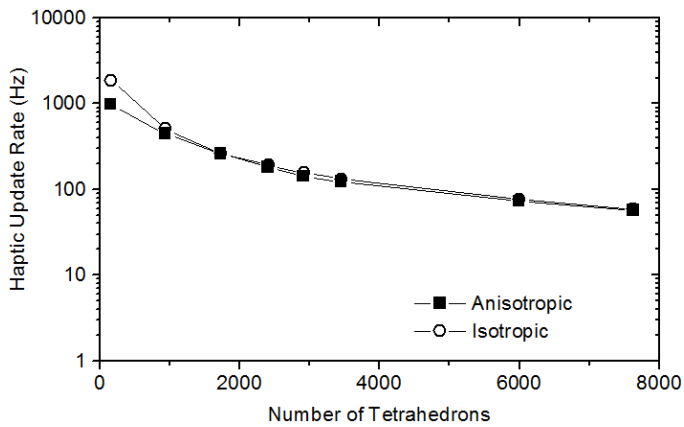

Figure 5.13 Haptic performance: haptic update rate of 1,000 Hz for realistic force feedback is achieved with around 500 tetrahedrons in the case of the isotropic material and 200 in the case of the anisotropic material.

5.4 Remarks

The proposed EBM provides a new means for modelling of soft tissue deformation for surgical simulation. Compared to MSM, ChainMail algorithm and position-based dynamics approach with shape matching, the proposed EBM is based on the continuum mechanics of elasticity to describe deformation of soft tissues, capable of accommodating both geometric and material nonlinearities involved in soft tissue deformation. The anisotropy and viscoelasticity can be easily incorporated in the proposed EBM via the constitutive laws, whereas it is difficult to achieve such incorporation by MSM, ChainMail and position-based dynamics approach. Compared to BEM, the proposed EBM can also exhibit anisotropic and viscoelastic behaviours of soft tissues. Compared to FEM based on linear elasticity and geometric nonlinear TMM, the proposed EBM can achieve both geometric and material nonlinearities. Compared to FEM based on model reduction [80, 145], the proposed EBM does not require offline pre-computation. Further, it accounts for full system energy for work-energy balance, whereas the model reduction technique involves a projection from the full system space into a smaller subspace, leading to a loss of system energy. The proposed EBM also preserves system energy via work-energy balance.

6. Discussion

This thesis presents three new methodologies, namely the new ChainMail algorithms, energy propagation method, and energy balance method, for modelling of soft tissue deformation in surgical simulation. The proposed ChainMail algorithms improve the traditional ChainMails by accommodating various material properties, conserving volume and strain energy, conserving linear and angular momentums, and enhancing computational performance. Energy propagation method provides a new perspective for conducting soft tissue deformation, i.e., it considers soft tissue deformation as a process of energy propagation; nonlinear material properties are accommodated via the nonlinear energy propagation and modification of parameter coefficients. Energy balance method conducts soft tissue deformation from the perspective of energy conservation, and it can accommodate fast simulation of geometric and material nonlinearities. Among the three new methodologies, the choice of a suitable methodology for soft tissue deformation depends on the situation of surgical simulation developed. ChainMail algorithms exhibit higher solution speed to soft tissue deformation but are achieved at the cost of physical accuracy. They are well capable for modelling deformation of medical volumes containing large data sets. Energy propagation method and Energy balance method, on the other hand, are more suitable for soft tissue deformation where physical accuracy is concerned. Since it does not require pre-computation, Energy propagation method may be employed where topology changes are encountered. Energy balance method is more suitable for generic surgical simulation and clinical analysis where conservation of energy is considered.

Topology changes due to surgical operations such as cutting and tearing is a requirement in surgical simulation that further complicates deformable modelling. These operations are difficult to achieve within the constraint of real-time performance as topology changes, often involve mesh and surface reconstruction, need to be calculated and updated. In ChainMail algorithms, topology changes can be accommodated by removing the chain links that are encountered along the path of the cutting tool as it passes through soft tissues [42]. In energy propagation method, topology changes can be accommodated by identifying the break point to break an edge using a threshold value of energy; subsequently, new points will be introduced according to the transition of energy to form new control volumes and boundaries to achieve optimal energy distribution. In energy balance method, topology changes can be accommodated by removing or splitting finite elements or employing extended FEM (X-FEM) technique. For a thorough discussion, readers are referred to the survey [163] on topic of physically-based simulation of cuts in deformable models.

Overall, among various deformable models proposed for modelling of soft tissue deformation, it is obvious that there is no single deformable model that can address the realistic and real-time surgical simulation. Instead, they are developed in different ways to meet specific needs. Despite the computational advantage of the geometrically-based models, these models are seldom or no longer used for soft tissue deformation due to their non-physics-based nature. MSM is often used when computational efficiency is preferred to model accuracy,

and it has been used in many commercially available surgical simulators [146, 147]. However, a more accurate model is needed in order to be compatible with clinical use, provided the added computational complexity is acceptable. In addition, the optimisation process in MSM is a time-consuming task and may lead to failure if the prior assumed condition is changed. The ChainMail algorithm is well suited to the modelling of interactive deformation of large medical volumes, where other deformation models cannot achieve real-time computational performance. The shape matching approach can be used for stable simulation of soft tissue deformation, thanks to its unconditional stability [47]. It needs to be noted that these models generally exhibit difficulties in determination of model parameters to be associated with constitutive laws governing the mechanical behaviours of soft tissues, and hence they can only produce a physically plausible simulation.

Higher model accuracy can be achieved by the continuum-based approach despite the increased computational complexity. FEM is often employed if physical accuracy is concerned. Most simplifications made to FEM to facilitate its computational performance inevitably compromise its model accuracy and limit its capability in handling various material properties. Although real-time computational performance can be achieved with the total Lagrangian-based FEMs, they are generally only suitable for the modelling of soft tissue response that does not involve topology changes, such as surgical cutting and tearing. The results of pre-computation at the initial configuration would become invalid when a topology-changing cut is introduced to the system. Model reduction is a promising technique for real-time simulation of soft tissue deformation; however, most of the models developed using this scheme require an offline and an online computation, which may pose challenges at simulation of topological changes. Despite recent progress [145] in the framework of model reduction that topological changes are handled by X-FEM for the incorporation of discontinuities in the displacement field, the offline computation generally assumes a certain model behaviour that may lead to inaccuracy if the model is changed during online simulation. In addition, it is also important to consider the element-related issues when using mesh-based methods due to the use of low-order finite elements. The hourglass control algorithm and locking-free tetrahedrons should be used to mitigate numerical inaccuracies. When simulating large deformation and discontinuities in soft tissue deformation, the meshless methods are often preferred to the mesh-based methods, since they can conduct deformation without explicit construction of nodal connectivity which can avoid most of the element-related issues, such as element distortion and element inversion. Meanwhile, it also avoids the process of mesh generation, facilitating the clinical integration of the computer-assisted surgery [96]. However, the accuracy of the meshless methods is heavily dependent on the distribution of particles in the problem domain, and it is only accurate in terms of global reaction force but not so for local reaction force.

The emerging of neural network approach and machine learning could also perform an important position in realistic and real-time surgical simulation. The continuum-mechanical models generally consider the soft tissues as a continuum medium whose behaviours are governed by constitutive laws expressed by PDEs. Despite the high accuracy achieved by the continuum-based methods, it is arguably that soft tissues are more complex than

idealised continuum models, both in material compositions and structure formations. The machine learning technique, on the other hand, seeks for a mapping function through training of a supervised neural network to generate an output (deformation) for future unseen inputs (prescribed displacements). The soft tissue mechanical behaviours are encoded implicitly in the trained coefficients of the nerual network. Owing to the recent advancement in artificial intelligence and open-source package such as the TensorFlow [148], many different soft tissues can be employed for the training of nerual networks. However, it needs to be noted that the simulated results are highly dependent on the learning algorithm chosen.

Table 1. Comparison of main categories of deformable models

Deformable model	Accuracy	Speed	Remark
Geometrically-based	*	****	Lack of deformable physics
MSM	***	****	Generic simulation, such as surgical training
ChainMail	*	*****	Large medical volumes
FEM	*****	***	Good for scientific analysis
Meshless method	****	***	Large deformation and discontinuities
Machine learning	****	****	Rely on training samples and learning algorithms
Data-driven	****	****	Require patient-specific data

Scheme: * is the lowest whereas ***** is the highest.

Given the wide varieties and variations of deformable models for surgical simulation, Table 1 summaries the capabilities of the aforementioned approaches in terms of physical accuracy and computational performance. It can be used as reference to make up an appropriate deformation strategy according to different surgical simulation conditions.

To verify the physical accuracy of the deformable models for surgical simulation, most models compared their deformation solutions with those of the FEM reference solutions, such as the solution of conmerically available ABAQUS [149] using implicit solver with hybrid formulation of linear elements [85]. However, given that finite element modelling is an approximation method in itself, the accuracy of its results heavily relies upon the quality of its input [5]. Kerdok *et al.* [5] presented a Truth Cube which set the practical physical standards for validation of real-time soft tissue deformation models. A cube of silicone rubber with a pattern of embedded Teflon spheres is undergone uniaxial compression and spherical indentation tests, and the cube is scanned by a

CT scanner (see Fig. 6.1). The volumetric displacement results, along with details of the cube construction and boundary conditions in the two loading tests served as the physical standard for model validation. Despite the available data for validation, it needs to be noted that the Truth Cube has a regular geometry and well-characterised material properties and loading conditions, but the surgical simulation needs to handle with conditions that are vastly different, involving large deformation, irregular shapes and complex materials.

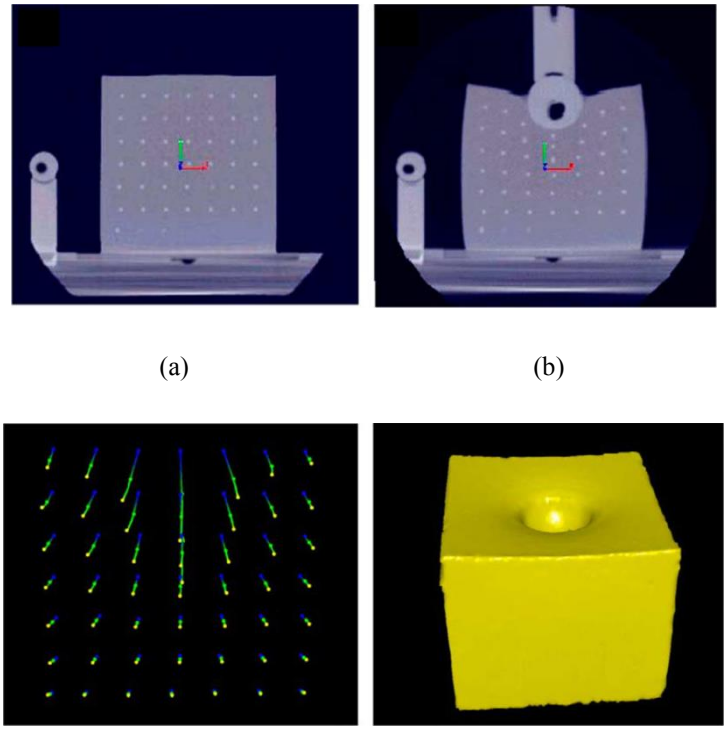

(a) (b)

(c) (d)

Figure 6.1 (a) A CT scan of a centre vertical slice for spherical indentation in undeformed, initial configuration; (b) deformation of the cube under 30% nominal strain; (c) the trajectory and locations of the internal spheres where blue represents no indentation, green represents 22% nominal strain case, and yellow represents 30% nominal strain case; and (d) the surface for the 30% strain case.

To be compatible with clinical use, the deformable models must use patient-specific properties of tissues; however, they are significant difficult to determine for human tissues. The first reason is the evident difficulty in carrying out quantitative empirical measurements of human tissues (such as liver) *in vivo*. Second, there are always uncertainties in patient-specific properties of tissues since the mechanical properties of soft tissues obtained through *in vivo* and *in situ* measurements are different than the similar properties obtained through *in vitro* measurements [150]. However, despite these reasons, it is still possible to determine deformation of soft

tissues during surgery without the knowledge of patient-specific properties of tissues. As evident in [151], the computational biomechanics problems can be reformulated in such as a way that the results are weakly sensitive to the variation in mechanical properties of simulated tissues. In particular, the problems can be formulated into (i) pure-displacement and displacement zero traction problems whose solutions in displacement are weakly sensitive to mechanical properties of the considered continuum; and (ii) problems that are approximately statically determinate and therefore their solutions in stresses are weakly sensitive to mechanical properties of constituents [151]. It showed that reasonably accurate results can be expected for the brain tissues while using even the simplest constitutive model without the knowledge of patient-specific properties.

In general, deformable models play a fundamental role in the development of surgical simulation and could lead to a wide impact to the development of computer integrated surgery (CIS) system in the near future [1]. Currently, simulation software suites, such as the Simulation Open Framework Architecture (SOFA) [152], finite elements for biomechanics (FEBio) [153, 154], and open-source finite element toolkit (NiftySim) [71], have enabled a wide range of medical applications (see Fig. 6.2), such as interactive training system for interventional electrocardiology procedures [54], preoperative trajectory planning for percutaneous procedures [155], modelling of biomechanics of human liver during breathing [99], and biomechanically guided prone-to-supine image registration of breast magnetic resonance images (MRI) [156]. The development of deformable models have also facilitated the development of many medical applications such as tele-surgery for robotic surgery training [157], Chinese acupuncture training system [158], modelling of needle insertion [159], computer-assisted interventions [160, 161], and myringotomy simulation [162]. Further, the benefits of tissue modelling are useful not only for training, planning, and practice of surgical procedures, but also for optimising surgical tool design, creating “smart” instruments capable of assessing pathology or force-limiting novice surgeons, and understanding tissue injury mechanisms and damage thresholds [163, 164]. Despite recent progress in deformable modelling, the issues on error control [111] and clinical validation [12] still remain largely open topics, which could further facilitate the integration of CIS into clinical use and lead to more clinical impact.

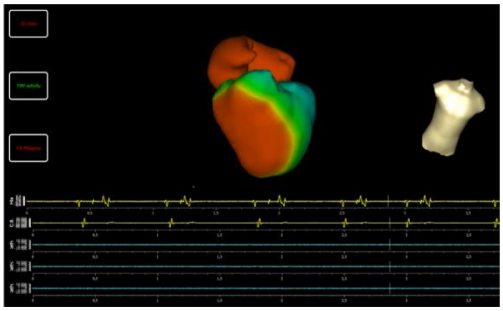

(a)

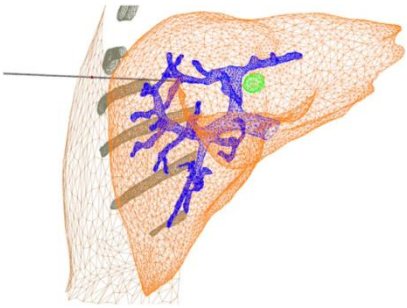

(b)

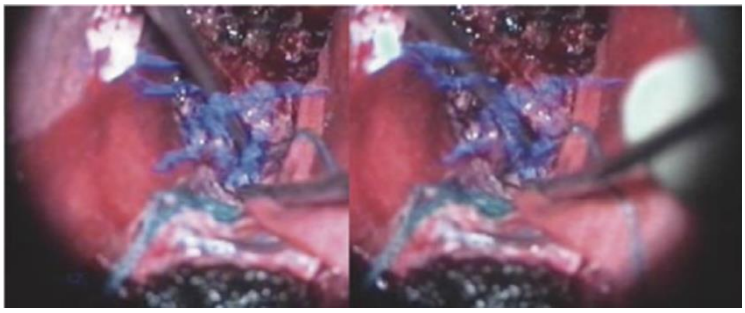

(c)

Figure 6.2 (a) An interactive training system for interventional electrocardiology procedures [54]; (b) a simulation scene of trajectory planning for percutaneous procedures [155]; and (c) a stereo pair showing MRI derived vasculature beneath the visible resected tissue surface [161].

7. Conclusions and Future Work

In this thesis, new methodologies are proposed for realistic and real-time soft tissue deformation for surgical simulation. The thesis presents the challenges existed in soft tissue deformation in Chapter 1, followed by the literature review on methodologies for realistic and real-time soft tissue deformation in Chapter 2. New methodologies are proposed regarding the ChainMail algorithm in Chapter 3, energy propagation method in Chapter 4, and energy balance method in Chapter 5 for soft tissue deformation. Finally, the methodologies for soft tissue deformation are discussed in Chapter 6 while outlining the remaining challenges of soft tissue modelling in surgical simulation. The proposed new methodologies are summarised below, followed by the proposed research of future work.

7.1 Proposed Methodology Summary

- **Time-Saving Volume-Energy-Conversed ChainMail Algorithm (Chapter 3.2):** This method allows different materials to be assigned to different chain elements to handle various material behaviours. A time-saving scheme is developed to improve computational efficiency for isotropic and homogeneous materials, and volume and strain energy conservation are proposed for realistic soft tissue deformation. Results demonstrate that the proposed method can not only handle isotropic and homogeneous, anisotropic and heterogeneous materials but also model soft tissues' incompressibility and relaxation behaviours.
- **Ellipsoid Bounding Region-based ChainMail Algorithm (Chapter 3.3):** This method employs an ellipsoid-shaped bounding region to control the movement of chain elements in the object. The ECBR complies with the concept of principle strains in continuum mechanics. It controls the strain of a chain link in the coordinate directions, independently from the chain link directions in the object mesh. New position adjustment rules are established based on the ECBR, leading to conservation of linear and angular momentums. Subsequently, temporal-domain model dynamics are derived from the position adjustment for dynamic simulation of soft tissue deformation. Experimental results demonstrate that the proposed ChainMail can not only reproduce the typical mechanical behaviours of soft tissues, but also handle large deformation. Isotropic and homogeneous, anisotropic and heterogeneous materials can be accommodated by simply changing the strain limit values. The proposed method also outperforms the traditional ChainMails, and the deformation results are in good agreement with those from commercial FEM software.
- **Neural Dynamics-based ChainMail Algorithm (Chapter 3.4):** This method achieves the nonlinear deformation of soft tissues via the nonlinear neural dynamics of CNN through the formulation of local connectivity of cells as the local position adjustments of ChainMail. Results demonstrate that the proposed method can produce soft tissues' nonlinear deformation as well as the typical mechanical behaviours.

- **Proposed Energy Propagation Method (Chapter 4.1):** This method formulates soft tissue deformation as the Poisson process of energy propagation to avoid complex and expensive computation of nonlinear elasticity. It combines Poisson propagation of mechanical load with non-rigid mechanical dynamics to govern the dynamics of soft tissue deformation. It also develops a finite volume scheme for spatial discretisation of Poisson equation on irregular volumetric soft tissue meshes. Simulation results demonstrate that the proposed method can not only reproduce the nonlinear force-displacement relationship and handle nonlinear deformation of soft tissues, but also accommodate isotropic and homogeneous, anisotropic and heterogeneous materials by simple modification of constitutive coefficient value of mass points.
- **Neural Dynamics-based Energy Propagation Method (Chapter 4.2):** This method employs CNN modelling of physical propagation of mechanical load and non-rigid mechanics of motion to achieve real-time computational performance, owing to the collective and simultaneous computing nature of cells. Simulations and experimental results show that the proposed method exhibits nonlinear force-displacement relationship, leading to the achievement of nonlinear large deformation for soft tissue modelling. Further, it can accommodate not only isotropic and homogeneous but also anisotropic and heterogeneous materials by simple modification of constitutive coefficient value of mass points. Interactive soft tissue deformation with haptic feedback is also achieved with the proposed method.
- **Neural Dynamics-based Stable Simulation of Soft Tissue Deformation (Chapter 4.3):** This method models the dynamic behaviours of soft tissues via the nonlinear neural dynamics of CNN by formulating the local connectivity of cells as the discrete non-rigid motion equation. Experimental results demonstrate that the proposed method can achieve good accuracy at a small time step and still remains numerically stable at a large time step while maintaining the computational efficiency of the explicit integration.
- **Energy Balance Method (Chapter 5):** This method formulates the process of soft tissue deformation as a process of work-energy balance, based on the law of conservation of energy, in which the work done by an external force is balanced against the strain energy done by the internal force. A novel position-based incremental approach is developed to achieve the work-energy balance by iteratively applying position increments for the equilibrium state of soft tissues. The position-based incremental approach is combined with non-rigid mechanics of motion to govern the dynamics of soft tissue deformation. Soft tissue deformation with haptic feedback is achieved with the proposed EBM. Simulations and experimental results demonstrate that the deformations of the proposed EBM are in good agreement with those by the commercial package of finite element analysis. Various soft tissue material properties, including isotropy, anisotropy, and viscoelasticity, can be modelled by specifying strain energy density functions. Further, the computational time of the proposed EBM is small, capable of achieving real-time performance for surgical simulation.

7.2 Future Work

- **Time-Saving Volume-Energy-Conversed ChainMail Algorithm (Chapter 3.2):** Future research work will focus on extending the proposed method to deal with complex surgical operations such as cutting, joining, tearing and suturing, which involve model topology change in addition to model deformation. Advanced algorithms will be developed in the future to model the complex surgical operations. Further, the current time-saving scheme is applied only to the isotopic and homogeneous materials; it is projected to extend the scheme to the modelling of anisotropic and heterogeneous materials in the future.
- **Ellipsoid Bounding Region-based ChainMail Algorithm (Chapter 3.3):** Future research work will focus on two aspects for improvement of the proposed method. The deformation behaviors are related to the selection of strain limits. The better the selection of strain limits is, the better the deformation results are. It is expected to develop an optimisation algorithm such as the Simulated Annealing and Genetic algorithm to optimise the selection of strain limits to further improve the modelling realism. The second aspect of future work is the global validation of the simulated deformation against *in vivo* data of soft tissues. The measurement of *in vivo* soft tissue behaviors would be of great value for a thorough validation but is much more challenging to achieve experimentally. A minimally invasive *in vivo* measurement will be established in the future to acquire mechanical data of soft tissues for full validation of the simulated deformation.
- **Neural Dynamics-based ChainMail Algorithm (Chapter 3.4):** Future research will be devoted to three aspects for enhancement of the proposed method. One is the scalability. Algorithms will be developed to map multiple chain elements to one single neural cell to expand the proposed method to accommodate the increase of chain elements. Another is material parameter determination. Optimisation algorithms will be developed to determine optimal material parameters for the nonlinear properties of soft tissues to further improve the modelling realism. Lastly is to generalise the ChainMail algorithm; investigations will be conducted to integrate the existing ChainMails to devise a unified ChainMail algorithm.
- **Proposed Energy Propagation Method (Chapter 4.1):** Future research work will focus on developing a minimally invasive experiment for full validation of the simulated deformation against *in vivo* data of soft tissues.
- **Neural Dynamics-based Energy Propagation Method (Chapter 4.2):** Future research work will focus on the extension of the proposed method to handle model topology changes such as cutting, joining and tearing. In addition to deformation, topology changes are also involved in these operations. To handle topology changes, the break point to break an edge will be identified using a threshold value of energy. Subsequently, new points will be introduced according to the transition of energy to form new control volumes and boundaries to achieve optimal energy distribution. It is expected that algorithms for handling topology changes will be developed, leading to a new energy propagation method to model both topology changes and deformation at the same time.

- **Neural Dynamics-based Stable Simulation of Soft Tissue Deformation (Chapter 4.3):** Future research work will focus on the use of nonlinear strain-stress relationship to formulate the local connectivity of cells to further improve the modelling realism.
- **Energy Balance Method (Chapter 5):** Future research work will focus on improvement of the proposed EBM. The proposed EBM will be extended for integration with GPU hardware to facilitate the computational performance. The current implementation only utilises the single core computing power of CPU without particular efforts on hardware acceleration. It is expected that the GPU acceleration solution will significantly improve the computational performance of the proposed EBM. In addition, the simulated deformations by the proposed EBM will be further verified against *in vivo* deformation of soft tissues. The measurement of *in vivo* soft tissue behaviours would be of great value for a thorough validation but is much more challenging to achieve experimentally. A minimally invasive *in vivo* measurement will be established in the future to acquire soft tissues' mechanical data for full validation of the simulated results. Further, the proposed EBM will be extended to model complex surgical operations such as cutting, joining, tearing and suturing. In addition to geometry changes, these operations also involve topology changes, which further lead to changes in the stiffness matrix of elements. Therefore, simulating these surgical operations is an even more challenging issue. Compared to conventional FEM method, the proposed EBM uses an iterative solution process without requiring the formulation of global stiffness matrix, leading to an advantage to model complex surgical operations.

Appendix A -Derivation of λ

Consider the governing equation of $\mathrm{ECBR}_{j,i}$ centred at point $\mathbf{C}(x_C, y_C, z_C)$ given by Eq. (3.33)

$$\left(\frac{x - x_C}{x_{j,i\ limit}}\right)^2 + \left(\frac{y - y_C}{y_{j,i\ limit}}\right)^2 + \left(\frac{z - z_C}{z_{j,i\ limit}}\right)^2 \leq 1 \tag{A.1}$$

The limit points $\mathbf{P_{max}}(x_{max}, y_{max}, z_{max})$ and $\mathbf{P_{min}}(x_{min}, y_{min}, z_{min})$ define the maximum extension length and minimum compression length of chain link $\mathbf{L_{ij}}$, and they are determined by identifying the intersection points between the boundary of $\mathrm{ECBR}_{j,i}$ and the infinite line of chain link $\mathbf{L_{ij}}$.

Since $\mathbf{P_{max}}$ and $\mathbf{P_{min}}$ are on the boundary of $\mathrm{ECBR}_{j,i}$, substituting $\mathbf{P_{max}}$ and $\mathbf{P_{min}}$ into Eq. (A.1), at the boundary limit:

$$\left(\frac{x_{max} - x_C}{x_{j,i\ limit}}\right)^2 + \left(\frac{y_{max} - y_C}{y_{j,i\ limit}}\right)^2 + \left(\frac{z_{max} - z_C}{z_{j,i\ limit}}\right)^2 = 1 \tag{A.2}$$

$$\left(\frac{x_{min} - x_C}{x_{j,i\ limit}}\right)^2 + \left(\frac{y_{min} - y_C}{y_{j,i\ limit}}\right)^2 + \left(\frac{z_{min} - z_C}{z_{j,i\ limit}}\right)^2 = 1 \tag{A.3}$$

Consider $\mathbf{P_{max}} = \mathbf{C} + \lambda\hat{\mathbf{u}}_{\mathbf{ij}}$ and $\mathbf{P_{min}} = \mathbf{C} - \lambda\hat{\mathbf{u}}_{\mathbf{ij}}$ given by Eq. (3.35) where $\hat{\mathbf{u}}_{\mathbf{ij}}(x_{ij,u}, y_{ij,u}, z_{ij,u})$ is the unit vector of chain link $\mathbf{L_{ij}}$. The coordinates of $\mathbf{P_{max}}$ and $\mathbf{P_{min}}$ can be written as

$$x_{max} = x_C + \lambda x_{ij,u} \tag{A.4}$$

$$y_{max} = y_C + \lambda y_{ij,u}$$

$$z_{max} = z_C + \lambda z_{ij,u}$$

$$x_{min} = x_C - \lambda x_{ij,u} \tag{A.5}$$

$$y_{min} = y_C - \lambda y_{ij,u}$$

$$z_{min} = z_C - \lambda z_{ij,u}$$

Substituting Eqs. (A.4) and (A.5) into Eqs. (A.2) and (A.3) respectively, we have

$$\lambda^2\left[\left(\frac{x_{ij,u}}{x_{j,i\ limit}}\right)^2 + \left(\frac{y_{ij,u}}{y_{j,i\ limit}}\right)^2 + \left(\frac{z_{ij,u}}{z_{j,i\ limit}}\right)^2\right] = 1 \tag{A.6}$$

Thus, λ is expressed as

$$\lambda = \frac{1}{\sqrt{\left(\frac{x_{ij,u}}{x_{j,i\ limit}}\right)^2 + \left(\frac{y_{ij,u}}{y_{j,i\ limit}}\right)^2 + \left(\frac{z_{ij,u}}{z_{j,i\ limit}}\right)^2}} \tag{A.7}$$

Appendix B -Proof of Linear and Angular Momentum Conservation for Position Adjustment

For the purpose of simplicity without loss of generality, we consider the case of two connected chain elements only. For any two connected chain elements i and j, the sum of linear momentum can be written as

$$m_i\left(-\frac{w_i}{w_i+w_j}\left(l_{max}-\left\|\overrightarrow{\mathbf{P}_\mathbf{i}^*\mathbf{P}_\mathbf{j}}\right\|\right)\hat{\mathbf{u}}_{\mathbf{i}^*\mathbf{j}}\right)+m_j\left(\frac{w_j}{w_i+w_j}\left(l_{max}-\left\|\overrightarrow{\mathbf{P}_\mathbf{i}^*\mathbf{P}_\mathbf{j}}\right\|\right)\hat{\mathbf{u}}_{\mathbf{i}^*\mathbf{j}}\right) \tag{B.1}$$

where $\hat{\mathbf{u}}_{\mathbf{i}^*\mathbf{j}}$ is the unit vector of chain link $\mathbf{L}_{\mathbf{i}^*\mathbf{j}}$ between $\mathbf{P}_\mathbf{i}^*$ and $\mathbf{P}_\mathbf{j}$.

Since $w_i = 1/m_i$ and $w_j = 1/m_j$, substituting them into Eq. (B.1) yields

$$\left(-\frac{1}{w_i+w_j}\left(l_{max}-\left\|\overrightarrow{\mathbf{P}_\mathbf{i}^*\mathbf{P}_\mathbf{j}}\right\|\right)\hat{\mathbf{u}}_{\mathbf{i}^*\mathbf{j}}\right)+\left(\frac{1}{w_i+w_j}\left(l_{max}-\left\|\overrightarrow{\mathbf{P}_\mathbf{i}^*\mathbf{P}_\mathbf{j}}\right\|\right)\hat{\mathbf{u}}_{\mathbf{i}^*\mathbf{j}}\right)=0 \tag{B.2}$$

Therefore, the condition of linear momentum conservation, i.e. Eq. (3.28) is satisfied.

The sum of angular momentum of chain elements i and j can be written as

$$\mathbf{r}_\mathbf{i}\times m_i\left(-\frac{w_i}{w_i+w_j}\left(l_{max}-\left\|\overrightarrow{\mathbf{P}_\mathbf{i}^*\mathbf{P}_\mathbf{j}}\right\|\right)\hat{\mathbf{u}}_{\mathbf{i}^*\mathbf{j}}\right)+\mathbf{r}_\mathbf{j}\times m_j\left(\frac{w_j}{w_i+w_j}\left(l_{max}-\left\|\overrightarrow{\mathbf{P}_\mathbf{i}^*\mathbf{P}_\mathbf{j}}\right\|\right)\hat{\mathbf{u}}_{\mathbf{i}^*\mathbf{j}}\right) \tag{B.3}$$

Eq. (B.3) may be simplified to

$$\frac{l_{max}-\left\|\overrightarrow{\mathbf{P}_\mathbf{i}^*\mathbf{P}_\mathbf{j}}\right\|}{w_i+w_j}\left(\mathbf{r}_\mathbf{i}\times(-\hat{\mathbf{u}}_{\mathbf{i}^*\mathbf{j}})+\mathbf{r}_\mathbf{j}\times\hat{\mathbf{u}}_{\mathbf{i}^*\mathbf{j}}\right) \tag{B.4}$$

By applying the vector cross product rule, Eq. (B.4) becomes

$$\frac{l_{max}-\left\|\overrightarrow{\mathbf{P}_\mathbf{i}^*\mathbf{P}_\mathbf{j}}\right\|}{w_i+w_j}\left(\left(-\|\mathbf{r}_\mathbf{i}\|\cdot\|\hat{\mathbf{u}}_{\mathbf{i}^*\mathbf{j}}\|\sin\theta_i\,\mathbf{n}\right)+\left(\|\mathbf{r}_\mathbf{j}\|\cdot\|\hat{\mathbf{u}}_{\mathbf{i}^*\mathbf{j}}\|\sin\theta_j\,\mathbf{n}\right)\right) \tag{B.5}$$

where θ_i and θ_j are the angles in the triangle formed by vectors $\mathbf{r}_\mathbf{i}$, $\mathbf{r}_\mathbf{j}$ and chain link $\mathbf{L}_{\mathbf{i}^*\mathbf{j}}$ between $\mathbf{P}_\mathbf{i}^*$ and $\mathbf{P}_\mathbf{j}$ (see Fig. B.1), and $\mathbf{n}$ is the unit vector perpendicular to the plane containing $\mathbf{r}_\mathbf{i}$, $\mathbf{r}_\mathbf{j}$ and $\hat{\mathbf{u}}_{\mathbf{i}^*\mathbf{j}}$.

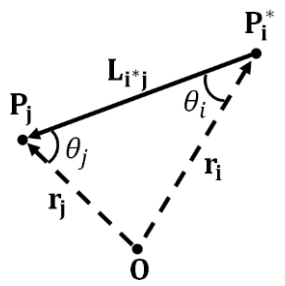

Figure B.1 Vectors $\mathbf{r_i}$, $\mathbf{r_j}$ and $\mathbf{L_{i^*j}}$ form a triangle: θ_i and θ_j are the internal angles, point $\mathbf{O}$ is an arbitrary common rotation centre.

Applying the sine rule yields

$$\frac{\|\mathbf{r_i}\|}{\sin\theta_j} = \frac{\|\mathbf{r_j}\|}{\sin\theta_i} \tag{B.6}$$

Substituting Eq. (B.6) into Eq. (B.5) yields

$$\frac{l_{max} - \left\|\overrightarrow{\mathbf{P_i^*P_j}}\right\|}{w_i + w_j}\left(\left(-\|\mathbf{r_i}\| \cdot \|\hat{\mathbf{u}}_{\mathbf{i^*j}}\| \sin\theta_i\,\mathbf{n}\right) + \left(\|\mathbf{r_i}\| \cdot \|\hat{\mathbf{u}}_{\mathbf{i^*j}}\| \sin\theta_i\,\mathbf{n}\right)\right) = 0 \tag{B.7}$$

Therefore, the condition of angular momentum conservation, i.e. Eq. (3.29) is satisfied.

List of Publications

- **Zhang, J.**, Zhong, Y., Smith, J., & Gu, C. (2016). A new ChainMail approach for real-time soft tissue simulation. *Bioengineered*, *7*(4), 246-252. DOI: 10.1080/21655979.2016.1197634 (Chapter **3.2**)
- **Zhang, J.**, Zhong, Y., Smith, J., & Gu, C. (2017). ChainMail based neural dynamics modelling of soft tissue deformation for surgical simulation. *Technology and Health Care*, *25*(S1), 231-239. DOI: 10.3233/THC-171325 (Chapter **3.4**)
- **Zhang, J.**, Zhong, Y., Smith, J., & Gu, C. (2017). Energy propagation modelling of nonlinear soft tissue deformation for surgical simulation. *SIMULATION*. DOI: 10.1177/0037549717720859 (Chapter **4.1**)
- **Zhang, J.**, Zhong, Y., Smith, J., & Gu, C. (2017). Neural dynamics-based Poisson propagation for deformable modelling. *Neural Computing and Applications*. DOI: 10.1007/s00521-017-3132-3 (Chapter **4.2**)
- **Zhang, J.**, Zhong, Y., Smith, J., & Gu, C. (2017). Cellular neural network modelling of soft tissue dynamics for surgical simulation. *Technology and Health Care*, *25*(S1), 337-344. DOI: 10.3233/THC-171337 (Chapter **4.3**)
- **Zhang, J.**, Zhong, Y., & Gu, C. (2017). Energy balance method for modelling of soft tissue deformation. *Computer-Aided Design*. DOI: 10.1016/j.cad.2017.07.006 (Chapter **5**)

References

[1] K. Miller, "Computational Biomechanics for Patient-Specific Applications," *Annals of Biomedical Engineering*, vol. 44, no. 1, pp. 1-2, 2016.

[2] H. Delingette, X. Pennec, L. Soler *et al.*, "Computational models for image-guided robot-assisted and simulated medical interventions," *Proceedings of the IEEE*, vol. 94, no. 9, pp. 1678-1688, Sep, 2006.

[3] H. Courtecuisse, J. Allard, P. Kerfriden *et al.*, "Real-time simulation of contact and cutting of heterogeneous soft-tissues," *Medical Image Analysis*, vol. 18, no. 2, pp. 394-410, Feb, 2014.

[4] Y.-J. Lim, and S. De, "Real time simulation of nonlinear tissue response in virtual surgery using the point collocation-based method of finite spheres," *Computer Methods in Applied Mechanics and Engineering*, vol. 196, no. 31-32, pp. 3011-3024, 2007.

[5] A. E. Kerdok, S. M. Cotin, M. P. Ottensmeyer *et al.*, "Truth cube: Establishing physical standards for soft tissue simulation," *Medical Image Analysis*, vol. 7, no. 3, pp. 283-291, Sep, 2003.

[6] T. W. Sederberg, and S. R. Parry, "Free-form deformation of solid geometric models," *ACM SIGGRAPH Computer Graphics*, vol. 20, no. 4, pp. 151-160, 1986.

[7] S. A. Cover, N. F. Ezquerra, J. F. O'Brien *et al.*, "Interactively deformable models for surgery simulation," *IEEE Computer Graphics and Applications*, vol. 13, no. 6, pp. 68-75, 1993.

[8] Y. Duan, W. Huang, H. Chang *et al.*, "Volume Preserved Mass-Spring Model with Novel Constraints for Soft Tissue Deformation," *IEEE Journal of Biomedical and Health Informatics*, vol. 20, no. 1, pp. 268-280, 2016.

[9] P. E. Hammer, M. S. Sacks, P. Del Nido, J *et al.*, "Mass-spring model for simulation of heart valve tissue mechanical behavior," *Annals of Biomedical Engineering*, vol. 39, no. 6, pp. 1668-1679, 2011.

[10] A. Nealen, M. Müller, R. Keiser *et al.*, "Physically based deformable models in computer graphics," *Computer Graphics Forum*, vol. 25, no. 4, pp. 809-836, 2006.

[11] U. Meier, O. Lopez, C. Monserrat *et al.*, "Real-time deformable models for surgery simulation: a survey," *Computer Methods and Programs in Biomedicine*, vol. 77, no. 3, pp. 183-197, 2005.

[12] H. Delingette, "Toward realistic soft-tissue modeling in medical simulation," *Proceedings of the IEEE*, vol. 86, no. 3, pp. 512-523, Mar, 1998.

[13] S. F. Gibson, and B. Mirtich, "A survey of deformable modeling in computer graphics," 1997.

[14] G. San-Vicente, I. Aguinaga, and J. Tomas Celigueta, "Cubical Mass-Spring Model design based on a tensile deformation test and nonlinear material model," *IEEE Transactions on Visualization and Computer Graphics*, vol. 18, no. 2, pp. 228-241, Feb, 2012.

[15] G. Picinbono, H. Delingette, and N. Ayache, "Non-linear anisotropic elasticity for real-time surgery simulation," *Graphical Models*, vol. 65, no. 5, pp. 305-321, Sep, 2003.

[16] K.-S. Choi, H. Sun, and P.-A. Heng, "An efficient and scalable deformable model for virtual reality-based medical applications," *Artificial Intelligence in Medicine*, vol. 32, no. 1, pp. 51-69, 2004.

[17] E. Basafa, and F. Farahmand, "Real-time simulation of the nonlinear visco-elastic deformations of soft tissues," *International Journal of Computer Assisted Radiology and Surgery*, vol. 6, no. 3, pp. 297-307, 2011.

[18] J. Qin, W.-M. Pang, Y.-P. Chui *et al.*, "A novel modeling framework for multilayered soft tissue deformation in virtual orthopedic surgery," *Journal of Medical Systems*, vol. 34, no. 3, pp. 261-271, Jun, 2010.

[19] K. S. Choi, H. Sun, and P. A. Heng, "Interactive deformation of soft tissues with haptic feedback for medical learning," *IEEE Transactions on Information Technology in Biomedicine*, vol. 7, no. 4, pp. 358-363, Dec, 2003.

[20] J. Qin, K.-S. Choi, and P.-A. Heng, "Collaborative simulation of soft-tissue deformation for virtual surgery applications," *Journal of Medical Systems*, vol. 34, no. 3, pp. 367-378, Jun, 2010.

[21] S. De, J. Kim, Y.-J. Lim *et al.*, "The point collocation-based method of finite spheres (PCMFS) for real time surgery simulation," *Computers & Structures*, vol. 83, no. 17–18, pp. 1515-1525, 6//, 2005.

[22] O. Deussen, L. Kobbelt, and P. Tücke, "Using simulated annealing to obtain good nodal approximations of deformable bodies," 1995.

[23] J. Louchet, X. Provot, and D. Crochemore, "Evolutionary identification of cloth animation models," *Computer Animation and Simulation'95*, pp. 44-54: Springer, 1995.
[24] S. F. Frisken-Gibson, "3D ChainMail: a Fast Algorithm for Deforming Volumetric Objects," *Proceedings of the Symposium on Interactive 3D graphics*, pp. 149-154, 1997.
[25] S. Gibson, C. Fyock, E. Grimson *et al.*, "Volumetric object modeling for surgical simulation," *Medical Image Analysis*, vol. 2, no. 2, pp. 121-132, Jun, 1998.
[26] S. F. Frisken-Gibson, "Using linked volumes to model object collisions, deformation, cutting, carving, and joining," *IEEE Transactions on Visualization and Computer Graphics*, vol. 5, no. 4, pp. 333-348, Oct, 1999.
[27] A. Rodríguez, A. León, and G. Arroyo, "Parallel deformation of heterogeneous ChainMail models: Application to interactive deformation of large medical volumes," *Computers in Biology and Medicine*, vol. 79, pp. 222-232, 2016.
[28] D. Fortmeier, A. Mastmeyer, J. Schroder *et al.*, "A Virtual Reality System for PTCD Simulation Using Direct Visuo-Haptic Rendering of Partially Segmented Image Data," *IEEE Journal of Biomedical and Health Informatics*, vol. 20, no. 1, pp. 355-366, Jan, 2016.
[29] A. Rodriguez, A. Leon, G. Arroyo *et al.*, "SP-ChainMail: a GPU-based sparse parallel ChainMail algorithm for deforming medical volumes," *Journal of Supercomputing*, vol. 71, no. 9, pp. 3482-3499, Sep, 2015.
[30] M. A. Schill, S. F. F. Gibson, H.-J. Bender *et al.*, "Biomechanical simulation of the vitreous humor in the eye using an enhanced chainmail algorithm," *Medical Image Computing and Computer-Assisted Interventation*, pp. 679-687: Springer, 1998.
[31] J. Park, S. Y. Kim, S. W. Son *et al.*, "Shape retaining chain linked model for real-time volume haptic rendering," *IEEE/ACM Siggraph Symposium on Volume Visualization and Graphics 2002, Proceedings*, pp. 65-72, 2002.
[32] X. G. Wang, and A. Fenster, "A virtual reality based 3D real-time interactive brachytherapy simulation of needle insertion and seed implantation," *2004 2nd IEEE International Symposium on Biomedical Imaging: Macro to Nano, Vols 1 and 2*, pp. 280-283, 2004.
[33] Y. Li, K. Brodlie, and N. Phillips, "Real-time soft tissue modelling for web-based surgical simulation: SurfaceChainMail," *Studies in Health Technology and Informatics*, vol. 85, pp. 261-267, 2002.
[34] Y. Li, and K. Brodlie, "Soft Object Modelling with Generalised ChainMail - Extending the Boundaries of Web-based Graphics," *Computer Graphics Forum*, vol. 22, no. 4, pp. 717-727, Dec, 2003.
[35] J. Wang, and W. F. Lu, "A real-time haptics-based deformable model for virtual prototyping and simulations," *ASME 2009 International Design Engineering Technical Conferences and Computers and Information in Engineering Conference*, pp. 1601-1610, 2009.
[36] D. Levin, A. Fenster, and H. M. Ladak, "A hybrid deformable model for simulating prostate brachytherapy," *Medical Imaging*, vol. 6141, pp. 61410Q-61410Q-10, 2006.
[37] A. Duysak, and J. J. Zhang, "Fast simulation of deformable objects," *Eighth International Conference on Information Visualisation, Proceedings*, pp. 422-427, 2004.
[38] D.-I. A. Neubauer, "A ChainMail Algorithm for Direct Volume Deformation in Virtual Endoscopy Applications," PhD thesis, 2005.
[39] S. F. F. Gibson, J. Samosky, A. Mor *et al.*, "Simulating arthroscopic knee surgery using volumetric object representations, real-time volume rendering and haptic feedback," *CVRMed-MRCAS'97*, pp. 367-378, 1996.
[40] M. A. Schill, C. Wagner, M. Hennen *et al.*, "Eyesi–a simulator for intra-ocular surgery," *Medical Image Computing and Computer-Assisted Intervention–MICCAI'99*, vol. 1679, pp. 1166-1174, 1999.
[41] X. Wang, and A. Fenster, "A haptic-enhanced 3D real-time interactive needle insertion simulation for prostate brachytherapy," *Medical Imaging*, vol. 5367, pp. 781-789, 2004.
[42] P. F. Villard, F. P. Vidal, L. ap Cenydd *et al.*, "Interventional radiology virtual simulator for liver biopsy," *International Journal of Computer Assisted Radiology and Surgery*, vol. 9, no. 2, pp. 255-267, Mar, 2014.
[43] T. Le Fol, O. Acosta-Tamayo, A. Lucas *et al.*, "Angioplasty simulation using ChainMail method," *Medical Imaging*, pp. 65092X-65092X-8, 2007.

[44] D. Fortmeier, A. Mastmeyer, and H. Handels, "Image-Based Palpation Simulation With Soft Tissue Deformations Using Chainmail on the GPU," *Bildverarbeitung für die Medizin 2013*, pp. 140-145: Springer, 2013.

[45] J. Zhang, Y. Zhong, J. Smith *et al.*, "A new ChainMail approach for real-time soft tissue simulation," *Bioengineered*, vol. 7, no. 4, pp. 246-252, Jul 03, 2016.

[46] J. Zhang, Y. Zhong, J. Smith *et al.*, "ChainMail based neural dynamics modeling of soft tissue deformation for surgical simulation," *Technology and Health Care*, vol. 25, no. S1, pp. 231-239, May 19, 2017.

[47] M. Camara, E. Mayer, A. Darzi *et al.*, "Soft tissue deformation for surgical simulation: a position-based dynamics approach," *International Journal of Computer Assisted Radiology and Surgery*, vol. 11, no. 6, pp. 919-928, 2016.

[48] M. Müller, B. Heidelberger, M. Teschner *et al.*, "Meshless deformations based on shape matching," *ACM Transactions on Graphics (TOG)*, vol. 24, no. 3, pp. 471-478, 2005.

[49] O. Zienkiewicz, R. Taylor, and J. Zhu, *The finite element method: its basis and fundamentals*: Butterworth-Heinemann, 2005.

[50] M. Freutel, H. Schmidt, L. Durselen *et al.*, "Finite element modeling of soft tissues: Material models, tissue interaction and challenges," *Clinical Biomechanics*, vol. 29, no. 4, pp. 363-372, 2014.

[51] R. Plantefève, I. Peterlik, N. Haouchine *et al.*, "Patient-Specific Biomechanical Modeling for Guidance During Minimally-Invasive Hepatic Surgery," *Annals of Biomedical Engineering*, vol. 44, no. 1, pp. 139-153, 2016.

[52] G. R. Joldes, A. Wittek, and K. Miller, "Suite of finite element algorithms for accurate computation of soft tissue deformation for surgical simulation," *Medical Image Analysis*, vol. 13, no. 6, pp. 912-919, Dec, 2009.

[53] M. Li, K. Miller, G. R. Joldes *et al.*, "Patient-specific biomechanical model as whole-body CT image registration tool," *Medical Image Analysis*, vol. 22, no. 1, pp. 22-34, May, 2015.

[54] H. Talbot, F. Spadoni, C. Duriez *et al.*, "Interactive training system for interventional electrocardiology procedures," *Medical Image Analysis*, vol. 35, pp. 225-237, 1//, 2017.

[55] M. Bro-Nielsen, "Finite element modeling in surgery simulation," *Proceedings of the IEEE*, vol. 86, no. 3, pp. 490-503, Mar, 1998.

[56] K. Miller, G. Joldes, D. Lance *et al.*, "Total Lagrangian explicit dynamics finite element algorithm for computing soft tissue deformation," *International Journal for Numerical Methods in Biomedical Engineering*, vol. 23, no. 2, pp. 121-134, 2007.

[57] M. Bro-Nielsen, and S. Cotin, "Real-time Volumetric Deformable Models for Surgery Simulation using Finite Elements and Condensation," *Computer Graphics Forum*, vol. 15, no. 3, pp. 57-66, 1996.

[58] W. Wu, and P. A. Heng, "An improved scheme of an interactive finite element model for 3D soft-tissue cutting and deformation," *The Visual Computer*, vol. 21, no. 8-10, pp. 707-716, Sep, 2005.

[59] S. Cotin, H. Delingette, and N. Ayache, "Real-Time Elastic Deformations of Soft Tissues for Surgery Simulation," *IEEE Transactions on Visualization and Computer Graphics*, vol. 5, no. 1, pp. 62-73, 1999.

[60] S. Cotin, H. Delingette, and N. Ayache, "A hybrid elastic model for real-time cutting, deformations, and force feedback for surgery training and simulation," *The Visual Computer*, vol. 16, no. 8, pp. 437-452, 2000.

[61] C. Monserrat, U. Meier, M. Alcaniz *et al.*, "A new approach for the real-time simulation of tissue deformations in surgery simulation," *Computer Methods and Programs in Biomedicine*, vol. 64, no. 2, pp. 77-85, 2001.

[62] B. Zhu, and L. Gu, "A hybrid deformable model for real-time surgical simulation," *Computerized Medical Imaging and Graphics*, vol. 36, no. 5, pp. 356-365, 2012.

[63] P. Wang, A. A. Becker, I. A. Jones *et al.*, "Virtual reality simulation of surgery with haptic feedback based on the boundary element method," *Computers & Structures*, vol. 85, no. 7-8, pp. 331-339, Apr, 2007.

[64] W. Tang, and T. R. Wan, "Constraint-based soft tissue simulation for virtual surgical training," *IEEE Transactions on Biomedical Engineering*, vol. 61, no. 11, pp. 2698-2706, 2014.

[65] X. P. P. Liu, S. P. Xu, H. Zhang *et al.*, "A New Hybrid Soft Tissue Model for Visio-Haptic Simulation," *IEEE Transactions on Instrumentation and Measurement,* vol. 60, no. 11, pp. 3570-3581, Nov, 2011.

[66] F. Goulette, and Z.-W. Chen, "Fast computation of soft tissue deformations in real-time simulation with Hyper-Elastic Mass Links," *Computer Methods in Applied Mechanics and Engineering,* vol. 295, pp. 18-38, 2015.

[67] K. Miller, A. Wittek, G. Joldes *et al.*, "Modelling brain deformations for computer-integrated neurosurgery," *International Journal for Numerical Methods in Biomedical Engineering,* vol. 26, no. 1, pp. 117-138, 2010.

[68] G. Szekely, C. Brechbuhler, R. Hutter *et al.*, "Modelling of soft tissue deformation for laparoscopic surgery simulation," *Medical Image Analysis,* vol. 4, no. 1, pp. 57-66, Mar, 2000.

[69] Z. A. Taylor, M. Cheng, and S. Ourselin, "High-Speed Nonlinear Finite Element Analysis for Surgical Simulation Using Graphics Processing Units," *IEEE Transactions on Medical Imaging,* vol. 27, no. 5, pp. 650-663, May, 2008.

[70] Z. A. Taylor, O. Comas, M. Cheng *et al.*, "On modelling of anisotropic viscoelasticity for soft tissue simulation: numerical solution and GPU execution," *Medical Image Analysis,* vol. 13, no. 2, pp. 234-244, Apr, 2009.

[71] S. F. Johnsen, Z. A. Taylor, M. J. Clarkson *et al.*, "NiftySim: A GPU-based nonlinear finite element package for simulation of soft tissue biomechanics," *International Journal of Computer Assisted Radiology and Surgery,* vol. 10, no. 7, pp. 1077-1095, 2015.

[72] G. R. Joldes, A. Wittek, and K. Miller, "Real-time nonlinear finite element computations on GPU–Application to neurosurgical simulation," *Computer Methods in Applied Mechanics and Engineering,* vol. 199, no. 49-52, pp. 3305-3314, 2010.

[73] V. Strbac, J. V. Sloten, and N. Famaey, "Analyzing the potential of GPGPUs for real-time explicit finite element analysis of soft tissue deformation using CUDA," *Finite Elements in Analysis and Design,* vol. 105, pp. 79-89, 2015.

[74] S. Marchesseau, T. Heimann, S. Chatelin *et al.*, "Fast porous visco-hyperelastic soft tissue model for surgery simulation: application to liver surgery," *Progress in Biophysics & Molecular Biology,* vol. 103, no. 2-3, pp. 185-196, Dec, 2010.

[75] R. Mafi, and S. Sirouspour, "GPU-based acceleration of computations in nonlinear finite element deformation analysis," *International Journal for Numerical Methods in Biomedical Engineering,* vol. 30, no. 3, pp. 365-381, 2014.

[76] A. Radermacher, and S. Reese, "A comparison of projection-based model reduction concepts in the context of nonlinear biomechanics," *Archive of Applied Mechanics,* vol. 83, no. 8, pp. 1193-1213, 2013.

[77] S. Niroomandi, I. Alfaro, D. Gonzalez *et al.*, "Real-time simulation of surgery by reduced-order modeling and X-FEM techniques," *International Journal for Numerical Methods in Biomedical Engineering,* vol. 28, no. 5, pp. 574-588, May, 2012.

[78] S. Niroomandi, I. Alfaro, E. Cueto *et al.*, "Real-time deformable models of non-linear tissues by model reduction techniques," *Computer Methods and Programs in Biomedicine,* vol. 91, no. 3, pp. 223-231, 2008.

[79] S. Niroomandi, I. Alfaro, E. Cueto *et al.*, "Accounting for large deformations in real-time simulations of soft tissues based on reduced-order models," *Computer Methods and Programs in Biomedicine,* vol. 105, no. 1, pp. 1-12, Jan, 2012.

[80] S. Niroomandi, D. González, I. Alfaro *et al.*, "Real-time simulation of biological soft tissues: a PGD approach," *International Journal for Numerical Methods in Biomedical Engineering,* vol. 29, no. 5, pp. 586-600, 2013.

[81] A. Radermacher, and S. Reese, "POD-based model reduction with empirical interpolation applied to nonlinear elasticity," *International Journal for Numerical Methods in Engineering,* vol. 107, no. 6, pp. 477-495, Aug, 2016.

[82] E. Cueto, and F. Chinesta, "Real time simulation for computational surgery: a review," *Advanced Modeling and Simulation in Engineering Sciences,* vol. 1, no. 1, pp. 11, 2014.

[83] G. R. Joldes, A. Wittek, and K. Miller, "An efficient hourglass control implementation for the uniform strain hexahedron using the Total Lagrangian formulation," *International Journal for Numerical Methods in Biomedical Engineering,* vol. 24, no. 11, pp. 1315-1323, 2008.

[84] G. R. Joldes, A. Wittek, and K. Miller, "Non-locking tetrahedral finite element for surgical simulation," *International Journal for Numerical Methods in Biomedical Engineering,* vol. 25, no. 7, pp. 827-836, 2009.

[85] A. Horton, A. Wittek, G. R. Joldes *et al.*, "A meshless Total Lagrangian explicit dynamics algorithm for surgical simulation," *International Journal for Numerical Methods in Biomedical Engineering,* vol. 26, no. 8, pp. 977-998, Aug, 2010.

[86] G. R. Joldes, A. Wittek, and K. Miller, "Stable time step estimates for mesh-free particle methods," *International Journal for Numerical Methods in Engineering,* vol. 91, no. 4, pp. 450-456, 2012.

[87] K. Miller, A. Horton, G. R. Joldes *et al.*, "Beyond finite elements: a comprehensive, patient-specific neurosurgical simulation utilizing a meshless method," *Journal of Biomechanics,* vol. 45, no. 15, pp. 2698-701, Oct 11, 2012.

[88] R. Aras, Y. Shen, and M. Audette, "An analytic meshless enrichment function for handling discontinuities in interactive surgical simulation," *Advances in Engineering Software,* vol. 102, pp. 40-48, 2016.

[89] Y. Zou, and P. X. Liu, "A high-resolution model for soft tissue deformation based on point primitives," *Computer Methods and Programs in Biomedicine,* vol. 148, pp. 113-121, 9, 2017.

[90] G. Y. Zhang, A. Wittek, G. R. Joldes *et al.*, "A three-dimensional nonlinear meshfree algorithm for simulating mechanical responses of soft tissue," *Engineering Analysis with Boundary Elements,* vol. 42, pp. 60-66, 2014.

[91] Y. Zou, P. X. Liu, Q. Cheng *et al.*, "A New Deformation Model of Biological Tissue for Surgery Simulation," *IEEE Transactions on Cybernetics,* pp. 1-10, 2016.

[92] H. A. Chowdhury, A. Wittek, K. Miller *et al.*, "An Element Free Galerkin Method Based on the Modified Moving Least Squares Approximation," *Journal of Scientific Computing,* vol. 71, no. 3, pp. 1-15, 2016.

[93] A. Palyanov, S. Khayrulin, and S. D. Larson, "Application of smoothed particle hydrodynamics to modeling mechanisms of biological tissue," *Advances in Engineering Software,* vol. 98, pp. 1-11, 2016.

[94] M. K. Rausch, G. E. Karniadakis, and J. D. Humphrey, "Modeling Soft Tissue Damage and Failure Using a Combined Particle/Continuum Approach," *Biomechanics and Modeling in Mechanobiology,* pp. 1-13, 2016.

[95] S. Banihani, T. Rabczuk, and T. Almomani, "POD for real-time simulation of hyperelastic soft biological tissue using the point collocation method of finite spheres," *Mathematical Problems in Engineering,* vol. 2013, 2013.

[96] A. Wittek, N. M. Grosland, G. R. Joldes *et al.*, "From Finite Element Meshes to Clouds of Points: A Review of Methods for Generation of Computational Biomechanics Models for Patient-Specific Applications," *Annals of Biomedical Engineering,* vol. 44, no. 1, pp. 3-15, 2016.

[97] Y. Zhong, B. Shirinzadeh, G. Alici *et al.*, "A Cellular Neural Network Methodology for Deformable Object Simulation," *IEEE Transactions on Information Technology in Biomedicine,* vol. 10, no. 4, pp. 749-762, Oct, 2006.

[98] S. De, D. Deo, G. Sankaranarayanan *et al.*, "A physics-driven neural networks-based simulation system (phynness) for multimodal interactive virtual environments involving nonlinear deformable objects," *Presence: Teleoperators and Virtual Environments,* vol. 20, no. 4, pp. 289-308, Aug, 2011.

[99] D. Lorente, F. Martínez-Martínez, M. J. Rupérez *et al.*, "A framework for modelling the biomechanical behaviour of the human liver during breathing in real time using machine learning," *Expert Systems with Applications,* vol. 71, pp. 342-357, 2017.

[100] B. Bickel, M. Bäecher, M. A. Otaduy *et al.*, "Capture and modeling of non-linear heterogeneous soft tissue," *ACM Transactions on Graphics (TOG),* vol. 28, no. 3, pp. 89, 2009.

[101] I. F. Costa, "A novel deformation method for fast simulation of biological tissue formed by fibers and fluid," *Medical Image Analysis,* vol. 16, no. 5, pp. 1038-1046, Jul, 2012.

[102] T. Liu, A. W. Bargteil, J. F. O'Brien *et al.*, "Fast simulation of mass-spring systems," *ACM Transactions on Graphics (TOG),* vol. 32, no. 6, pp. 1-7, Nov, 2013.

[103] B. Fierz, J. Spillmann, I. Aguinaga Hoyos *et al.*, "Maintaining large time steps in explicit finite element simulations using shape matching," *IEEE Transactions on Visualization and Computer Graphics,* vol. 18, no. 5, pp. 717-728, May, 2012.

[104] M. H. Doweidar, B. Calvo, I. Alfaro *et al.*, "A comparison of implicit and explicit natural element methods in large strains problems: Application to soft biological tissues modeling," *Computer Methods in Applied Mechanics and Engineering*, vol. 199, no. 25-28, pp. 1691-1700, 2010.
[105] M. Hauth, O. Etzmuß, and W. Straßer, "Analysis of numerical methods for the simulation of deformable models," *The Visual Computer*, vol. 19, no. 7-8, pp. 581-600, Dec, 2003.
[106] K.-J. Bathe, *Finite element procedures*: Klaus-Jurgen Bathe, 2006.
[107] T. J. Hughes, *The finite element method: linear static and dynamic finite element analysis*: Courier Corporation, 2012.
[108] Z. A. Taylor, S. Crozier, and S. Ourselin, "A reduced order explicit dynamic finite element algorithm for surgical simulation," *IEEE Transactions on Medical Imaging*, vol. 30, no. 9, pp. 1713-1721, Sep, 2011.
[109] G. R. Joldes, A. Wittek, and K. Miller, "Computation of intra-operative brain shift using dynamic relaxation," *Computer Methods in Applied Mechanics and Engineering*, vol. 198, no. 41-44, pp. 3313-3320, 2009.
[110] G. R. Joldes, A. Wittek, and K. Miller, "An adaptive dynamic relaxation method for solving nonlinear finite element problems. Application to brain shift estimation," *International Journal for Numerical Methods in Biomedical Engineering*, vol. 27, no. 2, pp. 173-185, 2011.
[111] H. P. Bui, S. Tomar, H. Courtecuisse *et al.*, "Real-time error control for surgical simulation," *IEEE Transactions on Biomedical Engineering*, 2017.
[112] Y.-C. Fung, *Biomechanics: Mechanical Properties of Living Tissues*: Springer-Verlag, 1993.
[113] J. Bender, M. Müller, M. A. Otaduy *et al.*, "A Survey on Position-Based Simulation Methods in Computer Graphics," *Computer Graphics Forum*, vol. 33, no. 6, pp. 228-251, 2014.
[114] J. Pan, J. Bai, X. Zhao *et al.*, "Real-time haptic manipulation and cutting of hybrid soft tissue models by extended position-based dynamics," *Computer Animation and Virtual Worlds*, vol. 26, no. 3-4, pp. 321-335, 2015.
[115] L. S. Srinath, *Advanced mechanics of solids*: Tata McGraw-Hill, 2003.
[116] N.-H. Kim, *Introduction to nonlinear finite element analysis*: Springer Science & Business Media, 2014.
[117] M. Muller, B. Heidelberger, M. Hennix *et al.*, "Position based dynamics," *Journal of Visual Communication and Image Representation*, vol. 18, no. 2, pp. 109-118, Apr, 2007.
[118] I. Peterlík, C. Duriez, and S. Cotin, "Modeling and real-time simulation of a vascularized liver tissue," *Medical Image Computing and Computer-Assisted Intervention–MICCAI 2012*, pp. 50-57: Springer, 2012.
[119] R. Barauskas, A. Gulbinas, and G. Barauskas, "Investigation of radiofrequency ablation process in liver tissue by finite element modeling and experiment," *Medicina*, vol. 43, no. 4, pp. 310-325, 2007.
[120] G. Picinbono, J. C. Lombardo, H. Delingette *et al.*, "Improving realism of a surgery simulator: linear anisotropic elasticity, complex interactions and force extrapolation," *The Journal of Visualization and Computer Animation*, vol. 13, no. 3, pp. 147-167, Jul, 2002.
[121] L. O. Chua, and L. Yang, "Cellular Neural Networks: Theory," *IEEE Transactions on Circuits and Systems*, vol. 35, no. 10, pp. 1257-1272, 1988.
[122] P. Thiran, G. Setti, and M. Hasler, "An Approach to Information Propagation in 1-D Cellular Neural Networks - Part I: Local Diffusion," *IEEE Transactions on Circuits and Systems I: Fundamental Theory and Applications*, vol. 45, no. 8, pp. 777-789, 1998.
[123] G. Setti, P. Thiran, and C. Serpico, "An Approach to Information Propagation in 1-D Cellular Neural Networks - Part II: Global Propagation," *IEEE Transactions on Circuits and Systems I: Fundamental Theory and Applications*, vol. 45, no. 8, pp. 790-811, 1998.
[124] L. O. Chua, M. Hasler, G. S. Moschytz *et al.*, "Autonomous Cellular Neural Networks: A Unified Paradigm for Pattern Formation and Active Wave Propagation," *IEEE Transactions on Circuits and Systems I: Fundamental Theory and Applications*, vol. 42, no. 10, pp. 559-577, 1995.
[125] M. H. Sadd, *Elasticity: theory, applications, and numerics*: Academic Press, 2009.
[126] Y. Zhong, B. Shirinzadeh, and J. Smith, "Soft tissue deformation with neural dynamics for surgery simulation," *International Journal of Robotics and Automation*, vol. 22, no. 1, pp. 1-9, 2007.

[127] A. P. Selvadurai, *Partial Differential Equations in Mechanics 2: the Biharmonic Equation, Poisson's Equation*: Springer Science & Business Media, 2013.
[128] P. Vijayan, and Y. Kallinderis, "A 3D finite-volume scheme for the Euler equations on adaptive tetrahedral grids," *Journal of Computational Physics*, vol. 113, no. 2, pp. 249-267, Aug, 1994.
[129] J. Blazek, *Computational Fluid Dynamics: Principles and Applications*: Elsevier, 2001.
[130] H. Nishikawa, "Beyond interface gradient: A general principle for constructing diffusion schemes." p. 5093.
[131] S. Xu, X. Liu, H. Zhang *et al.*, "A Nonlinear Viscoelastic Tensor-Mass Visual Model for Surgery Simulation," *IEEE Transactions on Instrumentation and Measurement*, vol. 60, no. 1, pp. 14-20, 2011.
[132] L. O. Chua, and T. Roska, "The CNN Paradigm," *IEEE Transactions on Circuits and Systems I-Fundamental Theory and Applications*, vol. 40, no. 3, pp. 147-156, 1993.
[133] T. Kozek, L. O. Chua, T. Roska *et al.*, "Simulating nonlinear waves and partial differential equations via CNN - Part II: Typical Examples," *IEEE Transactions on Circuits and Systems I: Fundamental Theory and Applications*, vol. 42, no. 10, pp. 816-820, 1995.
[134] P. Szolgay, G. Vörös, and G. Erőss, "On the applications of the cellular neural network paradigm in mechanical vibrating systems," *IEEE Transactions on Circuits and Systems I: Fundamental Theory and Applications*, vol. 40, no. 3, pp. 222-227, 1993.
[135] T. Roska, L. O. Chua, D. Wolf *et al.*, "Simulating nonlinear waves and partial differential equations via CNN - Part I: Basic Techniques," *IEEE Transactions on Circuits and Systems I: Fundamental Theory and Applications*, vol. 42, no. 10, pp. 807-815, 1995.
[136] T. Roska, and L. O. Chua, "Cellular neural networks with non-linear and delay-type template elements and non-uniform grids," *International Journal of Circuit Theory and Applications*, vol. 20, no. 5, pp. 469-481, 1992.
[137] Y. Zhong, B. Shirinzadeh, G. Alici *et al.*, "A Poisson-based methodology for deformable object simulation," *International Journal of Modelling and Simulation*, vol. 28, no. 2, pp. 156, 2008.
[138] Z. Jingya, W. Jiajun, W. Xiuying *et al.*, "The adaptive FEM elastic model for medical image registration," *Physics in Medicine and Biology*, vol. 59, no. 1, pp. 97-118, Jan 06, 2014.
[139] J. Misra, and I. Saha, "Artificial neural networks in hardware A survey of two decades of progress," *Neurocomputing*, vol. 74, no. 1-3, pp. 239-255, Dec, 2010.
[140] Z. Ullah, and C. E. Augarde, "Finite deformation elasto-plastic modelling using an adaptive meshless method," *Computers & Structures*, vol. 118, no. S1, pp. 39-52, 2013.
[141] P. Xia, "New advances for haptic rendering: state of the art," *The Visual Computer*, pp. 1-17, 2016.
[142] E. Forest, and R. D. Ruth, "Fourth-order symplectic integration," *Physica D: Nonlinear Phenomena*, vol. 43, no. 1, pp. 105-117, 1990.
[143] J. A. Weiss, B. N. Maker, and S. Govindjee, "Finite element implementation of incompressible, transversely isotropic hyperelasticity," *Computer Methods in Applied Mechanics and Engineering*, vol. 135, no. 1, pp. 107-128, 1996.
[144] H. Si, "TetGen, a Delaunay-based quality tetrahedral mesh generator," *ACM Transactions on Mathematical Software (TOMS)*, vol. 41, no. 2, pp. 11, 2015.
[145] C. Quesada, D. González, I. Alfaro *et al.*, "Computational vademecums for real-time simulation of surgical cutting in haptic environments," *International Journal for Numerical Methods in Engineering*, vol. 108, no. 10, pp. 1230-1247, 2016.
[146] J. Stunt, P. Wulms, G. Kerkhoffs *et al.*, "How valid are commercially available medical simulators?," *Advances in medical education and practice*, vol. 5, pp. 385, 2014.
[147] C. D. Lallas, J. W. Davis, and S. Members Of The Society Of Urologic Robotic, "Robotic surgery training with commercially available simulation systems in 2011: a current review and practice pattern survey from the society of urologic robotic surgeons," *J Endourol*, vol. 26, no. 3, pp. 283-93, Mar, 2012.
[148] M. Abadi, A. Agarwal, P. Barham *et al.*, "Tensorflow: Large-scale machine learning on heterogeneous distributed systems," *arXiv preprint arXiv:1603.04467*, 2016.
[149] Hibbitt, Karlsson, and Sorensen, *ABAQUS/standard User's Manual*: Hibbitt, Karlsson & Sorensen, 2001.

[150] E. Samur, M. Sedef, C. Basdogan *et al.*, “A robotic indenter for minimally invasive measurement and characterization of soft tissue response,” *Medical Image Analysis*, vol. 11, no. 4, pp. 361-373, Aug, 2007.

[151] K. Miller, and J. Lu, “On the prospect of patient-specific biomechanics without patient-specific properties of tissues,” *Journal of the Mechanical Behavior of Biomedical Materials*, vol. 27, pp. 154-166, Nov, 2013.

[152] F. Faure, C. Duriez, H. Delingette *et al.*, "Sofa: A multi-model framework for interactive physical simulation," *Soft Tissue Biomechanical Modeling for Computer Assisted Surgery*, pp. 283-321: Springer, 2012.

[153] S. A. Maas, B. J. Ellis, G. A. Ateshian *et al.*, “FEBio: Finite Elements for Biomechanics,” *Journal of Biomechanical Engineering*, vol. 134, no. 1, pp. 011005, 2012.

[154] S. A. Maas, G. A. Ateshian, and J. A. Weiss, “FEBio: History and Advances,” *Annual Review of Biomedical Engineering*, vol. 19, no. 1, 2017.

[155] N. Hamzé, I. Peterlík, S. Cotin *et al.*, “Preoperative trajectory planning for percutaneous procedures in deformable environments,” *Computerized Medical Imaging and Graphics*, vol. 47, pp. 16-28, 1//, 2016.

[156] B. Eiben, L. Han, J. Hipwell *et al.*, "Biomechanically guided prone-to-supine image registration of breast MRI using an estimated reference state." pp. 214-217.

[157] S. Suzuki, N. Suzuki, A. Hattori *et al.*, “Tele-surgery simulation with a patient organ model for robotic surgery training,” *The International Journal of Medical Robotics and Computer Assisted Surgery*, vol. 1, no. 4, pp. 80-88, Dec, 2005.

[158] P.-A. Heng, T.-T. Wong, R. Yang *et al.*, “Intelligent inferencing and haptic simulation for Chinese acupuncture learning and training,” *IEEE Transactions on Information Technology in Biomedicine*, vol. 10, no. 1, pp. 28-41, 2006.

[159] S. P. DiMaio, and S. E. Salcudean, “Needle insertion modeling and simulation,” *IEEE Transactions on Robotics and Automation*, vol. 19, no. 5, pp. 864-875, 2003.

[160] S. Ourselin, M. Emberton, and T. Vercauteren, “From computer-assisted intervention research to clinical impact: The need for a holistic approach,” *Medical Image Analysis*, vol. 33, pp. 72-78, Oct, 2016.

[161] D. J. Hawkes, “From clinical imaging and computational models to personalised medicine and image guided interventions,” *Medical Image Analysis*, vol. 33, pp. 50-55, Oct, 2016.

[162] A. K. Ho, H. Alsaffar, P. C. Doyle *et al.*, “Virtual reality myringotomy simulation with real-time deformation: development and validity testing,” *Laryngoscope*, vol. 122, no. 8, pp. 1844-1851, Aug, 2012.

[163] S. Misra, K. T. Ramesh, and A. M. Okamura, “Modeling of Tool-Tissue Interactions for Computer-Based Surgical Simulation: A Literature Review,” *Presence: Teleoperators and Virtual Environments*, vol. 17, no. 5, pp. 463-491, Oct 01, 2008.

[164] K. Kunkler, “The role of medical simulation: an overview,” *The International Journal of Medical Robotics and Computer Assisted Surgery*, vol. 2, no. 3, pp. 203-210, 2006.